

Science Meets Technology with Advanced Optical Metrology

Access in-depth information on methods and applications in the R&D field of optical metrology through free to access article digests of recent peer-reviewed publications and more.

Discover advancedopticalmetrology.com now!

OLYMPUS

WILEY

Recent Advances in MOF-Derived Single Atom Catalysts for Electrochemical Applications

Zhongxin Song, Lei Zhang, Kieran Doyle-Davis, Xianzhu Fu, Jing-Li Luo,* and Xueliang Sun*

Electrocatalysis plays a critical role in clean energy conversion, enabling great improvement for future sustainable technologies. Single atom catalysts (SACs) derived from metal–organic framework (MOF) are emerging extraordinary materials in electrochemical catalytic applications. Covering the merits of unique electronic structure, low-coordination environment, quantum size effect, and metal–support interaction, SACs promise enhanced electrocatalytic activity, stability, and selectivity in the field of clean energy conversion. In this article, MOF synthesis routes to afford well-dispersed SACs along with the respective synthesis mechanism are systematically reviewed first, and typical examples of each strategy are carefully discussed. Then the characterization techniques in understanding the isolated and spatial distribution, local electronic structure, coordination environment for SACs, and insights into stable mechanisms provided by density functional theory (DFT) calculations are summarized. In addition, several important electrocatalytic applications and electrocatalytic mechanisms of the MOF-derived SACs, including for the oxygen reduction reaction, CO₂ reduction reaction, nitrogen reduction reaction, hydrogen evolution reaction, oxygen evolution reaction, etc., are highlighted. To facilitate the future development of high-performing SACs, several technical challenges and corresponding research directions are proposed.

1. Introduction

Single-atom catalysts (SACs) with isolated metal atoms anchored on support materials exhibit the powerful ability to enhance the metal atom utilization.^[1] Unlike conventional metal

nanoparticles (NPs) catalysts, SACs display unique features like their unsaturated-coordination configuration, quantum size effect, and strong atom–support interaction, which induce the single-atom sites with excellent activity and stability in electrocatalysis.^[1b,2] In 2011, Zhang and co-workers employed a coprecipitation method to prepare Pt SACs supported on iron oxide which demonstrated high activity and stability for CO oxidation.^[3] Sun and co-workers reported the fabrication of Pt SACs on graphene by atomic layer deposition, and the as-prepared Pt SACs showed 10 times higher activity for methanol oxidation and superior CO tolerance compared to the benchmark Pt/C catalyst.^[4] According to this research, it can be seen that “single atom catalysts” developed rapidly and have become a hot research topic in heterogeneous electrocatalysis.

1.1. Identification and Features of SACs

SACs have isolated metal atoms that are anchored on a specific support and can behave as active centers for heterogeneous

catalysis. The concept of single-atom catalysts can be traced back to the pioneering research reported by Zhang and co-workers in 2011. In their work, well-dispersed Pt single atoms were successfully prepared on the FeOx support, which opens the avenue of “single atom catalysts.” The active single-atom sites generally consist of metal atoms and neighboring atoms from support materials. In addition, ion-exchanged metal atoms located on a porous support, as well as organometallic complexes anchored to the substrate, in principle, could also be viewed as SACs.

The unique features of single atoms are significantly different from NPs, which endow SACs with exceptional catalytic activity, stability and selectivity. i) Decreasing the size of metal particles down to single atoms results in the maximum atom-utilization efficiency and metal dispersion. Owing to the low-coordination environment property and fully exposed active sites, SACs are capable to exhibit remarkable electrocatalytic activity toward diverse reactions.^[5] ii) Single metal atoms can coordinate with support materials via strong interaction or charge transfer, which ensure the atomic dispersion and enhanced stability of SACs.^[6] iii) The uniform active sites and geometric configuration of SACs enable similar electronic and spatial interactions with reactant molecules, thereby achieving

Dr. Z. Song, Dr. X. Fu, Prof. J.-L. Luo
Shenzhen Key Laboratory of Polymer Science and Technology
Guangdong Research Center for Interfacial Engineering
of Functional Materials
College of Materials Science and Engineering
Shenzhen University
Shenzhen 518060, China
E-mail: jingli.luo@ualberta.ca

Dr. L. Zhang, K. Doyle-Davis, Prof. X. Sun
Department of Mechanical and Materials Engineering
University of Western Ontario
London, ON N6A 5B9, Canada
E-mail: xsun@eng.uwo.ca

 The ORCID identification number(s) for the author(s) of this article can be found under <https://doi.org/10.1002/aenm.202001561>.

DOI: 10.1002/aenm.202001561

high catalytic selectivity during energy conversion reactions.^[7] Furthermore, The structural homogeneity of SACs favors to identify the active sites, which enable SACs as ideal platforms in fundamental understanding the structure-catalytic mechanism relationship at atomic level.^[8]

1.2. Challenges of SACs and MOF Strategy in Design SACs

SACs made up of individual metal atoms have demonstrated distinguished electrochemical performance, such as excellent catalytic activity, high selectivity and notable cost-reduction. However, the design of SACs with densely dispersed isolated single atoms remains to be great challenges due to easy aggregation of SAs to generate clusters or NPs. Therefore, exploring novel strategy to achieve SACs with uniform atomic active sites, high stability, and facile to scale, is an important goal moving forward.

To now, great strides have been made in the field of SACs synthesis, characterizations, and preliminary applications. Generally, SACs synthesis approaches involving the coprecipitation,^[9] impregnation,^[10] atomic layer deposition,^[4,11] metal-organic framework (MOF) template,^[12] and photoreduction^[13] have been explored. Meanwhile, various metal-based SACs, such as noble metal SACs of Pt, Pd, Au, Ag, Ru, Ir, and non-noble metal SACs of Fe, Co, Ni, Mn, Cu, Zn, etc., have been successfully prepared, and their corresponding electrocatalysis applications have been studied.^[14] Among them, the MOF template synthesis routes indicated great advantages in preparing novel SACs.^[15]

MOF is a kind of crystalline porous material composed of metal nodes and organic linkers. The ordered arrangement of metal nodes and organic ligands enable MOF as ideal template to achieve the supported metal single atoms with uniform dispersion. Since the pioneering work of MOF-5 as template for porous carbon synthesis in 2008,^[16] a variety of examples in fabrication of MOF-derived nanomaterials have been explosively developed.^[17] It has been proved that single metal site can be introduced into the metal nodes, organic linkers, or pores of MOF at different locations. Then post conversion of MOF-coordinated metal precursors into supported metal SAs can be derived through high temperature pyrolysis and reduction. Owing to the advantages of metal-organic hybrid nature, well-defined pore structure, large surface area and tunable chemical composition of MOF precursors, a diversity of MOF-derived SACs can be achieved which have been reported playing significant roles in electrocatalysis of the energy conversion reactions. Initially, researchers focused on investigating the preparation and characterization of SACs. Several good reviews summarized the progress of SACs and their applications.^[1b,8e,18] In recent years, significant progress has been made and many different types of novel SACs with high loading and accessible atomic sites, excellent electrocatalytic activity have been successfully achieved from MOF precursors. However, few discussions on MOF-derived SACs for electrochemical applications can be found in recent reviews. This article focuses on comprehensive summary of recent progress in MOF-derived novel SACs, from aspects of various MOF strategies for SACs

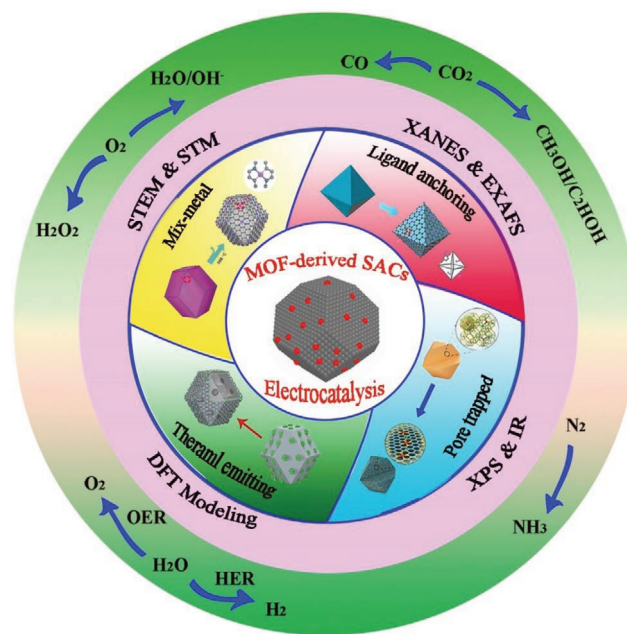


Figure 1. Schematic illustration of MOF strategies in design of single-atom electrocatalysts (SACs), the ex situ/in situ characterization techniques of SACs, and SACs applications in energy conversion reactions.

synthesis, in situ and ex situ characterization techniques, and their critical applications of SACs in electrochemical reactions (Figure 1). Meanwhile, an in-depth understanding of isolated SACs from their local electronic structure to coordination environment and bond distance in determining their advanced electrochemical performance is carefully elaborated and discussed. To facilitate the future development of high-performing SACs, remaining challenges and future directions are also presented. This review would provide an important overview and offer experience for the future practical application of SACs in clean energy conversion.

2. MOF Strategies in Design of SACs

MOFs have demonstrated great promising in electrocatalysis because of their high surface area, well-defined porosity, and flexible tunability.^[19] The merits of isolated metal nodes, organic ligands and ordered pore structures, perfectly cater MOF to the ideal template in anchoring metal SAs and maintaining their stability during the catalytic reactions. Several MOF-based strategies for preparing novel structured SACs have been studied in recent years. By rational coordinate single metal sites in the positions of metal nodes, organic ligands, and pores of MOF precursor, the classification of MOF strategies in design of SACs, including 1) mixed metal nodes of MOF, 2) ligand-coordinated metal of MOF, (3) MOF with pore trapped metal, and 4) thermal emitting of bulk metal for SACs synthesis are elaborated. Herein, recent progress in MOF precursors/templates to afford well dispersed SACs is systematically summarized. Meanwhile, the respective synthesis mechanism and typical examples of each strategy are discussed.

2.1. Mixed Metal of MOF for SACs

As the major component, metal ions are atomically dispersed in MOF structures, which makes MOF an ideal precursor in construction of SAs via reduction of metal ions. It was reported that metal ions can be reduced in operando by high temperature carbonization of organic linkers in MOF precursors, which help produce the metal SAs located in MOF-derived nanomaterials. However, a significant challenge of the migration and aggregation of metal SAs to generate particles during high temperature carbonization, which result the failure of SACs synthesis. Through predesign MOF precursor with mixed metal ions to spatially separate the target metal with an expand adjacent distance, the aggregation of target metal atoms can be effectively avoid, thus making it successful to obtain SACs after high temperature pyrolysis of mixed metal MOF.

As a subclass of MOF, the Zn-based zeolitic imidazolate framework-8 (ZIF-8) with a high content of N dopants in the organic ligands has been considered as ideal precursor in fabrication SACs via one-step pyrolysis of mixed metal MOF.^[20] For example, Li and co-workers developed a MOF strategy to construct Co SACs by direct pyrolysis of Zn/Co bimetallic MOF precursors.^[21] Because of the similar coordination of Co^{2+} and Zn^{2+} with 2-methylimidazole ligands, a Zn/Co bimetallic MOF with homogeneous distribution of Zn and Co ions was initially designed, in which a certain proportion of Zn^{2+} were substituted by Co^{2+} sites. Zn^{2+} serves as a fence to expand the adjacent distances of Co atoms in space. Due to the low boiling point, Zn atoms (907 °C) can be selectively evaporated away at high temperatures

over 800 °C, leaving the isolated Co atoms coordinated with MOF-derived nanocarbon support (Figure 2a). Through tuning the molar ratio of Zn:Co above 1:1, the high loading of Co-SAs (4.0 wt%) can be synthesized on the N-doped carbon support. The authors attempted to pyrolyze Zn/Co bimetallic MOF precursors under temperatures in range of 800–1000 °C. It was revealed that the Co-SAs with Co-N_4 , Co-N_3 , and Co-N_2 coordination configurations can be achieved under different temperatures.

To increase the density of SAs for superior electrocatalytic performance, Wu and co-workers reported an innovative surfactant-assisted bimetallic MOF approach to prepare the Co-based SAC with a high loading of CoN_x active centers.^[22] In their experiment, the surfactant was added as the capping agent to regulate Co-ZIF-8 crystallization, resulting in a surfactant coating shell on Co-ZIF-8 nanocrystals (Figure 2b). The coordination effect between surfactant and $\text{Zn}^{2+}/\text{Co}^{2+}$ ions can slow down the crystal growth rate and adjust the particle size of Co-ZIF-8 crystals. During the subsequent pyrolysis, the surfactant layer can be carbonized and converted into a graphitized carbon shell which coats the outside of Co-ZIF-8 polyhedrons. The carbon shell maintains dominant micropores and high content of N doping sites in the MOF-derived carbon matrix, which contribute to immobilize and mitigate Co SAs agglomeration. Moreover, the atomic dispersion of CoN_4 sites with high density can be achieved by using surfactant of F127, and the Co content reached 1.0 at% higher than the sample prepared without surfactant.

Different from Co ions, some other metal nodes cannot coordinate with imidazolate ligand and form the bimetallic MOF

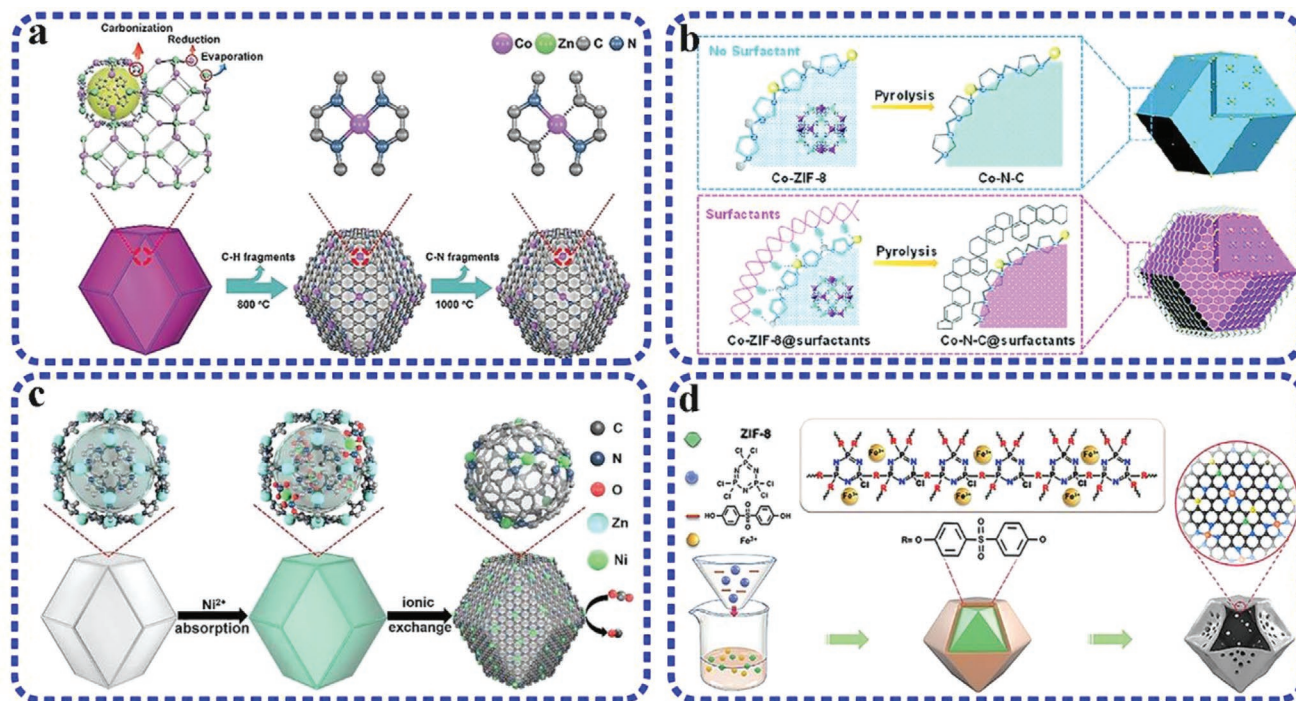


Figure 2. a) Scheme of mixed-metal MOF strategy for synthesis of $\text{Co}_{\text{SA}}\text{-N}_x\text{-C}$. Reproduced with permission.^[21b] Copyright 2019, Wiley-VCH. b) Scheme illustration of synthesis core-shell structured Co-N-Surfactants catalysts with increased active site density. Reproduced with permission.^[22] Copyright 2019, Royal Society of Chemistry. c) Scheme of the formation of Ni SAs/N-C through Ni ionic exchange with Zn species. Reproduced with permission.^[24] Copyright 2017, American Chemical Society. d) Scheme preparation of Fe SAs supported on a N, P, and S codoped hollow carbon. Reproduced with permission.^[25] Copyright 2018, Nature Publishing Group.

with Zn ions. However, the approach of metal ionic exchange by replacing Zn ions with target metal to obtain pre-designed mixed metal MOF has been exploited for design of SACs. A Zn-based MOF was subjected to modify via trans-metalation to yield atomically dispersed Cu, Co, or Ni atoms.^[23] Farha and co-workers described the successful installing of Cu, Ni, and Co SAs into Zn-MOF via the metal exchange approach. Zn-MOF were soaked in methanolic solutions of $\text{CuCl}_2 \cdot 2\text{H}_2\text{O}$, CuBr_2 , or $\text{Cu}(\text{NO}_3)_2 \cdot 2.5\text{H}_2\text{O}$ for 3, 6, and 10 h, resulting in color change of the yellow Zn-MOF powder to pale green. After washing repeatedly with fresh methanol and acetone, Cu atoms exchanged with Zn nodes and afforded Cu SAs incorporated into Zn-MOF. Additionally, Ni and Co installing in Zn-MOF can be achieved through the metal ionic exchange method. These experimental results indicated that metal ionic exchange provides possibility in replacing the initial metal from MOF with extra metal atoms, which benefit to install the target metal SAs in ZIF precursor. In another example, Li and co-workers reported the ionic exchange approach between Zn metal nodes and Ni ions and then to generate Ni SAs distributed on the surface of N-doped carbon via pyrolysis of mixed metal Ni-ZIF-8.^[24] As shown in Figure 2c, the initial ZIF-8 precursor was homogeneously dispersed in n-hexane, followed by the injection of $\text{Ni}(\text{NO}_3)_2$ aqueous solution. In the aqueous-hexane double-solvent, the Ni ions could diffuse into the ZIF-8 structure and exchange with Zn nodes. Then the Ni ions can be confined in ZIF-8 surface to obtain the Ni-doped ZIF-8. After 1000 °C pyrolysis in Ar atmosphere, the Ni-ZIF-8 was transformed into Ni SAs anchored on the surface of N-doped carbon with Ni SAs loading of 1.53 wt%.

Moreover, Wu and co-workers developed a chemical doping approach to synthesize Fe-doped bimetallic Zn-MOF.^[2e] Within the ZIF-8 hydrocarbon network, Fe ions partially replace Zn and chemically bond with imidazolate ligands to form Fe-N_4 complex. One-step thermal activation was subsequently executed to convert Fe-N_4 complex into active FeN_4 atomic sites embedded in porous carbon without metallic agglomeration. Rational design the geometric structure of SACs to expose active sites with high permeability is important to facilitate the mass and electron transfer during reactions. Li and co-workers developed a MOF@polymer strategy to construct Fe SAs located in nitrogen, phosphorus and sulfur codoped hollow carbon polyhedra (Fe-SAs/NPS-HC).^[25] The polymer of poly(cyclotriphosphazene-co-4,4'-sulfonyldiphenol) (PZS) coating on the surface of Fe/ZIF-8 exhibit the shell thickness of 20 nm. After pyrolysis at 900 °C in Ar, the Fe/ZIF-8@PZS was converted into the Fe-SAs/NPS-HC with Fe SAs content of 1.54 wt% located on the hollow matrix (Figure 2d). By analyzing the formation process, it was demonstrated that the pyrolysis occurs following the Kirkendall effect. S^{2-} ions from the PZS shell induce decomposition of ZIF-8 at low temperature (400 °C) for releasing Zn^{2+} ions. The unequal interdiffusion of the S^{2-} ion and Zn^{2+} ion in the interface of ZIF-8 core and PZS shell result in the emergence of Kirkendall voids. With increasing pyrolysis temperature and the Kirkendall proceeding, the inner ZIF-8 gradually decomposes, Zn vaporizes and escapes, resulting in the construction of a hollow structure of Fe-SAs/NPS-HC. The mixed-metal MOF strategy provides an effective

way to anchor target metal SAs in MOF precursor. After a facile and one-step pyrolysis reduction, the mixed-metal MOF can be well converted into MOF-derived highly stable SACs without metal agglomeration.

2.2. Ligand-Coordinated Metal of MOF for SACs

SACs can be constructed by pyrolysis and in situ reduction of the atomically dispersed mixed metal MOF precursor. However, noble metals (Pt, Pd, Ru, etc.) have been rarely used as the metal node during MOF preparation, thus hindering the fabrication of noble metal SACs from metal nodes of MOF. Fortunately, the functional organic ligands show great advantages in coordination with noble metal ions and enable strong anchoring effect to stabilize noble metal SAs. Li and co-workers employed the dangling $-\text{NH}_2$ located at the terephthalic acid linkers in UiO-66- NH_2 to coordinate and stabilize Ru SAs.^[26] The MOF precursor of UiO-66- NH_2 hold abundant dangling $-\text{NH}_2$ groups, Ru metal ions can be adsorbed within MOF channels by forming a strong interaction between the lone pair electron of N ($-\text{NH}_2$) and d-orbital of Ru atoms (as shown in Figure 3a). After pyrolysis UiO-66- NH_2 -Ru at inert atmosphere, the coordinated Ru ions can be reduced by the surrounding C species and result in anchored Ru SAs. The functional dangling $-\text{NH}_2$ from MOF organic ligands played a critical role in anchoring Ru SAs. The strong coordination interaction between Ru ions and $-\text{NH}_2$ limits Ru atoms diffusion and migration at high temperature thus avoiding Ru aggregation to form Ru NPs. By comparison, without the assistance of $-\text{NH}_2$ groups, Ru ions are prone to migration during pyrolysis and tend to aggregate to Ru clusters or NPs.

Defects and unsaturated anchoring ligands from MOF are critical to immobilize the SAs with isolated dispersion. Incorporation of single metal sites into organic square-planar porphyrin ligands of MOF, has been reported to be effectively in anchoring noble metal SAs. Wang and co-workers demonstrated a competitive coordination procedure to synthesize hollow nanotubes of Zr-porphyrinic-MOF composed with square-planar porphyrin ligands and Zr nodes.^[27] Treating the Zr-porphyrinic-MOFs with $\text{IrCl}_3 \cdot x\text{H}_2\text{O}$ or $\text{H}_2\text{PtCl}_6 \cdot 6\text{H}_2\text{O}$, the porphyrinic ligand can effectively grab Ir or Pt ions and trap them in the ligand center, thus forming the ligand-coordinated Ir/Zr-porphyrinic-MOF and Pt/Zr-porphyrinic-MOF complex with atomically dispersed Ir and Pt atoms (Figure 3b). Moreover, this square-planar porphyrin ligand can be extended to anchor other noble metals such as Ru, Au, Pd atoms. In another example, Jiang and co-workers reported a similar strategy to confine Pt SAs into MOF skeleton for efficient catalysis. A highly stable Al-based porphyrinic MOF (Al-TCPP) was synthesized by the hydrothermal method, in which $\text{Al}(\text{OH})\text{O}_4$ chains are interconnected with porphyrin linkers to construct the 3D microporous framework. $\text{Pt}_{(\text{II})}$ ions were then implanted into the center of porphyrin linkers in Al-TCPP to yield Al-TCPP- $\text{Pt}_{(\text{II})}$. After Pt reduction at 180 °C in H_2 atmosphere, stable Pt SAs with loading of 0.07 wt% were prepared which show strong interaction with pyrrolic N dopants in the Al-TCPP support (Figure 3c).^[12c]

Design SACs with hierarchical pore structure is of benefit to mass transport and active sites exposure which has attracted great interest in the field of electrocatalysis. Jiang

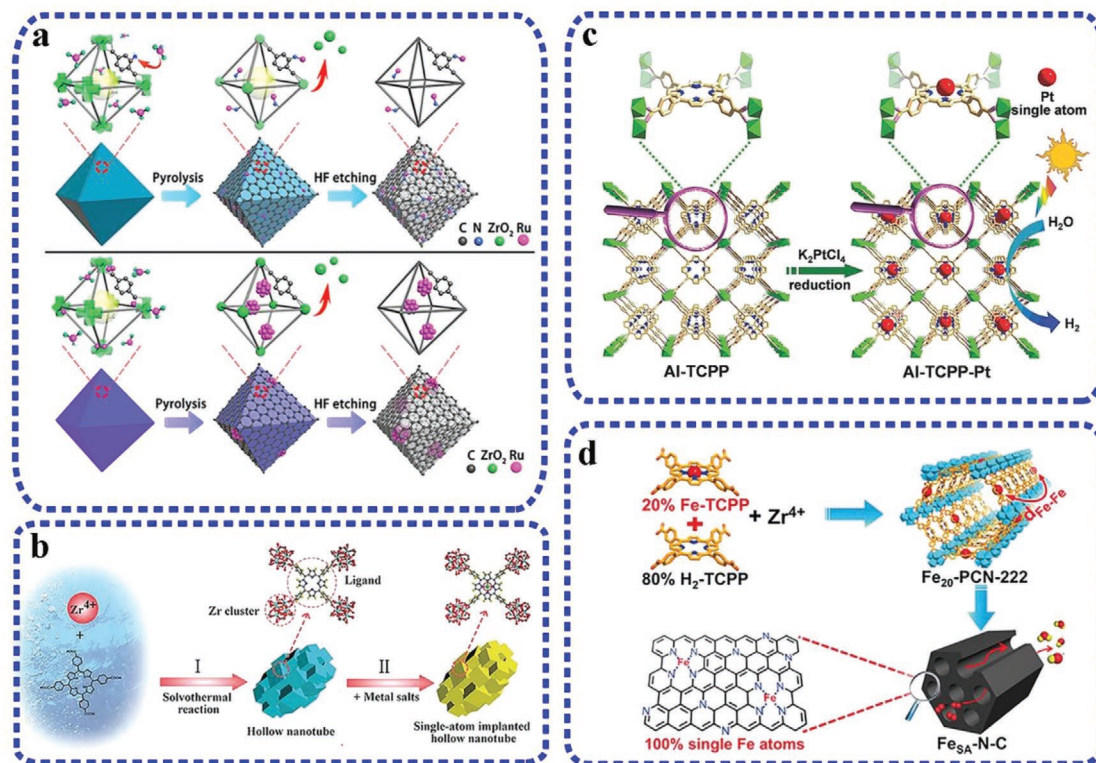


Figure 3. a) Scheme of the formation mechanism for Ru SAs through ligand-coordinated metal MOF. Reproduced with permission.^[26] Copyright 2017, American Chemical Society. b) Formation of the metal SAs immobilized in Zr-porphyrinic-MOF. Reproduced with permission.^[27] Copyright 2018, Wiley-VCH. c) Schematic illustration for the synthesis of Al-TCPP decorated with Pt SAs. Reproduced with permission.^[12c] Copyright 2018, Wiley-VCH. d) Scheme for the rational fabrication of Fe SAs in $\text{Fe}_{\text{SA}}\text{-N-C}$ catalyst via a mixed-ligand strategy. Reproduced with permission.^[28a] Copyright 2018, Wiley-VCH.

and co-workers chose a porphyrinic MOF (PCN-222) featuring 1D mesochannels with diameter of 3.2 nm as a representative precursor.^[28] Employing the mixed-ligand of Fe-TCPP and $\text{H}_2\text{-TCPP}$, a series of isostructural Fe-PCN-222 hybrids constructed with different ligand ratio were initially prepared. To obtain the Fe SACs, small amount of Fe-TCPP was assembled into 3D networks of Fe-PCN-222. Fe-TCPP molecules participant in building the framework of Fe-PCN-222 which are separated with each other by the adjacent $\text{H}_2\text{-TCPP}$ ligands, thereby resulting the isolated Fe-TCPP existence in the Fe-PCN-222 MOF structure. Beyond one-step pyrolysis, the precursor of $\text{Fe}_{20}\text{-PCN-222}$ with optimized mixed-ligand ratio can be converted into mesoporous N-doped carbon decorated with highly dispersed Fe SAs (Figure 3d). The pyrolysis of porphyrinic ligand coordinated Fe-MOFs enable the construction of hierarchical N-doped porous carbon implanted with high content of 1.76 wt% Fe SAs. These studies highlight the great advantages in design of metal SACs based on the MOF with ligand-anchored metal sites.

2.3. MOF with Pore Trapped Metal for SACs

Due to the well-defined cavity structure of MOF, the spatial confinement has been attempted to create SACs by trapping metal molecules within MOF pores. The encapsulating and

separating metal molecules via molecular-scale pore space was considered as a pore-trapped MOF strategy for design of SACs.^[29] For example, highly reactive Fe SAs anchored in N-doped porous carbon (FeSA/NC) with Fe-SAs loading of 2.16 wt% was prepared via pyrolysis of cage-encapsulated-MOF.^[29a] Typically, ZIF-8 with a cavity diameter of 11.6 Å and pore diameter of 3.4 Å was employed as molecular cages to encapsulate the $\text{Fe}(\text{acac})_3$ salt with molecular diameter of ≈ 9.7 Å. During the ZIF-8 synthesis, molecular-scale cages can be formed along with assembling of Zn^{2+} and 2-methylimidazole species (Figure 4a). Meanwhile, one $\text{Fe}(\text{acac})_3$ molecule can be trapped in one cage of ZIF-8 resulting in the encapsulated $\text{Fe}(\text{acac})_3@ZIF-8$ complex. Through pyrolysis of $\text{Fe}(\text{acac})_3@ZIF-8$ at 900 °C under Ar atmosphere, the encapsulated $\text{Fe}(\text{acac})_3$ was reduced into Fe-SAs by hydrocarbons decomposed from organic linkers, while ZIF-8 was transformed into N-doped porous carbon (NC), thereby forming the N-doped carbon decorated with Fe-SAs (FeSA/NC).

Furthermore, it was reported that the organic ligands coordinated with Fe^{2+} ions also play a significant role in determining the Fe-SACs activity. Sun and co-workers prepared the nitrogen-doped carbon supported Fe SAs (Fe-Nx-C) through encapsulating Fe-Phen complexes into the nanocages of ZIF-8 (Figure 4b). The pore space of ZIF-8 well trap and separate Fe-Phen complexes, which played significant role in fabricating isolated Fe SAs during Fe-Phen@ ZIF-8 pyrolysis. Importantly, this MOF strategy with

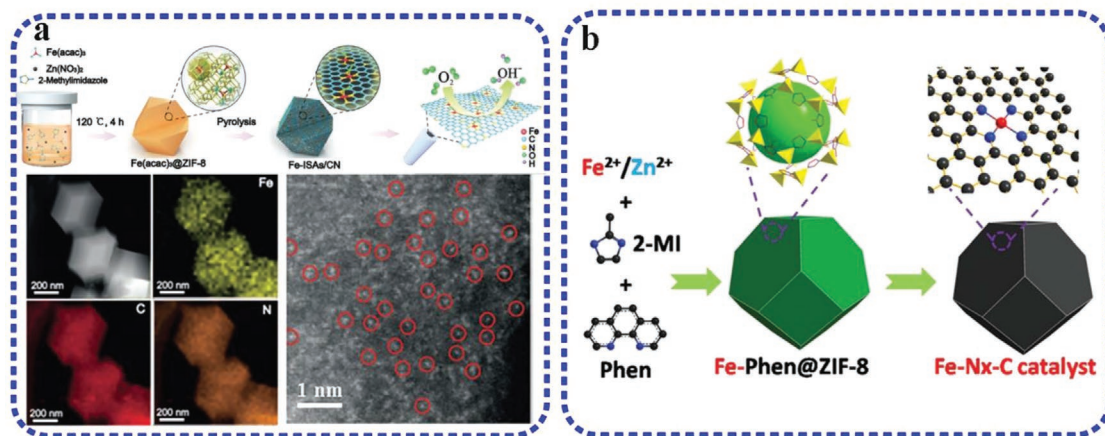


Figure 4. a) Schematic illustration of design FeSA/NC via space encapsulated $\text{Fe}(\text{acac})_3@ZIF-8$ complex. Reproduced with permission.^[29a] Copyright 2017, Wiley-VCH. b) Schematic illustration for the synthesis of Fe-Nx-C via space encapsulated $\text{Fe-Phen}@ZIF-8$ complex. Reproduced with permission.^[29d] Copyright 2019, Wiley-VCH.

space encapsulated metal can be generalized to prepare other non-noble metal SACs such as Co-Nx-C , Ni-Nx-C , Cu-Nx-C . However, it is worth noting that the pore-confined MOF strategy requires guest metal species well encaged with molecular size between pore diameter and pore opening, which guarantee only one metal molecule confine in one cage of MOF to prevent the aggregation of metal sites upon high temperature pyrolysis.

2.4. Thermal Emitting of Bulk Metal for SACs

Developing facile large-scale synthesis of sinter-resistant SACs which can maintain high activity over long-time operation is one primary target for SACs. In order to fabricate thermally stable SACs, reverse sintering from metal NPs and converting NPs into SAs is recognized as one potential solution. Jones and co-workers reported that high temperature treatment of bulk metal can emit isolated metal species. Once the mobile species are effectively trapped by a suitable support surface, atomically dispersed SAs can be produced.^[30] In their work, ceria powders with well-defined nanoshapes, such as nanorod, cube and octahedra were studied as effective surface for trapping Pt SAs. When mixing ceria with Pt NPs/ Al_2O_3 and aged at 800°C in air, the bulk Pt can emit mobile Pt atoms which were trapped by the ceria support and resulting ceria supported Pt SAs (Figure 5a). This top-down thermal emitting technique shows distinct advantages in approaching Pt SAs with high stability and sintering resistance. Inspired by the reversing idea from NPs to SAs, Li and co-workers developed thermally stable Pt, Pd, and Au SACs.^[31] They synthesized ZIF-8 nanocrystals on Pd NPs by mixing Pd NPs with $\text{Zn}(\text{NO}_3)_2$ and 2-methylimidazole solution. ZIF-8 nanocrystals grow around Pd NPs and obtained Pd-NPs@ZIF-8 composites. Then the conversion of Pd NPs to SAs occurred during heat treatment of Pd-NPs@ZIF-8 composites at 900°C under inert atmosphere. It was discovered that the N-doped carbon derived from ZIF-8 acts as the anchoring substrate, which can capture Pd atoms. As shown in Figure 5b, in situ environmental characterization observed that sintering occurs and large Pd NPs generate during the initial

0.5 h of heat treatment. However, the enlarged Pd NPs would intensively collapse along with the ZIF-8 carbonization, gradually becoming smaller, and finally digested within the substrate and transformed into Pd SAs. The thermal conversion of metal NPs to SAs was also applicable to other noble metals such as Pt and Au. Furthermore, computation calculations indicated that noble metal NPs to SAs conversion was motivated by formation of the more thermodynamically stable metal- N_4 structure when moving metal atoms were trapped on the defects of N-doped carbon support. This top-down route in fabricating SACs from NPs provides valuable insights for preparing high-performing and thermally stable SACs.

In situ thermal atomization to convert non-noble metal Ni NPs into surface-bound stable Ni SACs was studied and reported by Wu and co-workers.^[32] Ni NPs distributed on the defective N-doped carbon can be transformed into carbon supported Ni SAs through thermal diffusion. It was reported that Ni NPs can break surface C-C bonds and drill into the carbon matrix during high temperature treatment. When Ni NPs were exposed to the N-doped carbon, Ni atoms can be bound by N-rich defects. The strong coordination could trap Ni SAs from Ni NPs, resulting in Ni SAs splitting and being stabilized within the surface of the N-doped carbon (Figure 5c). The homogeneous Ni atoms distribution confirmed the successful top-down transformation from Ni NPs to SAs. By contrast, non-defective XC-72 carbon support was studied and representative Ostwald-ripening of Ni NPs from 5 to about 50 nm was observed, which implied that the defect sites from N-doped carbon support are the key factor in trapping and anchoring Ni SAs.

In contrast to generating SACs from parent NPs, direct fabrication of SACs from cheap and available bulk metal would have great commercial competitiveness.^[33] Li and co-workers reported a practical strategy to large-scale synthesis of SACs via thermal emission of metal atoms from metal bulk. As shown in Figure 5d, the formation mechanism of Cu SAs supported on N-doped carbon is demonstrated. Firstly, ZIF-8 pyrolysis occurs at 900°C , which produces the N-doped porous carbon with abundant N-doping sites. Under a high temperature NH_3 atmosphere, NH_3 molecules can coordinate with bulk Cu foam

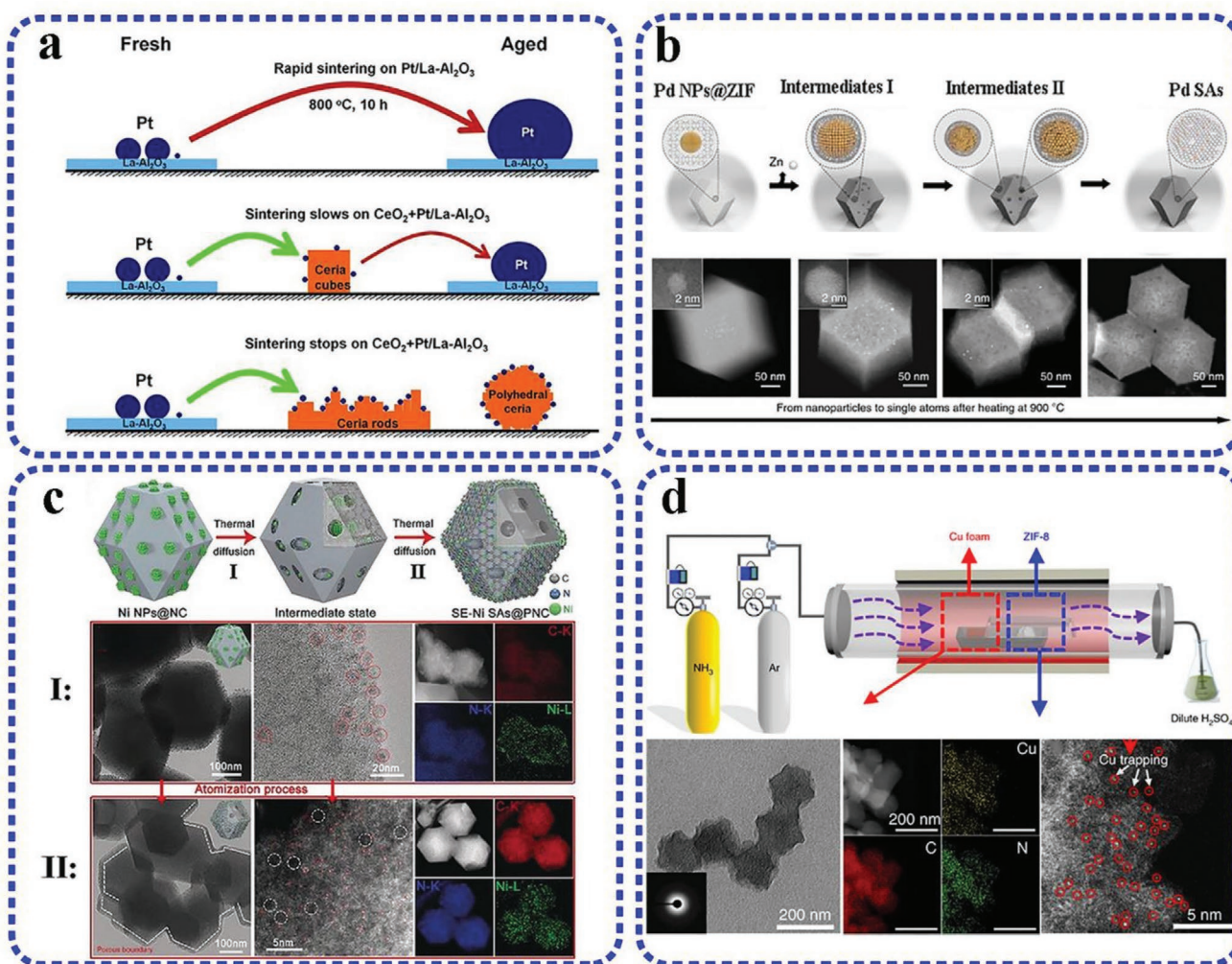


Figure 5. a) Scheme of Pt NPs sintering and atomization, showing how ceria can trap the mobile Pt atoms under high temperature aging process. Reproduced with permission.^[30] Copyright 2016, American Association for the Advancement of Science. b) Scheme for the transformation of Pd NPs to SAs and structural characterizations of Pd SAs. Reproduced with permission.^[31] Copyright 2018, Nature Publishing Group. c) Scheme of thermal transformation of Ni NPs into Ni SAs and structural characterizations of NiNPs@NC and NiSAs@NC. Reproduced with permission.^[32] Copyright 2018, Wiley-VCH. d) Scheme of the top-down preparation and characterization of Cu-SAs/N-C. Reproduced with permission.^[33a] Copyright 2018, Nature Publishing Group.

and grab Cu atoms to generate Cu(NH₃)_x species based on the Lewis acid-base interactions. Then, Cu(NH₃)_x species migrated and were trapped by the N-dopants in carbon support, resulting in isolated Cu SAs anchored on the carbon support (CuSAs/N-C). In another work, a thermal emission strategy was applied to synthesize noble metal Pt SAs.^[33b] During the synthesis, dicyandiamide (DCD), Pt mesh and graphene oxide (GO) were sequentially placed in the tube furnace and then heated to 1100 °C under Ar atmosphere. At high temperature, the DCD releases NH₃ gas which forms strong coordination with Pt atoms and generate volatile Pt(NH₃)_x species. Then Pt(NH₃)_x was anchored by the defective sites from the GO, and supported Pt SAs with loading of 2.1wt% were achieved. Moreover, a series of metal-SAs/N-C (such as Co, Ni, Pd, Au etc.) could be fabricated through this NH₃ assisted thermal emission and gas-migration approach, implying its practicality in achieving various SACs. Benefitting from the cheap bulk metal precursor for metal SAs as well as the

facile process, the thermal emission MOF strategy in preparing stable SAs shows great potential in purpose of scaling up SACs for practical energy conversion application.

Based on the above progress, it can be briefly summarized that MOF-template is an effective strategy for the preparation of SACs (Pt, Pd, Ru, Fe, Co, Ni, Cu, etc.). High surface area of MOF-derived carbon support should enable SACs with high loading under the uniform distribution. Doping effect and spatial confinement contribute metal SAs with great advantages in stability. Although tremendous progress of MOF-derived SACs have been achieved, most of the research is focused on a few kind of MOF such as ZIF-8, ZIF-67, UiO-66-NH₂, Zr-porphyrinic-MOF, and Al-porphyrinic-MOF, which are suitable for SACs preparation. Novel design strategies to broaden the available MOF precursors for SACs are still in high demand. To obtain SACs with high loading of SAs and most exposure of active sites, the high surface area MOF precursors with 2D

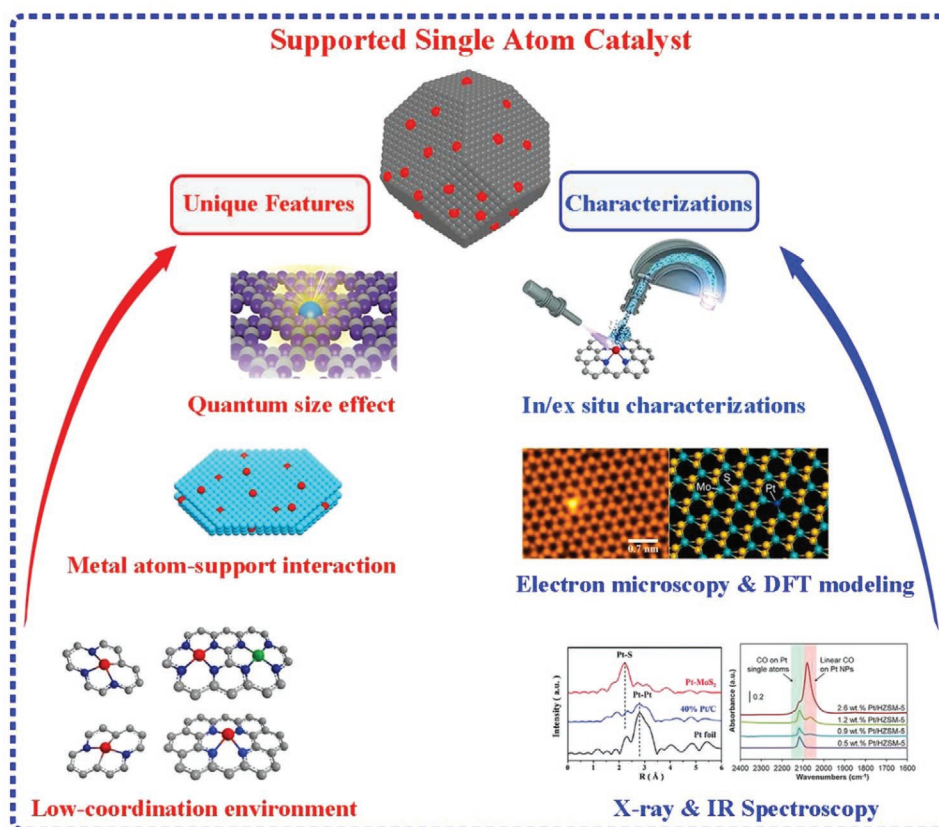


Figure 6. Scheme illustration of unique features and characterization techniques for single atom catalysts (SACs).

morphology, micro/mesoporous hierarchical structure and even hollow structure should be in highly desirable.^[34] Moreover, novel MOF precursors with high content of heteroatom doping sites (e.g., N, P, S, B, etc.) in their ligands are expected which are considered with great advances in fabrication SACs with superior stability.^[35] In addition to carbon supported SACs, incorporation of metal SAs to the MOF-derived transition metal-based materials should be developed, which are expected to endow SACs with enhanced electrical conductivity and strong metal–support interaction, and are vital in the electrochemical energy conversion reactions.^[36]

3. Characterization Techniques of SACs

Characterization of supported SACs is critical in understanding their microstructure which is firmly related to their electrochemical properties. Therefore, the identification of isolated SAs and confirmation of their spatial distribution are significantly important. Nowadays, advanced characterization tools used for identifying SAs include electron microscopy techniques, such as aberration-corrected high-angle annular dark field scanning transmission electron microscopy (HAADF-STEM) and scanning tunneling microscopy (STM), and spectroscopy techniques, such as X-ray absorption spectroscopy (XAS) involving extended X-ray absorption fine structure spectroscopy (EXAFS), X-ray absorption near edge spectroscopy

(XANES), X-ray photoelectron spectroscopy (XPS) and infrared spectroscopy (IR) (**Figure 6**). In this section, we will introduce these in situ and ex situ characterization techniques in understanding the microstructure and coordination environment of SACs. Moreover, the density functional theory (DFT) calculations offer deep insight into the original stable active centers and understanding the reaction mechanism.

3.1. Electron Microscopy

The most intuitive approach for observation of SACs is direct imaging SAs dispersion on the support surface. The aberration corrected transmission electron microscopy (AC-TEM), in both bright-field (HRTEM) and dark-field (HAADF-STEM) modes, has been widely utilized to observe the atomic structure and distribution of SACs.^[37] Based on the principle of Rutherford scattering, the image intensity collected from HAADF-STEM is proportional to the square of atomic number (Z^2) for the selected element, which allows heavy atoms to show bright contrast compare with light atoms. Nowadays, some ideal support materials of metal oxides such as FeOx, SiO₂, and TiO₂ (**Figure 7I**),^[3,38] and 2D materials of graphene and MoS₂ (**Figure 7II**),^[6b,39] as well as MOF derivatives (**Figure 7III**),^[40] have been attempted to anchor metal SAs. HAADF-STEM combined with element mapping techniques can give direct information of the location and distribution of metal SAs.

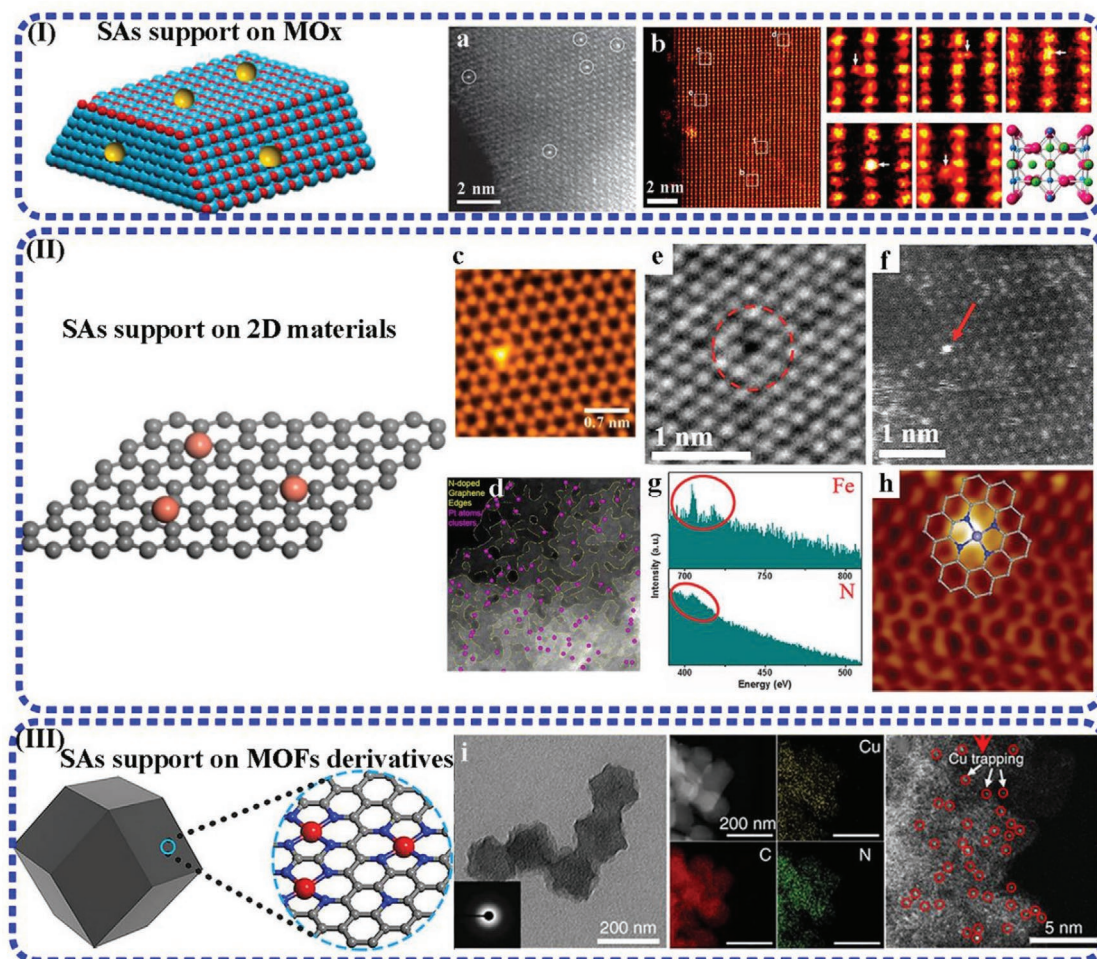


Figure 7. I) Metal SAs support on metal oxide: a) HAADF-STEM image of Pt₁/FeOx. Reproduced with permission.^[3] Copyright 2011, Nature Publishing Group. b) HAADF STEM images of Pt single atoms on TiO₂ (110) surface. Reproduced with permission.^[38b] Copyright 2014, American Chemical Society. II) Metal SAs support on 2D materials: c) HAADF-STEM image of Pt single atoms on 2D MoS₂. Reproduced with permission.^[39c] Copyright 2017, American Chemical Society. d) HAADF-STEM image of Pt single atoms/clusters on N-doped graphene. Reproduced with permission.^[41] Copyright 2014, American Chemical Society. e–h) Low-temperature STEM image and EELS of FeN₄-graphene. Reproduced with permission.^[39a] Copyright 2015, American Association for the Advancement of Science. III) Metal SAs support on MOFs derivatives: i) HRTEM, EDS mapping and HAADF-STEM images of Cu single atoms on MOF-derived N-doped carbon. Reproduced with permission.^[33a] Copyright 2018, Nature Publishing Group.

For example, Zhang and co-workers determined the exact position of Pt SAs on FeOx through HAADF-STEM techniques.^[3] As shown in Figure 7a, isolated Pt atoms appear as bright spots, which dispersed on the surface of FeOx support and located exactly at the position of Fe atoms. By varying beam focus settings, authors claimed that the density of Pt SAs was about 0.07 Pt atoms nm⁻² in FeOx. It was found that Pt atoms are either located on the surface or in the near subsurface of the FeOx nanocrystals, no Pt atoms were detected inside the FeOx crystals. In another study, Shibata and co-workers showed direct atomic-resolution HAADF-STEM images of individual Pt atoms adsorbed on TiO₂ (110) surfaces, in which many Pt atoms are determined to be isolated SAs.^[38b] The sub-angstrom spatial resolution enables the identification of five different Pt atoms adsorption sites on the TiO₂ (110) surface (Figure 7b). Combined with DFT calculations, it was further revealed that the most favorable Pt adsorption sites on TiO₂ are the basal oxygen vacancies which are located in subsurface positions

instead of top surface bridging oxygen atoms. The HAADF-STEM technique unraveled the interfacial interaction between the Pt atoms and TiO₂ surfaces at the atomic dimension, which is great significant in understanding the accurate location of SAs.

Another powerful advantage of HAADF-STEM is the ability in study the atomic level interfacial interactions between SAs and anchoring sites from support.^[39b,c] Warner and co-workers explored the detailed atomic structure of Pt SAs on monolayer MoS₂.^[39c] As shown in Figure 7c, bright contrast from the atomically resolved Pt atom with monolayer MoS₂ lattice enables to distinguish its exact position. It was found that Pt atoms on pristine MoS₂ were anchored by bonding with single or double S vacancies. The chemical bonding between Pt atoms and S vacancies ensured the high stability of Pt SAs. However, when the MoS₂ surface was contaminated by carbon, a different behavior of Pt atoms located at random sites on MoS₂ lattice appeared. Because Pt bonding with amorphous carbon

layer, which disrupts the intrinsic Pt-MoS₂ interactions, leading to more varied dispersion of Pt SAs. In another case, Botton and co-workers employed HAADF-STEM to determine the atomic structure information of Pt SAs dispersed on N-doped graphene sheets.^[6b,41] Through examination of the structural information of Pt species, it was revealed that both individual Pt SAs (bright Pt spots) and Pt subclusters were presented on the surface of N-doped graphene sheets (Figure 7d). Further element mapping of Pt SAs indicated that Pt atoms prefer to be anchored at the location of atomic step edges, suggesting the defect from graphene are the favorable sites in anchoring Pt atoms.

It is worth mentioning that the energy supply from electron beam may cause dynamic hopping and migration of metal SAs, leading to inaccurate atomic characterization. To obtain veritable atomic and electronic information of SAs, Bao and co-workers performed low-temperature scanning tunneling microscopy (LT-STM, 4K) to analyze single-atom Fe sites.^[39a] From the aberration-corrected HRTEM of Figure 7e and HAADF-STEM image of Figure 7f, it was found that atomic Fe species were homogeneously dispersed within the graphene matrix. Through examination of the electron energy loss spectroscopy (EELS) of one bright dot (Figure 7g), both Fe and N elements were clearly detected, indicating Fe–Nx bonding structure composed of Fe atoms coordinated with N atoms. The LT-STM image (Figure 7h) of FeNx embedded in the graphene matrix was resolved and the Fe centers were observed as bright spots. The neighboring atoms of Fe exhibited a higher apparent height than carbon atoms in the graphene, which were assigned as four nitrogen atoms, confirming the Fe–N₄ coordination structure. In the example of MOF-derived Cu SACs, the image of Figure 7i showed that the structure of pyrolyzed ZIF-8 maintained its parent shape and crystal size. The element maps of Cu SACs indicated the homogeneous dispersion of Cu, N, and C over the whole architecture. It was claimed that the individual Cu atoms were trapped by the defective N-dopants, which served as effective anchoring sites for capturing Cu atoms and trapping them in the MOF-derived support.

3.2. X-Ray Absorption Fine Structure (XAFS)

Deep insight into local electronic structure is important for understanding the structure–property relationship in SACs. Synchrotron radiation-based XAFS technique as a powerful tool has attracted great attention for SAs characterization, because the spectrum obtained from XAFS is sensitive to the electronic structure, local atomic structure and coordination environment for the selected core element.^[37b,42] When the energy of incoming X-ray is higher than the binding energy of certain core-level, electrons in core-level might be ejected to the valence band or continuum. Such process is called X-ray absorption and can be used to determine metal atoms electronic environment. XAFS is generally divided into two regimes: X-ray absorption near-edge spectroscopy (XANES) and extended X-ray fine structure spectroscopy (EXAFS). XANES arises from electronic transition in the energy range of –20 to 50 eV from the absorption edge, is applied to analyze the oxidation state, geometry and electronic structure for the central atom. While EXAFS

in the energy range of 50–1000 eV from the absorption edge, is favorable for information of radial distribution, interatomic distance, coordination number and bond length.^[42] Due to powerful functions, XAFS has been widely employed to examine the SACs in both ex situ and in situ mode.

3.2.1. XANES Analysis of SACs

XANES can be applied to study the local electronic structure^[43] and quantitatively determine the unoccupied electron vacancy of central metal SAs.^[4,6c] By analyzing the main X-ray absorption edge energy shift, it is possible to confine the oxidation state of the metal species. In addition, the XANES peak intensity is proportional to the corresponding density of unoccupied density of electron states, which contributes to quantitatively identifying and determining the electronic and chemical structures of core metal SAs.

For example, Huang and Duan group conducted XANES to understand the electronic nature of monodispersed transition metal atoms implanted in N-doped graphene frameworks (M_{SAS}-NGF).^[43c] The X-ray absorption fine structure analyses combined with STEM imaging identified that M_{SAS}-NGF materials adopted the MN₄C₄ configuration with metal SAs occupying the divacancies in the graphene lattice. The XANES profiles of M_{SAS}-NGF along with their references are shown in Figure 8a. The pre-edge feature due to the 1s → 4p transition appears in the XANES, and a noticeable pre-edge shift to higher energy for M_{SAS}-NGF compared to metal bulk was observed. The fact of pre-edge energy position of M_{SAS}-NGF in between bulk and metal oxides suggested that M-SAs were in oxidation states other than in metallic formation. Comparing the first derivative XANES (insets) for Ni_{SAS}-NGF, Fe_{SAS}-NGF, Co_{SAS}-NGF with their references, it was found that the stable valence states of metal SAs are +2, +3 and +2 for Ni, Fe and Co SAs, respectively. Moreover, XANES analysis enables quantitative identification of the local structure of M–Nx–C species. The authors carried out XANES simulation by evaluating MN₄C₄ moieties in the graphene lattice. It was revealed that the graphene enclosed MN₄C₄ structure can be regarded as a single metal atom occupying the divacancy of graphene matrix by coordination with four pyridinic N. With one end-on dioxygen molecule in the axial position of metal SAs sites (O₂–MN₄C₄), all features of the theoretical simulated spectra can excellent agreement with the experimental XANES spectra (Figure 8a). The structural refinement based on comprehensive XANES analyses determined the local sites of MN₄C₄ in M_{SAS}-NGF. To unambiguously identify the coordination configuration of MN₄C₄ species and the corresponding bond strength, more detailed EXAFS and DFT predictions are further required.

As the XANES is proportional to the projected density of unoccupied density of electron states (DOS),^[44] this important function can be utilized to quantitatively determine the electronic structure of metal atoms. Sun and co-workers carried out the XANES spectra to investigate the electronic environment of Pt SAs^[6b] and Pt–Ru dimers.^[6c] By qualitative and quantitative analyzing the normalized XANES spectra at Pt L₃- and L₂-edge, the detailed Pt SAs d-state electronic property was revealed. The XANES spectra (Figure 8b) showed that both Pt L₃- and

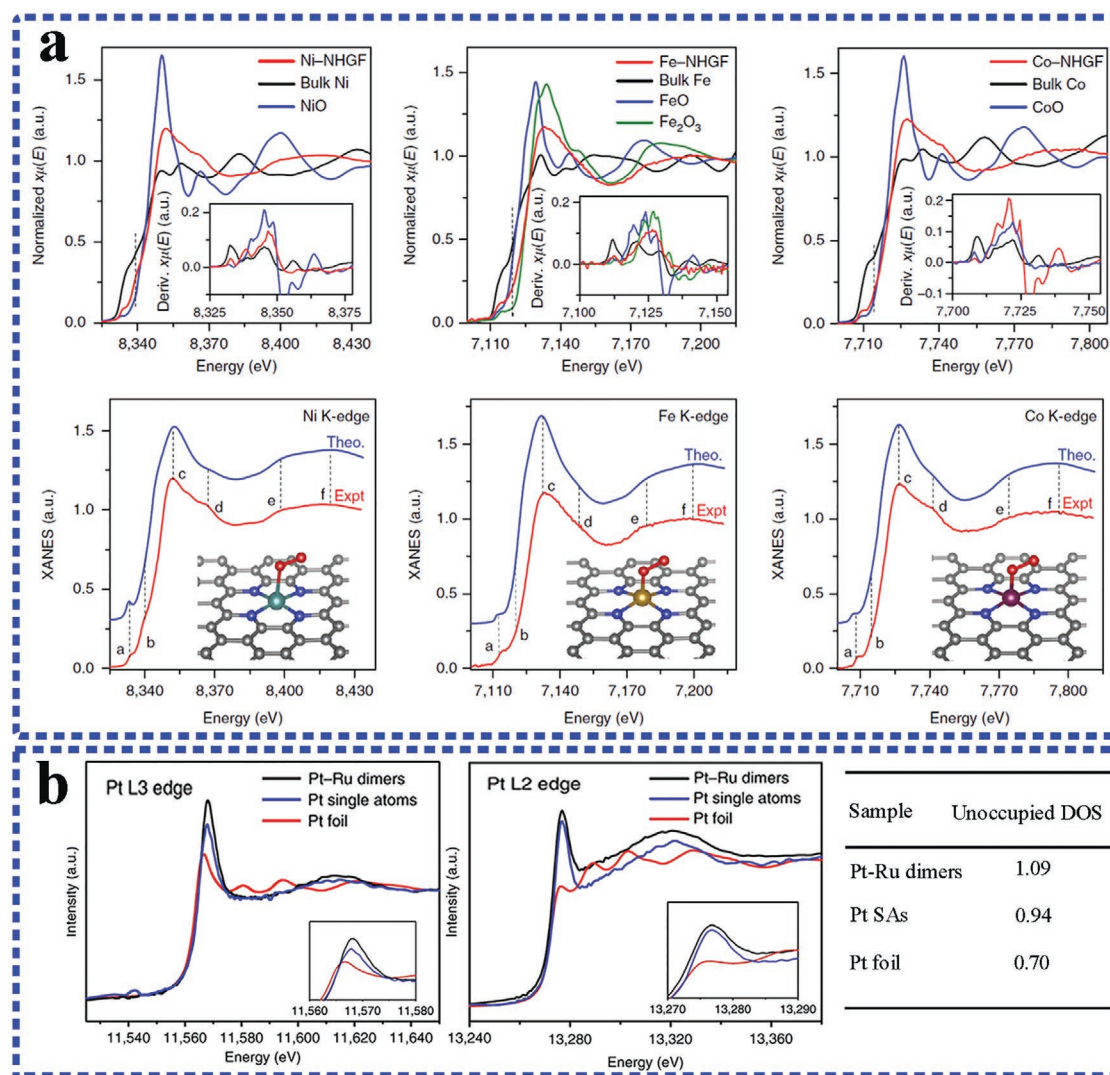


Figure 8. a) Structural characterization by XANES spectroscopy on Ni_{SAs}-NGF, Fe_{SAs}-NGF, Co_{SAs}-NGF, and reference samples; comparison between the experimental K-edge XANES spectra of M_{SAs}-NHGFs and the theoretical spectra of MN₄C₄ moieties embedded in graphene lattice. Reproduced with permission.^[43c] Copyright 2018, Nature Publishing Group. b) The normalized XANES spectra at Pt L₃- and L₂-edge of Pt–Ru dimers, PtSAs, Pt foil, and the corresponding calculated electron structures for each sample. Reproduced with permission.^[6c] Copyright 2019, Nature Publishing Group.

L₂-edge of Pt SAs exhibited a substantial whiteline (WL), a sharp resonance in the absorption coefficient. The WL feature arises from dipole transition from Pt p to d band, indicating the presence of appreciable unoccupied DOS of Pt 5d_{5/2} and 5d_{3/2} above the Fermi level. From the analysis, Pt–Ru dimers and Pt SAs showed higher E_0 of 11 565.5 and 11 565.9 eV than that of 11 564.0 eV of Pt foil, indicating an increased unoccupied electron number of Pt 5d orbitals for Pt–Ru dimers and Pt SAs. Quantitative calculations indicated that Pt SAs from Pt–Ru dimers obtained high unoccupied DOS of 1.09, which was much higher than the character of Pt foil (0.70). The electronic character of Pt SAs is crucial in determining their electrochemical catalytic performance. Hence, XANES spectra have promising potential in identifying and quantifying the chemical and electronic environment of SAs. In addition to study chemical environment, the bonding structure of metal SAs can be further understood by analysis the EXAFS data.

3.2.2. EXAFS and Fitting Analysis of SACs

The XANES spectra can provide information about local electronic and chemical structure of central metal SAs. If we would like to understand the detailed information about the neighboring atom, coordination number (CN), and bonding distance of the central metal atom, EXAFS spectra analysis is in primarily demanded.

Li and co-workers used EXAFS spectra to investigate the atomic dispersion of Co, Fe atoms, and studied the coordination nature of M–Nx–C bonding in MOF-derived nanomaterial.^[21b,29a] The Fourier-transformed (FT) k^3 -weighted EXAFS spectra in **Figure 9a** showed that only a main peak at 1.5 Å attributed from the Fe–N(O) scattering can be detected in the FeSA/CN sample. By analysis high resolution wavelet transform (WT) EXFAS in both K and R spaces of Fe k-edge, it was found that the intensity maxima at 5 Å⁻¹ was associated with

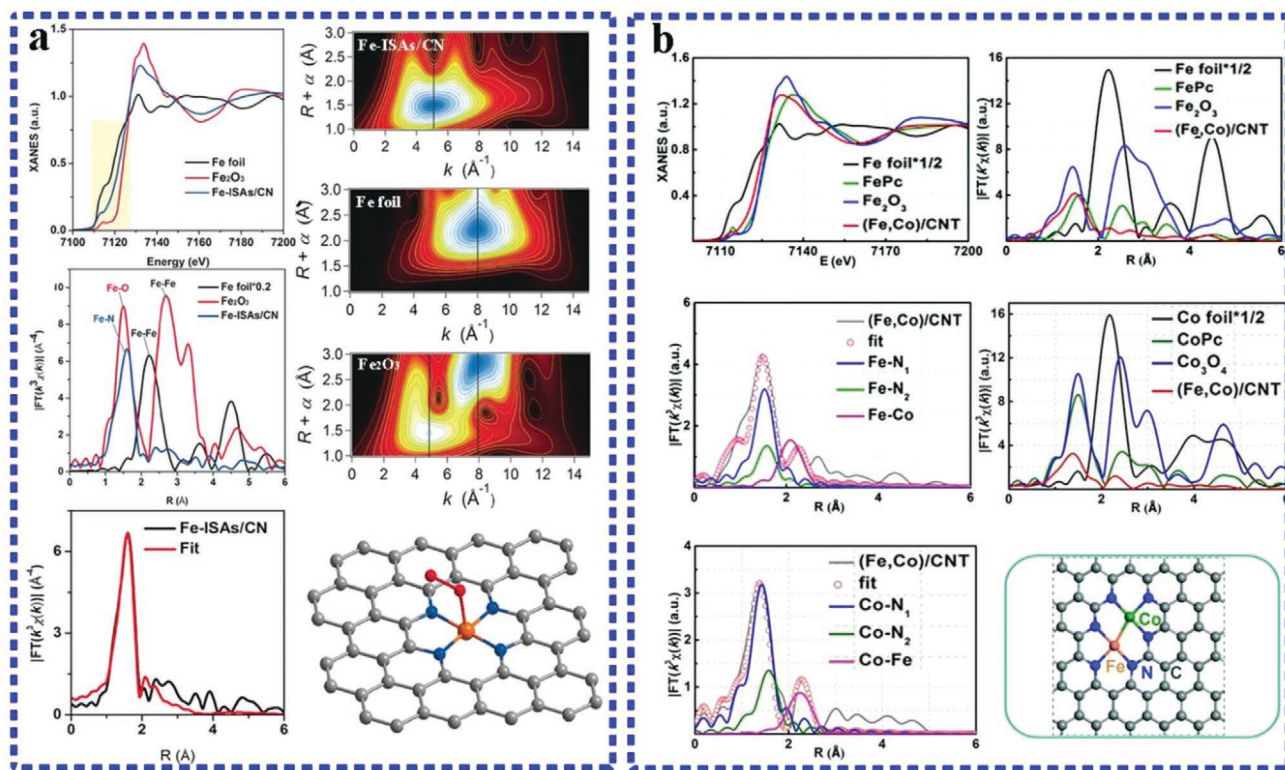


Figure 9. a) The XANES, FT-EXAFS, WT-EXAFS, corresponding EXAFS R-space fitting curves at Fe K-edge, and schematic model for Fe-ISA/CN. Reproduced with permission.^[29a] Copyright 2017, Wiley-VCH. b) XANES spectra, FT-EXAFS spectra for the Fe K-edge and Co K-edge of the (Fe,Co)/CNT, and proposed architecture of Fe–Co dual sites. Reproduced with permission.^[61a] Copyright 2018, Royal Society of Chemistry.

the Fe–N (O) scattering. The WT-EXAFS spectra of FeSA/CN displayed only the Fe–N(O) bonding at 5 \AA^{-1} without Fe–Fe bonding (at 8 \AA^{-1}), intuitive demonstrating the isolated dispersion of Fe atoms. To obtain the quantitative structural parameters of the central Fe atom, least-squares EXAFS fitting was performed for FeSA/CN sample. The coordination number of Fe was calculated to 4.8 and the average bond length was 2.01 \AA . Based on EXAFS fitting analysis, the local atomic structure was demonstrated to be Fe atoms anchored in the N-doped carbon and four-fold coordinated by N atoms. While one O_2 molecule was considered to adsorb on the Fe atom in the Fe– N_4 porphyrin plane, and the proposed architecture of Fe– N_4 – O_2 is shown in Figure 9a.

Moreover, EXAFS analysis can be applied to determine the bimetallic dimer structure. As shown in Figure 9b, k^3 -weighted FT-EXAFS spectra in R space for Fe K-edge suggested that Fe species presented as the Fe–N and Fe–Co moieties in the MOF-derived (Fe,Co)/CNT. The prominent peak at 1.48 \AA for the Fe K-edge was attributed to the scattering interaction between Fe atoms and N (Fe–N). An additional small peak appears at 2.22 \AA demonstrating the metal-metal dual bonds of Fe–Co. Fitting for EXAFS data and comparing between experimental and theoretical spectrum results revealed that the coordination of Fe in (Fe,Co)/CNT was Fe– N_3 (CN = 3.2) and Fe–Co (CN = 0.8). The additional EXAFS curve-fitting of reference (Fe,Co)/N–C at the Fe and Co K-edge by considering the structural model of Fe–Fe and Co–Co dual sites, further confirmed the well-defined dual coordination site of FeCoN_6 moiety in (Fe,Co)/CNT

sample. The FT-, WT-EXAFS, and theoretical fitting thereby are the powerful tools in revealing the unique electronic structure and coordination environment of metal SAs, which benefit in understanding effect active sites in boosting the high electrocatalytic activity.

3.2.3. In Situ XAFS Analysis of SACs

Operando/in situ XAFS with the potential for dynamic monitoring the electronic and structural properties of active centers during the electrochemical conversion, provides more relevant and deep insights in understanding the reaction mechanism and working mechanism of active sites.

New techniques of in situ X-ray absorption spectra were investigated to capture the dynamic structure of SACs during the oxygen reduction reaction (ORR).^[43a,45] For example, Xing and co-workers presented a MOF-strategy for preparation of SAC and revealed the nature of Fe– N_4 –C during the ORR by applying in situ XAFS.^[45a] It was found that the nonplanar Fe– N_4 configuration was a major presence in the Fe– N_4 –C sample. However, increasing the potential on the working electrode from 0.3 to 0.9 V (vs RHE) resulted in a positive shift in Fe K-edge XANES, indicating the $\text{Fe}^{2+/3+}$ redox transition. The sinusoidal shape and high amplitude of $\Delta\mu$ -XANES spectra demonstrated the Fe^{2+} – N_4 can be oxidized to Ox-Fe^{3+} – N_4 at high potentials (Figure 10a). Therefore, the in situ XANES revealed that the Ox-Fe^{3+} – N_4 undergoes an $\text{Fe}^{3+/2+}$ transition

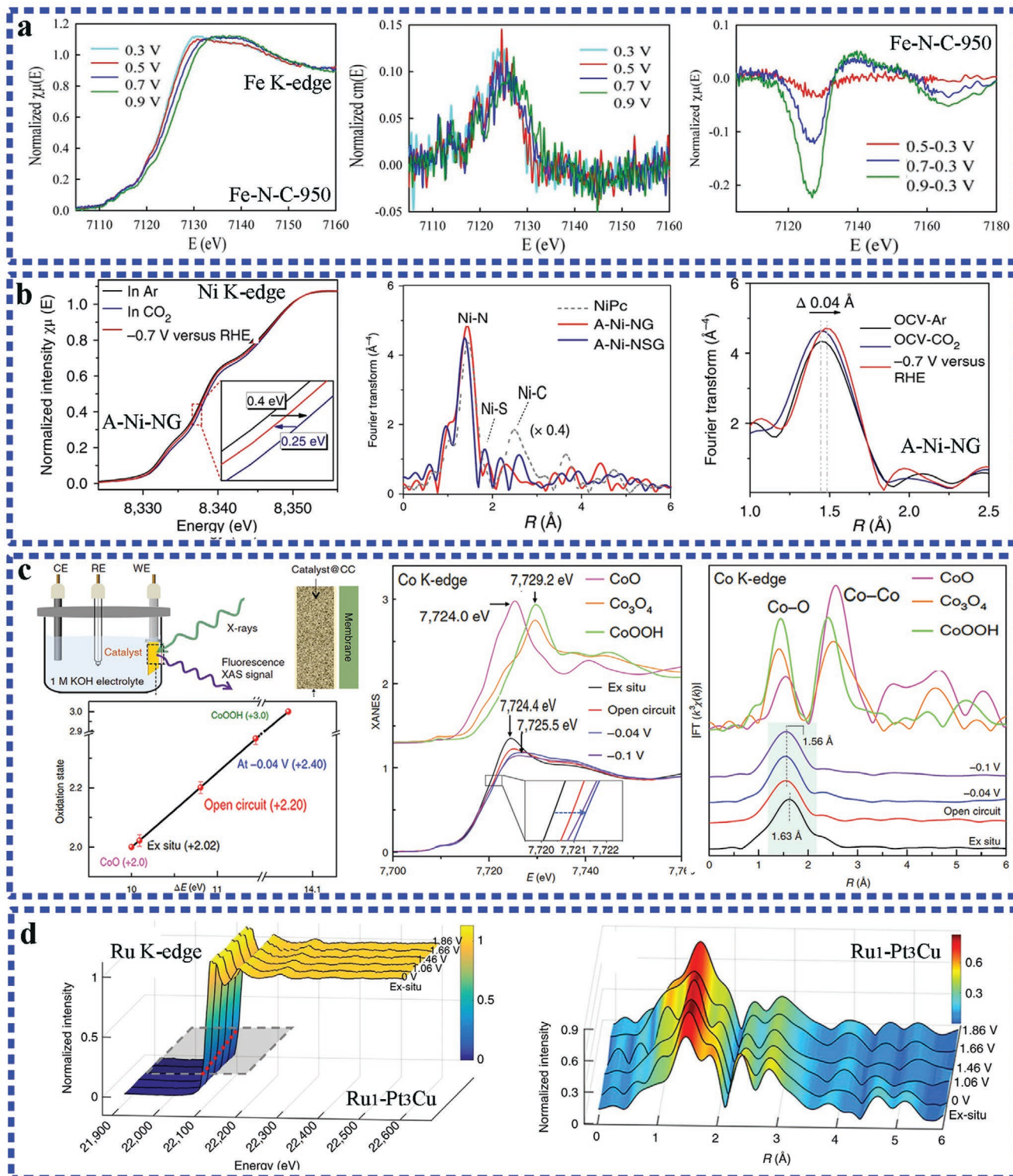


Figure 10. a) In situ XANES, first derivatives, and $\Delta\mu$ -XANES curves of the Fe-N-C-950 collected at 0.3–0.9 V on the electrode. Reproduced with permission.^[45a] Copyright 2018, American Chemical Society. b) Normalized operando Ni K-edge XANES spectra, ex situ and in situ FT-EXAFS spectra for A-Ni-NG at applied voltage in Ar/ CO_2 -saturated 0.5 M KHCO_3 medium. Reproduced with permission.^[46a] Copyright 2018, Nature Publishing Group. c) Schematic of the operando electrochemical cell set-up, operando XANES/EXAFS spectra recorded at the Co K-edge of Co₁/PCN and references at different applied voltages during electrocatalytic HER. Reproduced with permission.^[47a] Copyright 2018, Nature Publishing Group. d) In-situ XANES/EXAFS spectra change of the Ru K-edge for Ru₁-Pt₃Cu during the OER. Reproduced with permission.^[47b] Copyright 2019, Nature Publishing Group.

with potential decrease and the active site of nonplanar HO-*Fe(2+)-N₄ was in situ formed below the Fe^{2+/3+} redox potential. The freshly reduced HO-*Fe(2+)-N₄ as the effect active site thus achieved the excellent catalytic activity under the ORR conditions.

Additionally, the operando X-ray absorption spectroscopy has been performed on SACs to clarify the activation of CO₂.^[46] For example, Liu and co-workers observed that Ni K-edge of A-Ni-NG shifted 0.4 eV to higher energy in CO₂-saturated KHCO₃ compared with that in Ar-saturated KHCO₃ at open-circuit voltage, then it moved back to lower energy during the CO₂ reduction.^[46a] These results indicated the recovery of low-oxidation-state Ni sites after one cycle of electrochemical CO₂ reduction. Moreover, the main peak in FT-EXAFS for Ni-N shifted to longer length during CO₂ reduction at -0.7 V (vs RHE) compared with that under open-circuit voltage, suggesting the expansion and distortion of Ni-N bond with the adsorption of CO₂ on Ni SA sites (Figure 10b). Based on the operando XAFS and theoretical calculations, the monovalent Ni (I) atomic center with a d⁹ electronic configuration was determined as active sites in the CO₂ molecular activation and electrochemical reduction. In another work reported by Wang and co-workers, operando XAFS measurements were carried out for probing the coordination environment and electronic structure of Ni-SAs during the CO₂ reduction.^[46b] In-situ XAFS spectra at Ni K-edge of Ni-NG were recorded under different CO₂ electrocatalysis potential. No obvious changes in Ni XANES at various bases suggested the high stability of Ni-SACs, which ensured their long-term activity in the electrocatalysis application. Similar results on Co-SACs was reported by Deng and co-workers.^[46c] They conducted the in situ XAFS to probe the valence state and coordination structure of CoPc catalysts under the electrocatalytic CO₂ reduction conditions. Negligible changes were detected in either XANES or EXAFS spectra at the Co K-edge when applying -0.6 V (vs RHE) for CO₂ reduction, suggesting the maintenance of Co²⁺.

Besides electrochemical reduction reactions, operando XAFS is able to give deep insights into the nature of atomically dispersed active sites in water splitting reactions.^[47] Figure 10c presented a schematic of the operando XAFS set-up used for studying the Co SACs (Co₁/PCN) toward the hydrogen evolution reaction (HER).^[47a] By analyzing XANES spectra at Co K-edge of Co₁/PCN during the HER, it was discovered that the Co valence in Co₁/PCN under ex situ and operando conditions are close to those of CoO and Co₃O₄, respectively, suggesting the Co cations increased from +2 to a higher oxidation state under working conditions. In operando EXAFS analysis at Co K-edge discovered the oxidation state change of Co SAs and the rearrangement in their local atomic structure. It was monitored that the Co SAs undergo structural change to form a high-oxidation moiety of HO-Co₁-N₂. Then H₂O prefers to adsorb on HO-Co₁-N₂ to generate the intermediate H₂O-(HO-Co₁-N₂), which is responsible for the high HER activity. In another example, Li and co-workers prepared a series of Pt-Cu alloys with embedded Ru atoms as the oxygen evolution reaction (OER) electrocatalyst.^[47b] In situ XAFS studies were carried out to investigate the potential-dependent oxidation of Ru₁ during the OER. It was found that the oxidation

state of Ru₁ was almost unchanged within the OER potential range of 0–1.86 V (Figure 10d). Ru₁ active sites kept the same oxidation state during OER electrocatalysis, which was due to the possible charge compensation from the Pt-Cu alloy to Ru₁, thereby avoiding the overoxidation of Ru₁ and achieving excellent stability during the electrocatalysis.

The above-mentioned progress has clearly highlighted the powerful functions of operando/in situ XAFS technique in exploring the electronic structure of active sites at the atomic level during electrochemical reactions. To better understand the electrocatalytic reaction mechanisms, a combination of operando XAFS with other analytical techniques should be most effective.

3.3. X-ray Photoelectron Spectroscopy

X-ray photoelectron spectroscopy (XPS), as a highly surface-sensitive and element-specific technique, is powerful in studying surface elemental oxidation state and composition of heterogeneous catalyst. In addition, the in situ XPS technique under a synchrotron light source showed an important role in fundamental understanding thermal stability and active sites of SACs.^[37b,48]

In the work reported by Neyman and co-workers, the synchrotron radiation photoelectron spectroscopy (SRPES) was applied to investigate the chemical states and thermal stability of Pt SAs on CeO₂ support (0.3 nm Pt-CeO₂).^[48c] It was detected the ionic Pt exclusively in the oxidation states of +2 and +4. Upon thermal heating, the signal for Pt⁴⁺ in **Figure 11** rapidly decreases, indicating the unstable property of Pt⁴⁺. Surprisingly, the Pt²⁺ behave exceptional thermal stability up to high temperature of 750 K. Note that SRPES spectra were taken at low photo energy (180 eV) with high surface sensitivity (photoelectron mean free path 0.5 nm). The well-controlled surface-science SRPES technique show the increase of Pt²⁺ signal, suggesting that Pt²⁺ are anchored at the very surface of CeO₂ nanofacets and remain perfectly stable up to high temperature (750 K) without sintering or bulk diffusion. In another case, Liu and co-workers applied conventional XPS to evaluate the compositions of Ni SAs and their valences in N-doped graphene support (A-Ni-NG, A-Ni-NSG).^[46a] It was indicated that A-Ni-NG and A-Ni-NSG have high N contents (2.2 and 2.8 at% Ni-N) and N is in the pyridinic form (Figure 11e,f). The high-resolution XPS S_{2p} spectrum of A-Ni-NSG displayed a peak at 162 eV, which was assigned to the Ni-S bond and implied the atomic Ni-S-C coordination. The binding energy of Ni2p_{3/2} in A-Ni-NG and A-Ni-NSG were 855.0 and 854.8 eV in between of Ni⁰ at 853.5 eV and Ni²⁺ at 855.8 eV, which suggested the low-valent state of Ni atoms in A-Ni-NG and A-Ni-NSG. Combined with the Ni K-edge XANES spectra, the oxidation state of the Ni atoms was confirmed to be +1 with a 3d⁹, S = 1/2 electronic configuration in A-Ni-NG and A-Ni-NSG.

Results of these work disclose the significance of in situ and ex situ XPS technique for studying the surface composition, chemical states, and thermal stability of SACs. The utilization of XPS in identification of SACs for understanding the active sites under realistic conditions are highly encouraged in the ongoing research.

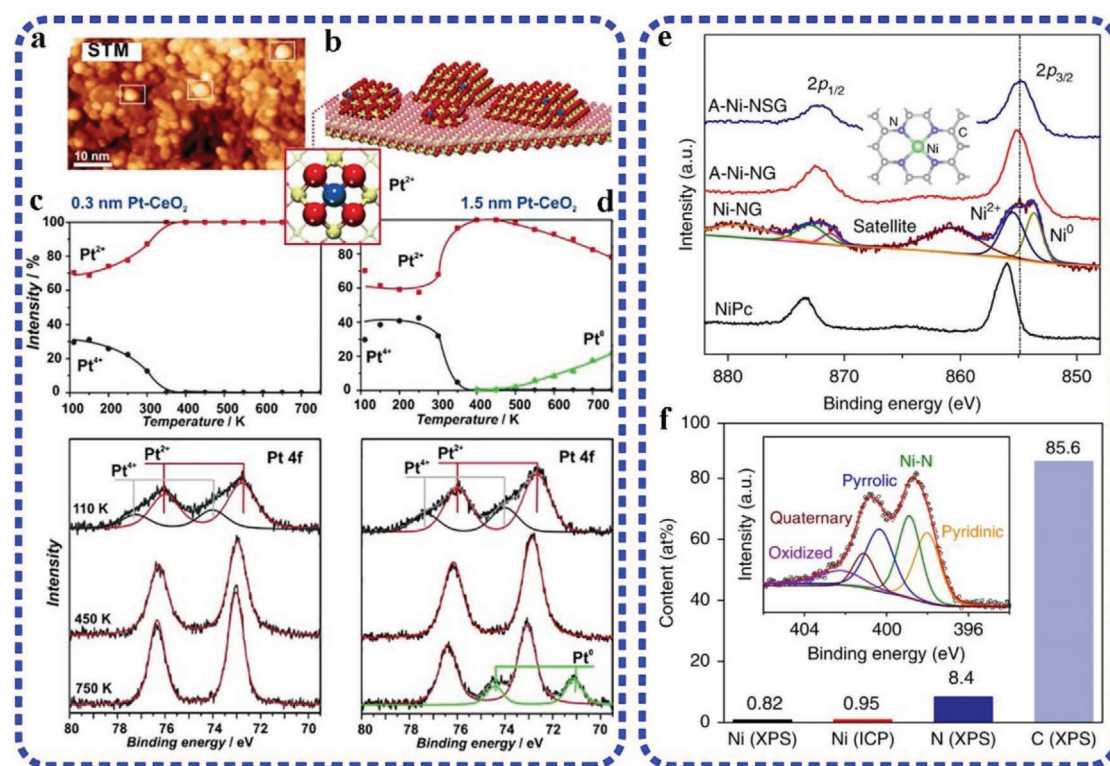


Figure 11. a) STM image and b) Schematic structure model of Pt–CeO₂ on a well-ordered CeO₂ (111) surface. Evolution of the Pt–4f core level XPS spectra as a function of annealing temperature at c) Pt–CeO₂ film thickness of 0.3 nm and d) Pt–CeO₂ film thickness of 1.5 nm. Reproduced with permission.^[48c] Copyright 2014, Wiley-VCH. e) high resolution XPS Ni 2p spectra in samples of A-Ni-NG, A-Ni-NSG, and Ni-NG. f) elemental content of A-Ni-NG obtained from XPS and ICP measurements. Reproduced with permission.^[46a] Copyright 2018, Nature Publishing Group.

3.4. IR Spectroscopy

Probe molecule infrared (IR) spectroscopy is one effective approach to identify and distinguish metal SAs from NPs. IR spectroscopy allows for monitoring the interaction between probe molecules and the metal surface. As chemical bonds form when probe molecules are adsorbed on the metal surface, therefore the structure of metal centers can be deduced by detecting the variation in vibrational frequency of probe modes. IR spectroscopy using CO as the probe molecule is widely used to identify metal structures based on peak position of CO_{ad}.^[10,49]

For example, Stair and co-workers showed the IR spectroscopy with CO as a probe molecule that can differentiate and quantify Pt SAs from NPs.^[49a] The IR spectra (Figure 12a) of adsorbed CO on four Pt/HZSM-5 samples with different Pt loadings (0.5–2.6 wt%) revealed two sets of CO adsorption bands centered at 2115 and 2070–2090 cm⁻¹. Combined with HAADF-STEM, the IR peak at 2115 cm⁻¹ was attributed to CO adsorbed on Pt SAs, while the predominant peak at 2070–2090 cm⁻¹ corresponding to CO adsorbed on Pt NPs. In addition, the CO adsorbed on Pt SAs remained unchanged after undergoing oxidation treatments, indicating the strong binding interaction of CO molecule to Pt SAs (Figure 12b). Stronger binding energy of CO to Pt SAs than that to Pt NPs resulted in lower catalytic activity of Pt SAs toward CO oxidation. To examine the nature of Pt active sites during reaction

conditions, Datye and co-workers performed diffuse reflectance infrared Fourier transform (DRIFT) of the 1.0 wt% Pt/CeO₂ catalyst.^[30] Before exposing to reaction conditions of CO:O₂ = 1.5:1, the Pt/CeO₂ sample was subjected to an oxidative treatment with 10% O₂/He at 450 °C. The DRIFT spectra in Figure 12c demonstrated a prominent characteristic peak of CO on ionic Pt for the 1.0 wt% Pt/CeO₂ sample, even at 350 °C during CO oxidation, suggesting the high stability of isolated Pt SAs on CeO₂ support. Additionally, it was found that only at higher temperatures that the Pt SAs on CeO₂ become active and exhibit outstanding specific activity for CO oxidation. However, in another example, Christopher and co-workers demonstrated a catalyst architecture where isolated Pt species are dispersed on TiO₂ NPs, which showed good CO oxidation activity.^[10] Combining with correlated STEM image and CO probed IR, distinguished IR signatures of CO adsorption to Pt isolated atoms (Pt_{iso}), Pt oxide clusters (Pt_{ox}), and Pt metal clusters (Pt_{metal}) on TiO₂ were identified (Figure 12d–f), which allowed rapid characterization of various Pt sites. Obtained from the spectroscopic signatures, the order of CO adsorption energy on Pt sites was revealed to be Pt_{iso} < Pt_{metal} < Pt_{ox}, where adsorbed Pt_{ox} was essentially inactive for oxidation of CO at the temperature below 200 °C. Rigorous kinetic examination for steady-state CO oxidation showed that the interfacial Pt_{iso} atoms connected with TiO₂ were inherently reactive. This work revealed that isolated Pt SAs on certain reducible supports could provide the most efficient metal utilization for CO oxidation.

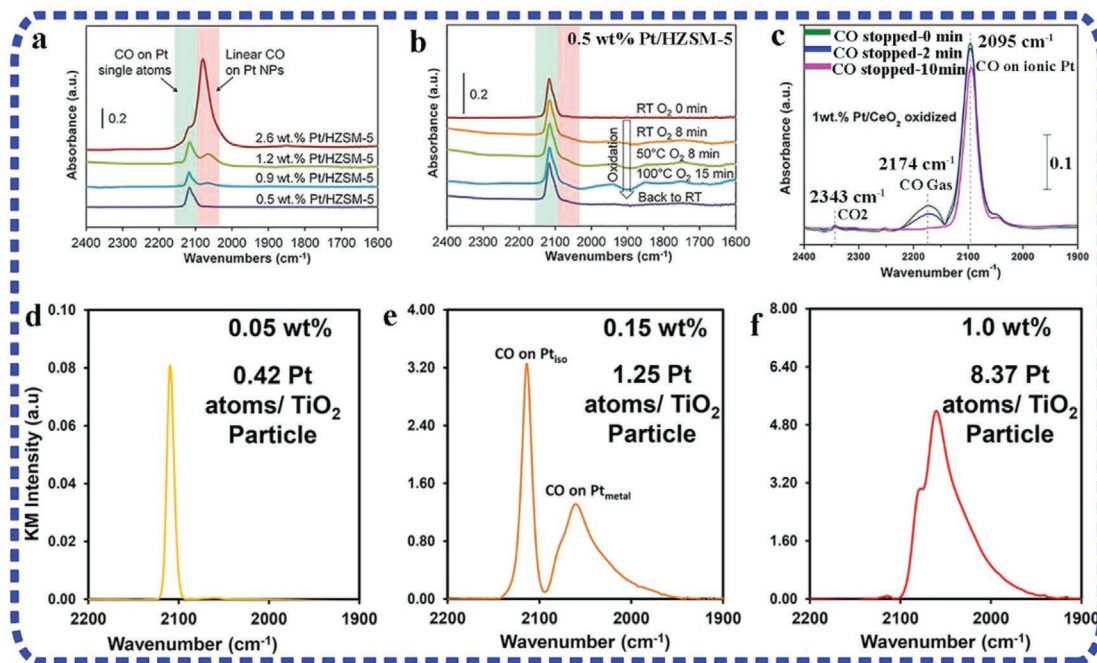


Figure 12. a) IR spectra of CO adsorbed on different Pt/HZSM-5 after the desorption processes. b) Time-dependent IR spectra of CO adsorbed on 0.5 wt% Pt/HZSM-5 during the oxidation process. Reproduced with permission.^[49a] Copyright 2015, American Association for the Advancement of Science. c) DRIFTS of the 1.0 wt% Pt/CeO₂ during CO oxidation at 125 °C after oxidative pretreatment in 10% O₂ at 450 °C. Reproduced with permission.^[30] Copyright 2016, American Association for the Advancement of Science. d–f) IR spectra of CO adsorbed at saturated coverage to 0.05 wt% Pt/TiO₂, 0.15 wt% Pt/TiO₂, 1.0 wt% Pt/TiO₂ catalysts, respectively. Reproduced with permission.^[10] Copyright 2017, American Chemical Society.

3.5. DFT Calculations of SACs

Besides physical and chemical characterizations of SACs, the theoretical computations based on DFT are being performed to study catalyst properties at the atomic level. By resorting to DFT calculations, the most stable configuration of supported SACs and reaction mechanisms can be confirmed, which provide perspectives in determining the atomic structure and characters of SACs.

Wu and co-workers carried out molecular dynamics simulations and DFT calculations to elucidate the formation mechanism of atomically dispersed FeN₄ sites through high temperature converting from FeOx particles.^[50] DFT calculations predicted that 5.38 eV was required to remove an Fe atom from the FeOx particle. If the removed Fe atom was adsorbed in a N₄ vacancy moiety, the system energy would significantly decrease by 6.44 eV. Therefore, it is thermodynamically favorable for ultrafine FeOx particles to lose Fe atoms and form more stable FeN₄ sites. The driving force from FeOx to Fe SACs is the potential energy decrease of the FeN₄ as compared to that of an isolated N₄ vacancy and individual Fe atom (Figure 13a). Therefore, DFT simulations provide a mechanism understanding in FeN₄ site formation. Additionally, DFT calculations can be used to well understand the active sites origin and to explain electrocatalysis reaction pathway in chemical conversion reactions. Taking the ORR as an example, the adsorption and desorption energy of ORR intermediates on FeN₄ are indicated (Figure 13b). DFT results in Figure 13c,d demonstrated that FeN₄ sites with contracted Fe–N configuration and shortened Fe–N bonding distance showed low activation energy in

breaking O=O bond, which enhanced the reaction kinetics and favored ORR activity.

Moreover, computational modeling can be used to study the interactions between isolated metal SAs and support to understand the stability of SACs. Zhang and co-workers reported that isolated Pt atoms can be stabilized through strong covalent metal-support interaction, yielding a high loading and thermally stable SAC by trapping Pt atoms on the nondefect support.^[38a] Calculations indicated that the reactive Pt atoms were coordinated with four surface oxygen atoms in a distorted square geometry with a Pt–O length of 1.94 Å. The evaporation free energy of PtO₂ from a Pt (221) step was about –0.61eV per PtO₂ at 800 °C, whereas the evaporation energy of Pt₁ reached as high as 4.00 eV, and hence atomic Pt₁ was energetically stable due to the strong interaction between Pt₁ and the support. Moreover, it was found that the Fe₂O₃ support favors atomically dispersed Pt, whereas Al₂O₃ favors Pt NPs sintering as shown in Figure 13e. The stability of SACs is closely related to the reducibility of the metal oxide support. The DFT calculations in Figure 13f revealed the mechanism of nondefect support in anchoring SAs, which may afford a generic route to fabricate high loading of stable SACs over diverse reducible supports.

Overall, to fully understand the electronic structure and related electrochemical properties of SACs, it is important to develop the advanced characterization techniques. Particularly, combining both ex situ and in situ characterizations is essential to determine the structure–performance relationships of SACs during electrochemical reactions. Moreover, theoretical calculations of more complex reaction systems are required in order

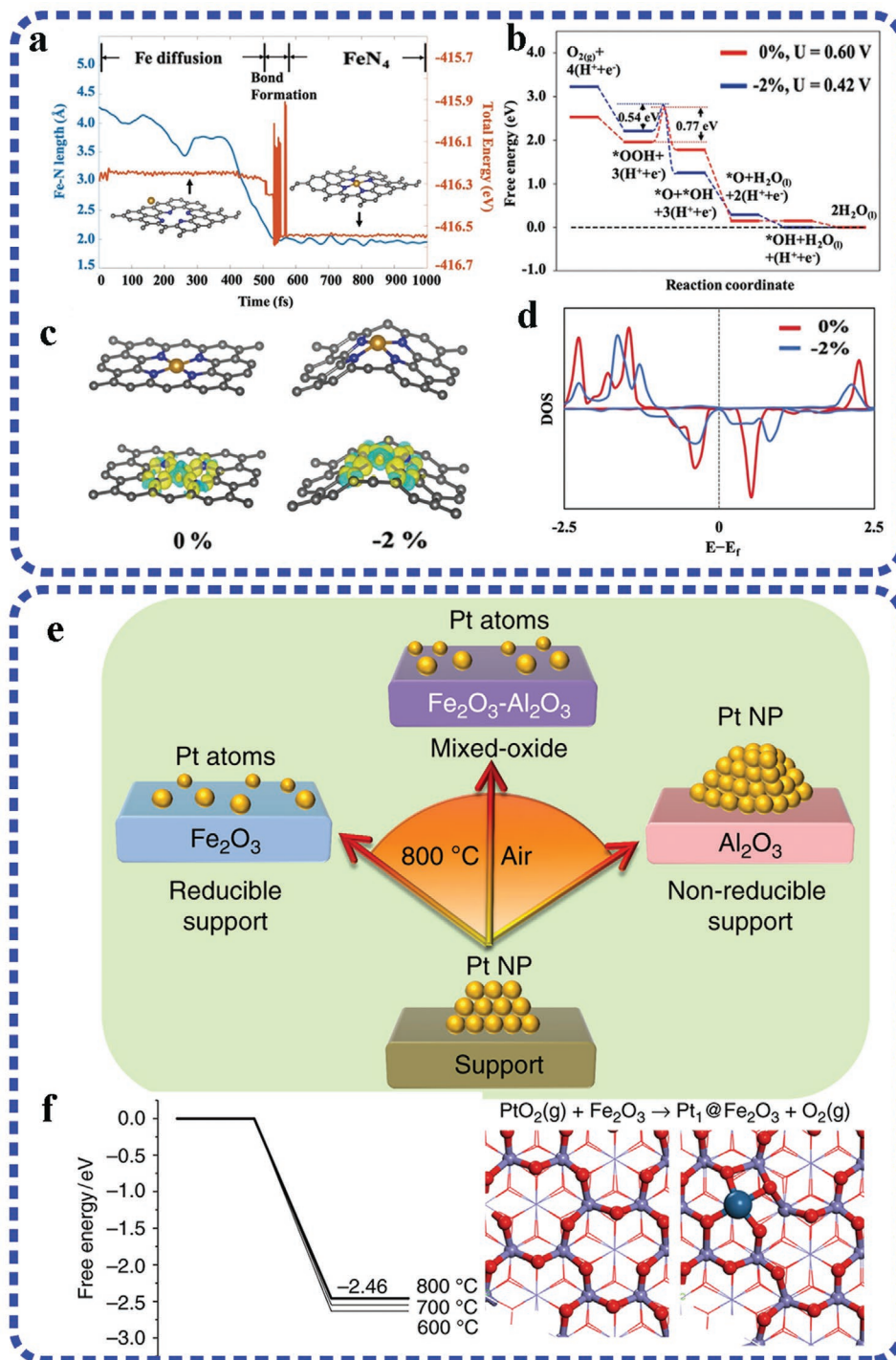


Figure 13. a) Molecular dynamic simulation on the formation of FeN₄ sites. b) DFT calculated ORR free energy evolution on the fully relaxed FeN₄ site (0%) and on the FeN₄ site with 2% shorten Fe–N bonds. c) Geometric structure of fully relaxed 0% FeN₄ and with 2% Fe–N bond of contracted FeN₄. d) DOS of the 3d orbitals of the Fe ion in two model FeN₄ sites. Reproduced with permission.^[50] Copyright 2019, Wiley-VCH. e) Illustration of Pt NPs dispersing and sintering on different supports. f) Calculated energy and surface structures for capture of PtO₂ over Fe₂O₃ to form Pt₁ atoms. Reproduced with permission.^[38a] Copyright 2019, Nature Publishing Group.

to confirm and support the experimental results, which benefit in identifying SACs structure accurately and understanding the origin of reaction mechanism for SACs in boosting electrochemical reactions.

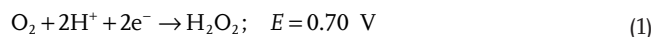
4. Electrochemical Application of MOF-Derived SACs

SACs with atomically dispersed active sites and maximum atom utilization efficiency, have recently emerged as a new frontier in

electrocatalysis. The electrochemical devices of fuel cells, Zn-air battery, water splitting and CO₂ reduction require electrochemical reactions at each electrode. In the case of fuel cells, the ORR occurs at the cathode, and fuel oxidation happens at the anode. Due to the sluggish kinetics of the ORR, there is a requirement of large use of Pt-based noble metal catalysts at the cathode. To decrease noble metal catalyst loading while not impacting the electrocatalytic performance, the synthesis of single-atom catalysts has been recognized to be an efficient way in boosting the catalytic performance. On the other hand, electrochemical catalysis water splitting, such as the OER and HER in anode and cathode, requires the noble metal catalysts of Pt, Ru and Ir etc. Downsizing noble metal catalysts to SACs is desirable in water splitting. Moreover, initial attempts and DFT calculations suggested that SACs can be good catalysts for CO₂ reduction reaction (CO₂RR) and nitrogen reduction reaction (NRR). In this section, we summarize the recent progress of MOF-derived SACs in application of electrochemical conversion reactions, such as the ORR, CO₂RR, NRR, HER, and OER. Different kinds of metal-based SACs, active sites structures, and their effect on electrocatalytic activity and selectivity will be discussed.

4.1. MOFs-Derived SACs for the ORR

Under the electrocatalysis of SACs, the ORR proceeds by either a two-electron pathway via reduce O₂ into peroxide (H₂O₂) in the acidic media



or in a four-electron pathway to produce H₂O in acidic solution



It has been reported that catalyst particle size has a significant impact on the ORR performance due to the different intermediates' adsorption/desorption energy. When downsizing catalysts NPs to SAs, the reduction of peroxide intermediate (H₂O₂) can be suppressed accompanied with H₂O₂ diffusion into the electrolyte instead of its further decomposition. As a result, the ORR product of H₂O₂ other than H₂O is generated through a 2-electron pathway. Nowadays, the MOF-derived noble metal, and non-noble metal SACs have been reported to be electrocatalysts for the ORR.

4.1.1. Noble Metal SACs for the ORR

Yu and co-workers reported a precise modulation at the atomic level by a "single-atom to single-atom" grafting of Pt atoms onto Fe atoms in Fe-N₄-C support through a bridging oxygen molecule (Pt₁/Fe-N-C).^[51] A top level loading of 2.1 wt% Pt SAs has been achieved on Fe-N-C matrix. Electrochemical measurement indicated that Pt₁/Fe-N-C catalyst exhibited high catalytic activity in the four-electron pathway to reduce oxygen into H₂O. It was exciting to find that Pt₁/Fe-N-C catalyst achieved a considerably improved durability during catalyzing the ORR in

acidic media. The primary stable mechanism was the mitigated H₂O₂ attack to the catalyst due to the protection of Pt₁-O₂-cap on the Fe atom.

It should be noted that the support material plays a significant role in tuning the ORR pathway for SACs. The interaction between support and Pt single-atom is closely related to the SACs activity and stability, which can even change the reaction mechanism from a four-electron to two-electron pathway toward ORR.^[2b,51,52] For example, the ORR performance of Pt/HSC catalyst with isolated Pt SAs supported on the sulfur-doped carbon (HSC) was studied by Choi and co-workers.^[53] The abundant S-species (17 wt% S) and highly curved 3D carbon networks are able to stabilize Pt atoms with high loading of 5 wt%. Considering the ORR activity under acidic environment, the Pt_{SAs}/HSC catalyst does not follow a typical four-electron pathway producing H₂O, but predominantly produces H₂O₂. Rotating ring disk electrode (RRDE) experiments revealed that Pt_{SAs}/HSC produces H₂O₂ with up to 96% selectivity, suggesting the ORR reaction occurs through a two-electron pathway (electron number = 2.1). This work indicated that the support materials not only provide the anchoring sites for stabilizing SAs, but also play a critical role in tuning the surface reaction mechanism.

Several noble metal SACs have been developed as electrocatalysts for the ORR, which show high electrocatalytic activity and selectivity during the reactions. By tuning the metal-support interaction, and optimizing the support material, the ORR to H₂O₂ or H₂O products under 2-electron or 4-electron pathway can be achieved.

4.1.2. Non-Noble Metal SACs for the ORR

Co-Based SACs: The MOF strategy has been investigated as an effective approach to fabricate non-noble metal SACs. Among them, transition metals such as Co, Fe, Mn, Cu, Zn-based SAs have been examined in electrocatalysis of the ORR. In 2016, Li and co-workers reported the Co-SACs with high loading of Co SAs (4.0 wt%) embedded in N-doped carbon (Co_{SAs}/N-C) as electrocatalysts for the ORR.^[21a] As shown in **Figure 14a**, the Co_{SAs}/N-C catalysts exhibit superior ORR performance in 0.1 M KOH with a half-wave potential (*E*_{1/2}) of 0.881 V (vs RHE) which was more positive than that of 0.811 V (vs RHE) for commercial Pt/C. The ORR activity was better for the sample of Co_{SAs}/N-C with CoN₂ active centers than that with CoN₄ species. The RRDE testing demonstrated nearly four-electron ORR pathway over the Co-N₂ active sites. DFT calculations proved that Co-N₂ species showed stronger interaction with hydrogen peroxide than Co-N₄. Thereby, Co-N₂ species from Co_{SAs}/N-C promote further oxidation of H₂O₂ and lead to the four-electron oxygen reduction to H₂O. Wu and co-workers used a similar MOFs strategy to obtain the Co-NC SACs consisted with CoN₄ moieties incorporated in porous carbon matrix.^[20,22] Through investigation of the effect of Co SAs content and pyrolysis activation temperature, the optimal Co-SACs with planar CoN₄ active sites can achieve excellent electrochemical activity and stability for the ORR in challenging acidic media (0.5 M H₂SO₄).^[20] It was found that 20Co-NC-1100 activated at 1100 °C with an optimal 20 at% Co atoms (20 at%

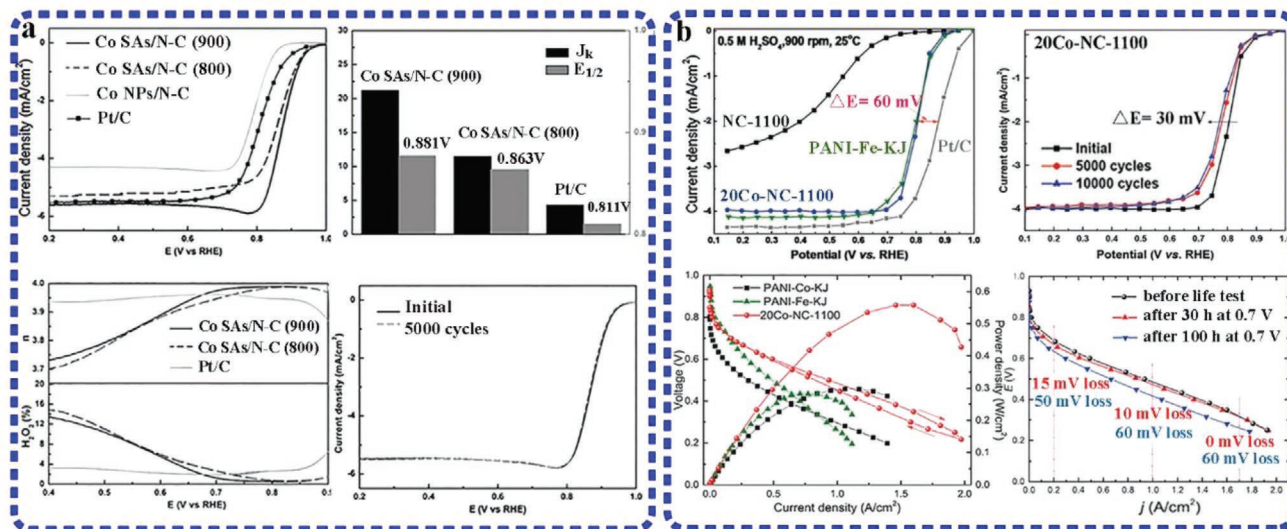


Figure 14. a) RDE polarization curves of Co SAs/N-C and counterparts in 0.1 M KOH. Comparison of $E_{1/2}$ and J_k for different catalysts. Electron transfer number and H_2O_2 yield. ORR polarization curves of Co SAs before and after 5000 potential cycles in O_2 -saturated 0.1 M KOH. Reproduced with permission.^[21a] Copyright 2016, Wiley-VCH. b) ORR polarization curves of Co-ZIF derived catalysts. Potential cycling stability in O_2 -saturated 0.5 M H_2SO_4 . H_2 - O_2 fuel cell polarization curve: cathode 4.0 mg cm^{-2} , anode 0.2 mg cm^{-2} . 100 h durability test under H_2 - O_2 polarization curves before and after the life test at 0.7 V. Reproduced with permission.^[20] Copyright 2018, Wiley-VCH.

Co in total metals of Co and Zn; 3.5 at% N) showed the best performance in acidic media, displaying much positive onset potential (E_{onset}) and half-wave potential ($E_{1/2}$) of 0.93 and 0.80 V (vs RHE), respectively (Figure 14b). Applied as the practical non-noble metal catalyst in polymer electrolyte membrane fuel cells (PEMFCs), the H_2/O_2 fuel cell using 20Co-NC-1100 as cathode exhibited high performance with the peak power density of 0.56 W cm^{-2} , and long-time stability after 30 and 100 h operation.

Fe-Based SACs: It has been reported that the electrocatalytic activity of transition metal-based M-Nx-C catalysts follows the order of Fe > Co > Mn > Cu > Ni in both acid and alkaline electrolyte. With the advantage of high activity, Fe appears to be the most promising transition metal to replace noble metal catalysts for the ORR. MOF-derived Fe SACs have received great attention due to their satisfying ORR performance.^[2e,28a,29a,45a,50,54] Experiments and theoretical calculations indicate that Fe-Nx active centers located on conductive support show comparable ORR activity to that of Pt catalysts. For example, Chen and co-workers reported an effective host-guest chemistry strategy to construct the MOF-derived Fe_{SA} -N/C electrocatalyst for ORR.^[54d] Electrochemical tests showed that the 5% Fe_{SA} -N/C catalyst with abundant five-coordinated N-Fe-N₄ sites displayed current density of 5.12 mA cm^{-2} at 0.4 V versus RHE for the ORR, comparable to that of 30%Pt/C catalyst in 0.5 M H_2SO_4 media. To deeply understand the relationship between Fe-Nx active sites and electrocatalytic performance, DFT calculations were performed. The results suggested that definite N-Fe-N₄ sites with coordination number of 5 are the active centers which originate the four-electron ORR pathway via narrowing the reaction energy barrier in the rate-determine step for the Fe_{SA} -N/C.

Li and Wang et. al prepared a highly stable Fe-based SAC via the cage-encapsulated-MOF pyrolysis strategy.^[29a] The as-prepared Fe_{SAs} /NC catalyst composed of isolated Fe SAs anchored

in the N-doped carbon which exhibited high activity with kinetic current density (J_k) of 37.85 mA cm^{-2} at 0.85 V, and $E_{1/2}$ of 0.9 V (vs RHE) in 0.1 M KOH, 58 mV more positive than that of commercial Pt/C. Moreover, the Fe_{SAs} /NC catalyst also showed excellent methanol tolerance and long-time stability, reflecting as negligible current change in the presence of 1.0 M methanol and little ORR polarization curve degradation after 5000 potential cycles. In another example, Wang and Chen reported the edge-site engineering of atomically dispersed Fe-N₄ sites embedded in the micro-mesoporous carbon, through pyrolysis of iron phthalocyanine (FePc) encapsulated ZIF-8 precursor.^[54e] As shown in Figure 15a, the Fe-N₄ sites anchored in 3D hierarchically porous carbon with 0.2 wt% of Fe atoms (Fe_{SAs} -N/C-20) demonstrated excellent ORR performance with $E_{1/2}$ of 0.915 V (vs RHE) in 0.1 M KOH, better than that of commercial Pt/C ($E_{1/2}$ = 0.85 V) and most reported M-Nx-C catalysts (Table 1). Moreover, the remarkable stability and \approx 10 times greater atom utilization efficiency were revealed by the 0.2 wt% Fe_{SAs} -N/C-20 catalyst. Experiment and DFT calculations demonstrated that porosity engineering enables the selective C-N bond cleavage adjacent to Fe centers to generate edge-hosted Fe-N₄ sites, which reduce the overall ORR free energy change and thus enhance the catalytic activity and long-term durability.

It is well accepted that doping heteroatoms within the skeleton of carbon matrix can adjust the electronic feature and electrical conductivity of SACs. Modifying the Fe-Nx active centers through doping extra elements is one of the approaches in tuning catalytic performance of SACs. Li and co-workers developed a polymer coated MOF strategy to fabricate Fe-SAC with isolated Fe SAs supported on a nitrogen, phosphorous and sulfur multidoped hollow carbon polyhedron (Fe_{SAs} /NPS-HC).^[55] Benefiting from the unique physical and electronic structure, the Fe_{SAs} /NPS-HC catalyst accelerated the ORR kinetics and achieved superior activity, showing a positive

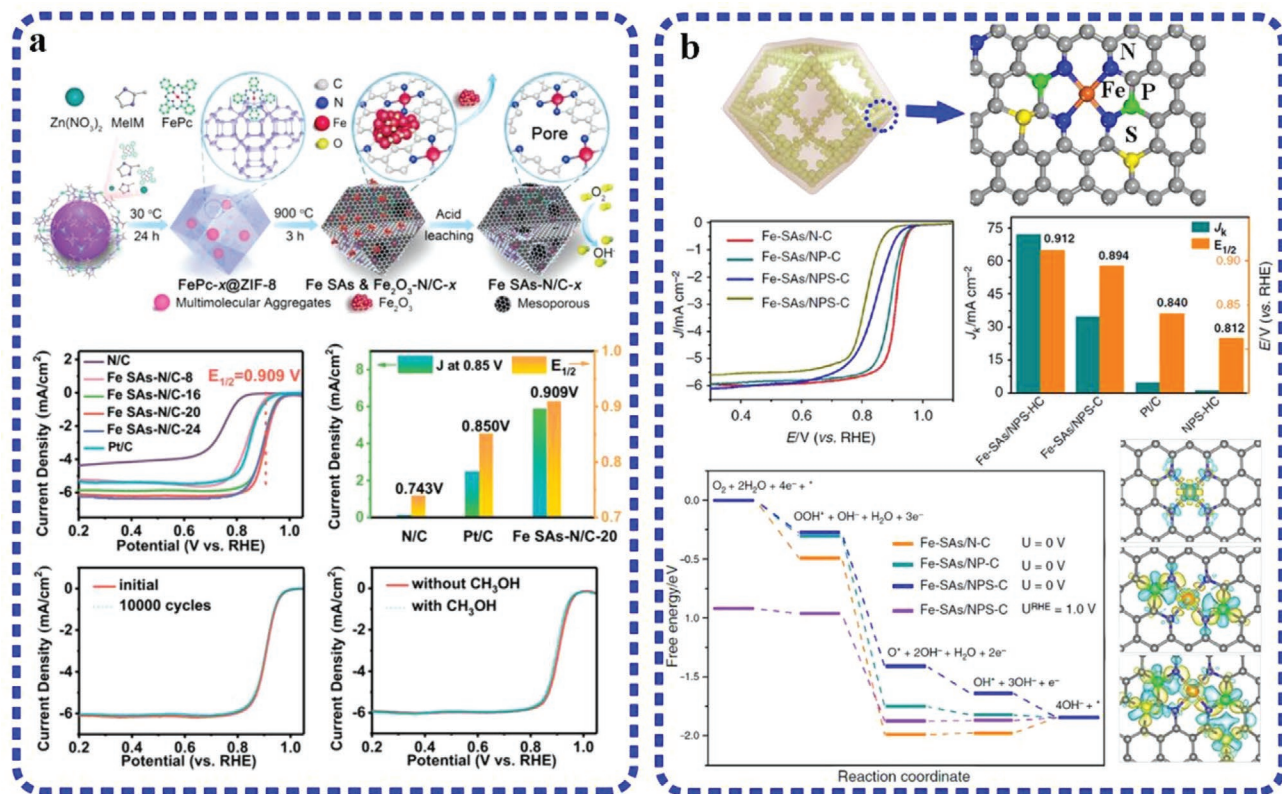


Figure 15. a) Schematic illustration of FeSAs-N/C-x synthesis; LSV curves, comparison of J_k and $E_{1/2}$, LSV curves before/after 10 000 cycles and without/with 1.0 M CH₃OH of FeSAs-N/C-x catalyst. Reproduced with permission.^[54e] Copyright 2018, American Chemical Society. b) Scheme of atomic structure of Fe SAs supported on N, P, S codoped carbon polyhedron (FeSAs/NPS-HC); electrocatalytic ORR performance, comparison of J_k and $E_{1/2}$ of FeSAs/NPS-HC with reference catalysts; free energy diagram of the ORR on FeSAs/N-C, FeSAs/NP-C, and FeSAs/NPS-C. Reproduced with permission.^[55] Copyright 2018, Nature Publishing Group.

half-wave potential of 0.912 V (vs RHE), better than that of Pt/C (0.9840 V vs RHE) in the O₂-saturated 0.1 M KOH. As illustrated in Figure 15b, the kinetic current density (J_k) of 71.9 mA cm⁻² at 0.85 V for FeSAs/NPS-HC was approached, which was 15 times higher than that of Pt/C (4.78 mA cm⁻²), suggesting the excellent catalytic activity of FeSAs/NPS-HC toward ORR. Beyond the evaluation of ORR performance in an electrochemical cell, the application of FeSAs/NPS-HC catalyst in energy conversion devices of Zn-air battery and H₂-air fuel cell was further investigated in their work. The Zn-air battery assembled with FeSAs/NPS-HC cathode exhibited an open circuit voltage of 1.45 V and the maximum power density up to 195.0 mW cm⁻² (at current density of 375 mA cm⁻²), which outperformed that of Pt/C-catalyzed Zn-air battery. Moreover, the performance of PEMFCs composed with FeSAs/NPS-HC cathode was exploited to understand its ORR performance in the device application. The Fe-SAs/NPS-HC-based PEMFC obtained a remarkable current density of ≈ 50 mA cm⁻² at 0.8 V and the peak power density of 333 mW cm⁻², which achieving $\approx 92\%$ power density of the commercial Pt/C-based PEMFC. DFT calculations revealed that the atomically distributed Fe-N active sites and the electronic effect arising from long-range S and P atoms that contributes to high efficiency and enhanced kinetics for the 4e⁻ ORR pathway of FeSAs/NPS-HC catalyst.

To develop highly active and stable SACs, fabricating the high density of isolated Fe-N_x atomic sites and avoiding their agglomeration is essential in delivering enhanced ORR activity. To approach SACs with high metal loading, Jiang and co-workers creatively put forward a nanocasting SiO₂ strategy into a porphyrinic MOF for design high loading Fe SACs.^[28b] Due to the dual protection from SiO₂ barrier and spatial isolation of Fe atoms anchored by N atoms, the high loading of 3.46 wt% Fe was obtained in FeSAs-N-C (Figure 16a). After removal of SiO₂, the optimized FeSAs-N-C with high Fe SAs loading (3.46 wt%) and exposed active sites exhibited outstanding ORR performance. In the alkaline media of 0.1 M KOH, FeSAs-N-C showed the highest half-wave potential of $E_{1/2} = 0.90$ V and kinetic current density of 37.19 mA cm⁻² at 0.85 V. The mass activity of FeSAs-N-C was up to 21.36 mA g⁻¹ at 0.9 V, much better than that of FeNP-N-C and counterparts. Moreover, FeSAs-N-C exhibited excellent ORR activity and durability in the more challenging acidic condition (0.1 M HClO₄), with high $E_{1/2}$ of 0.80 V and mass activity of 1.12 mA g⁻¹ (at 0.9 V). In the acidic PEMFC application, FeSAs-N-C as cathode catalyst also demonstrated excellent performance indicating a remarkable current density of 292 mA cm⁻² at 0.8 V and peak power density of 0.68 W cm⁻², which is among the highest activity of non-Pt cathode reported in PEMFC (Table 1). The KSCN poison experiment to FeSAs-N-C

Table 1. Summary of MOF-derived SACs for the ORR.

Catalyst	Metal SAs loading	Electrolyte	Half-wave potential [V] (vs RHE)	Electron transfer number	H ₂ O ₂ yield	Tafel slope [mV dec ⁻¹]	ORR kinetic current [mA cm ⁻²]	Active sites	Durability	Fuel cell/battery power density [W cm ⁻²]	Ref.
20Co _{SA} /N-C-1100	0.34 at%	0.5 M H ₂ SO ₄	0.80	≈4	≈5%	–	–	Co–N ₄	30 mV loss after 10 000 CV cycles	0.56	[20]
Co _{SA} /NC@F127	1.0 at%	0.5 M H ₂ SO ₄	0.84	≈4	<2.0%	–	–	CoN ₂₊₂	40 mV loss after 30 000 CV cycles	0.87	[22]
Co _{SA} –NC-900	4.0 wt%	0.1 M KOH	0.881	≈4	<14%	75	≈21 @ 0.80 V	Co–N ₂	No loss after 5000 CV cycles	–	[21a]
Co–N–C-10	4.3 wt%	0.1 M HClO ₄	0.79	≈4	2.0%	55.8	–	Co ₂ –N ₅	12 mV loss after 20 000 CV cycles	0.418	[91]
Fe–N/C	5.0 wt%	0.5 M H ₂ SO ₄	0.735	3.98	<1.0%	55.6	12.03 @ 0.70 V	N–Fe–N ₄	–	–	[54d]
Fe _{SA} /NC	2.16 wt%	0.1 M KOH	0.900	3.9	<5.0%	58	37.83 @0.85V	Fe–N ₄	2 mV loss after 5000 CV cycles	–	[29a]
Fe _{SA} –N/C-20	0.20 wt%	0.1 M KOH	0.915	3.8	–	–	–	Fe–N ₄	–	–	[54e]
Fe _{SA} –N–C	1.76 wt%	0.1 M KOH	0.891	3.9	<5.5%	–	23.27 @0.85V	Fe–N–C	6 mV loss after 5000 CV cycles	–	[28a]
Fe _{SA} /NPS-HC	1.54 wt%	0.1 M KOH	0.912	3.96–3.99	4.2%	36	71.9 @0.85 V	Fe–N ₄ –PS	No loss after 5000 CV cycles	0.195	[55]
Fe _{SA} /NPS-HC	1.54 wt%	0.5 M H ₂ SO ₄	0.791	3.95	<2.8%	54	18.8 @0.85 V	Fe–N ₄ –PS	5 mV loss after 5000 CV cycles	0.333	[55]
Fe _{SA} –N–C	3.46 wt%	0.1 M KOH	0.9	≈4	–	–	37.19 @0.85 V	Fe–N–C	–	–	[28b]
Fe _{SA} –N–C	3.46 wt%	0.1 M HClO ₄	0.8	≈4	–	–	6.14 @0.8 V	Fe–N–C	–	0.68	[28b]
Fe/OES	6.24 wt%	0.1 M KOH	0.85	3.8–4.0	1.1–13%	–	–	–	13.3% loss after 30 000 s	0.1868	[56]
Mn _{SA} –N–C	3.03 wt%	0.5 M H ₂ SO ₄	0.8	≈4	<2.0%	80	–	Mn–N ₄	17 mV loss after 30 000 CV cycles	0.46	[57]
Cu _{SA} –N–C	0.54 wt%	0.1 M KOH	0.895	3.96	<3.75%	63	≈7.5 @0.90 V	Cu–N ₄	No loss after 5000 CV cycles	–	[33a]
Cu _{ISA} /N–C	0.45 wt%	0.1 M KOH	0.92	3.99	–	59	8.87@0.9 V	Cu–N ₃ –V	Stabile after 20 000 cycles	0.28	[58]
Zn _{SA} –N–C	5.64 wt%	0.1 M HClO ₄	0.746	≈4	<5.0%	–	–	Zn–N ₄	19.9 mV loss after 1000 CV cycles	–	[60]
Zn _{SA} –N–C	5.64 wt%	0.1 M KOH	0.873	≈4	<5.0%	–	–	Zn–N ₄	No loss after 1000 CV cycles	0.179	[60]
((Fe,Co)/N–C	Fe:0.93 wt% + Co: 1.17wt%	0.1 M HClO ₄	0.863	≈4	<1.17%	66	2.842 @0.9V	FeCo–N	No loss after 50 000 CV cycles	0.98	[61b]
((Fe,Co)/CNTs	Fe:1.21 wt% + Co: 1.13wt%	0.1 M KOH	0.954	≈4	<12%	–	17.51 @0.9V	FeCo–N	Minimal loss after 10 000 CV cycles	0.26	[61a]
((Co,Zn)/N–C	Zn:0.33 wt% + Co: 0.14wt%	0.1 M KOH	0.861	3.88	5.0%	67	–	ZnCo–N ₆	9 mV loss after 10 000 CV cycles	0.705	[62]

induced an apparent half-wave potential loss, which manifests that Fe SAs are the active sites for the excellent ORR. DFT calculations based on Fe_{SA}–N–C and Fe_{NP}–N–C model well explained that the outstanding ORR activity of Fe_{SA}–N–C originates from the lower energy change (0.55 eV) that required in the most sluggish step for the ORR.

Although extensive studies focus on exploring Fe-based SACs with a high density of active sites, improving the utilization of inaccessible Fe–N_x–C as real active sites has been neglected for a long time, which is one of the main barriers for Fe-SACs application in practical energy conversion devices. To further enhance the ORR performance of Fe-SACs in both

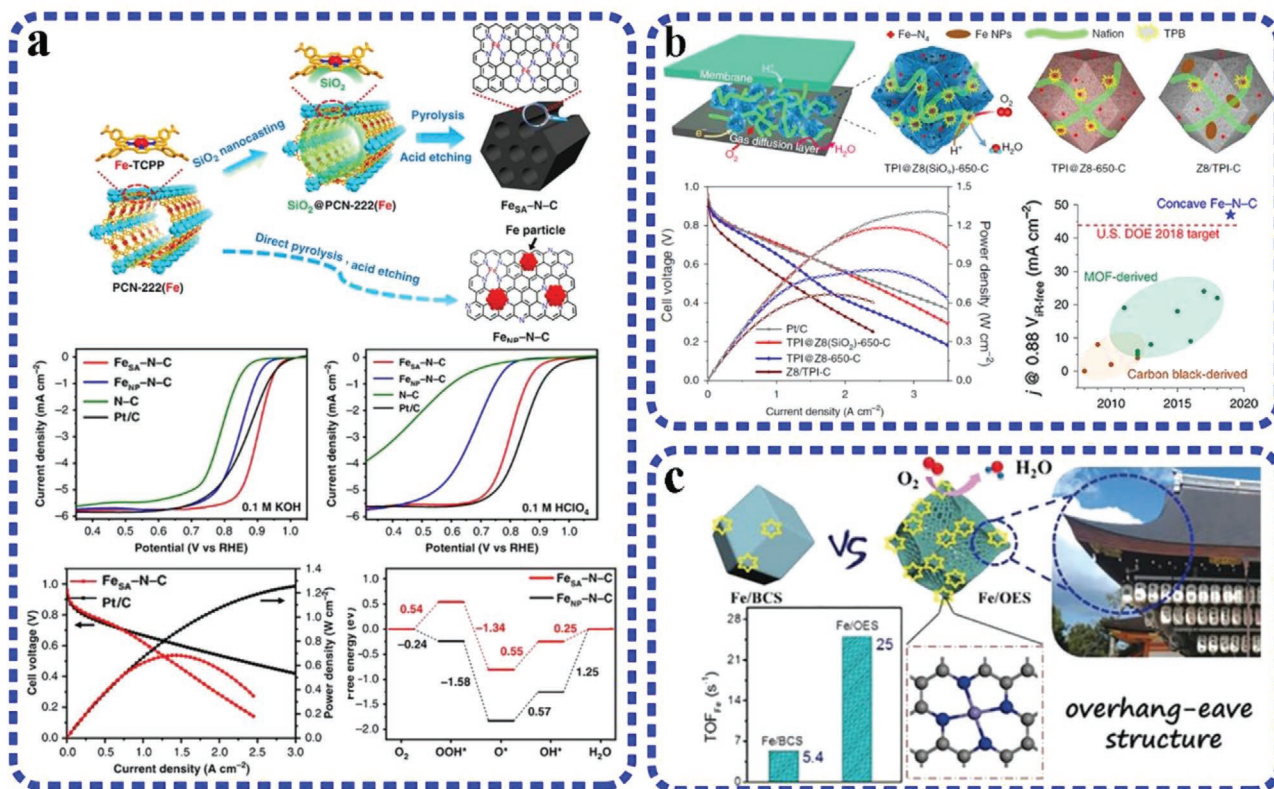


Figure 16. a) Schematic illustration of nanocasting-assisted synthesis of $\text{Fe}_{\text{SA}}\text{-N-C}$ from PCN-222(Fe); electrochemical ORR performance for $\text{Fe}_{\text{SA}}\text{-N-C}$ and reference catalysts in 0.1 M KOH and 0.1 M HClO₄; polarization and power density curves of PEMFCs with $\text{Fe}_{\text{SA}}\text{-N-C}$ and Pt/C cathode catalysts; free energy diagrams of ORR on $\text{Fe}_{\text{SA}}\text{-N-C}$ and $\text{Fe}_{\text{NP}}\text{-N-C}$ in acidic media. Reproduced with permission.^[28b] Copyright 2020, Nature Publishing Group. b) Schematic illustration of synthesis concave-shaped Fe-N-C SAC. $\text{H}_2\text{-O}_2$ fuel cell performance measurements and the resulting activity of Fe-N-C SAC compared with DOE target. Reproduced with permission.^[54c] Copyright 2019, Nature Publishing Group. c) Schematic illustration of synthesis MOF-derived Fe-SAs on overhang-eave carbon cages for high performance ORR. Reproduced with permission.^[56] Copyright 2020, Wiley-VCH.

half-cell and the full-fuel cell application, Xu and Shui studied the structure-performance relationships in consideration of Fe-N_x active sites density, accessible Fe-N_x utilization, and the catalyst layer porosity.^[54c] The concave-shaped $\text{Fe-N}_x\text{-C}$ SAC with dense Fe-N_4 moieties, mesoporosity and increased surface area was synthesized through a MOF strategy. Benefiting from the high density and sufficient exposure of active sites, the $\text{Fe}_{\text{SA}}\text{-N-C}$ SAC demonstrated an extremely high catalytic activity in both half-cell and full-cell of PEMFC devices. The half-cell test displayed that concave $\text{Fe}_{\text{SA}}\text{-N-C}$ SAC exhibited high activity, a four-electron pathway, long-time stability during the ORR, and excellent methanol tolerance. More importantly, through evaluating the ORR performance of $\text{Fe}_{\text{SA}}\text{-N-C}$ catalyst in a practical PEMFC, it was discovered that the PEMFC composed of $\text{Fe}_{\text{SA}}\text{-N-C}$ cathode exhibited a much high power density of 1.18 W cm^{-2} under 2.5 bar $\text{H}_2\text{-O}_2$ and high current density of 129 mA cm^{-2} at 0.8 V under 1.0 bar $\text{H}_2\text{-air}$ (Figure 16b). After executing the DOE testing protocol, the $\text{Fe}_{\text{SA}}\text{-N-C}$ cathode PEMFC demonstrated a current density of 0.047 A cm^{-2} @0.88 V (iR-free), outperformed the DOE 2018 target of 0.044 A cm^{-2} (@0.88 V iR-free). The quantitative study of structure-property relationship clearly evidenced that a high density of exposed Fe-N_4 active site is the key factor in achieving the high activity of $\text{Fe}_{\text{SA}}\text{-N-C}$ SAC, which make great

contributions in maximal active site utilization and rapid mass transport during PEMFC operation.

Engineering morphologies of SACs to facilitate mass transport in catalyst layers, can increase the utilization of active sites and thus enhance the ORR performance. Construct structures of SACs with more three-phase interface is considered benefit in promoting fast kinetics during the ORR. Xu and co-workers developed an overhang-eave structure decorated with single-atom Fe sites ($\text{Fe}_{\text{SA}}/\text{OES}$) via a silica-mediated MOF approach.^[56] The overhang-eave structure could supply more stretched edges as three-phase interface to support the mass transport for ORR and expose the active Fe sites to the utmost (Figure 16c). Benefit from these features, the $\text{Fe}_{\text{SA}}/\text{OES}$ catalyst demonstrated outstanding ORR catalytic activity under both alkaline and acidic media. Moreover, it exhibited remarkable ORR performance in Zn-air battery by achieving ultrahigh power density of 186.8 mW cm^{-2} and high capacity of $8075 \text{ mAh g}_{\text{Zn}}^{-1}$. It was claimed that the excellent activity originates from its over-hang eave and edge-rich morphology, which promote the mass transport of reactants to the exposed active sites of $\text{Fe-N}_4\text{-C}$.

Mn-Based SACs: Despite the encouraging ORR activity of Fe-N-C and Co-N-C SACs, they still suffer from the challenge of insufficient durability, especially in harsh acidic media

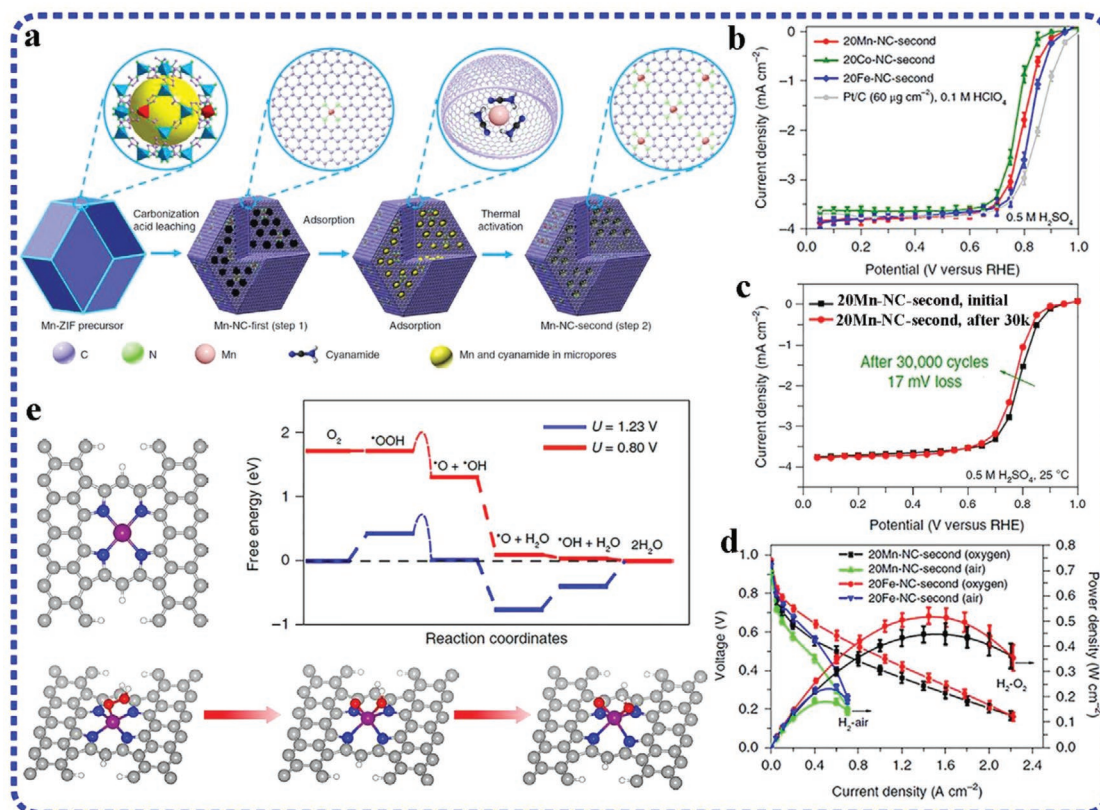


Figure 17. a) Schematic of atomically dispersed MnN_4 site catalyst synthesis. b) ORR activity and c) stability of MnN_4 site catalyst studied by using RRDE and d) fuel cell tests. e) Fundamental understanding of Mn active sites by using DFT calculations. Reproduced with permission.^[57] Copyright 2018, Nature Publishing Group.

and more practical voltage conditions, which hamper their long-term operation in energy conversion devices. The instability issue is partially caused by H_2O_2 oxidative Fenton attack during the ORR, which induces instability and dissolution of active metal centers. DFT calculations predict that Mn-based SACs with $\text{Mn-N}_4\text{-C}$ centers possess comparable electrocatalytic activity to that of $\text{Fe-N}_4\text{-C}$ moieties. Unlike Fe and Co, Fenton reactions ($\text{Fe}^{2+} + \text{H}_2\text{O}_2$) in Mn ions are insignificant because of the weak reactivity between Mn and H_2O_2 . To obtain the Mn-SAC and investigate its ORR performance, Wu and co-workers prepared the atomically dispersed $\text{Mn}_{\text{SA}}\text{-N-C}$ catalyst via two-step doping and adsorption synthesis by using the ZIF-8 precursors.^[57] For ORR in 0.1 M HClO_4 as shown in **Figure 17**, the $\text{Mn}_{\text{SA}}\text{-N-C}$ catalyst (Mn loading of 3.03 wt%) composed of atomically dispersed MnN_4 active sites exhibited half-wave potential of 0.80 V (vs RHE), which was comparable to that of $\text{Fe}_{\text{SA}}\text{-N-C}$ and $\text{Co}_{\text{SA}}\text{-N-C}$ SACs. The H_2O_2 yield was less than 2.0% indicating a highly efficient four-electron ORR pathway. The $\text{Mn}_{\text{SA}}\text{-N-C}$ catalyst was further employed as cathode catalyst for PEMFC application. A high open circuit voltage of 0.95 V was achieved in the $\text{H}_2\text{-O}_2$ PEMFC, suggesting a high intrinsic ORR activity of $\text{Mn}_{\text{SA}}\text{-N-C}$ catalyst. The $\text{Mn}_{\text{SA}}\text{-N-C}$ -based PEMFC output a maximum power density of 0.46 W cm^{-2} and generated the current density of 0.35 A cm^{-2} at 0.6 V, which exceeded the reported performance of Fe-N-C catalysts and the performance comparison of MOF-derived SACs

are summarized in Table 1. DFT calculations in **Figure 17e** confirmed that the $\text{MnN}_4\text{C}_{12}$ sites showed favorable binding with O_2 during the ORR, which contributed to break O–O bonds and promote the 4e[−] oxygen reduction in acidic media. Additionally, the long-term stability is another important evaluation criterion for SACs. By conducting durability testing at constant 0.7 V for 100 h, the $\text{Mn}_{\text{SA}}\text{-N-C}$ catalyst maintained 88% of its initial current density and exhibited only 29 mV loss of $E_{1/2}$ after 100 h test in half-cell. Even under real PEMFC operation, the $\text{Mn}_{\text{SA}}\text{-N-C}$ catalyst also presented superior durability compared to Co- and Fe-based SACs.

Cu-Based SACs: Common approaches for synthesis of SACs often require multiple procedures and lack appropriate interactions between the metal atoms and support. In 2018, Wu and Li reported a simple and practical strategy to access the large-scale synthesis of Cu-based $\text{Cu}_{\text{SAs}}\text{/N-C}$ SACs (Cu of 0.54 wt%) via thermally emitting Cu atoms from bulk copper.^[33a] According to electrochemical activity, the $\text{Cu}_{\text{SAs}}\text{/N-C}$ exhibited better ORR activity than Pt/C catalysts in 1.0 M KOH. For example, the $E_{1/2}$ of $\text{Cu}_{\text{SAs}}\text{/N-C}$ was 0.895 V (vs RHE) more positive than that of Pt/C (0.87 V) and $\text{Cu}_{\text{NPs}}\text{/N-C}$ (0.77 V). The nearly parallel Koutecky–Levich plots and RRDE results showed a four-electron pathway and high H_2O selectivity of $\text{Cu}_{\text{SAs}}\text{/N-C}$ for the ORR. The advanced kinetic current density and a lower Tafel slope of 63 mV dec^{-1} further confirmed the excellent activity of $\text{Cu}_{\text{SAs}}\text{/N-C}$ catalyst. Afterward, they developed

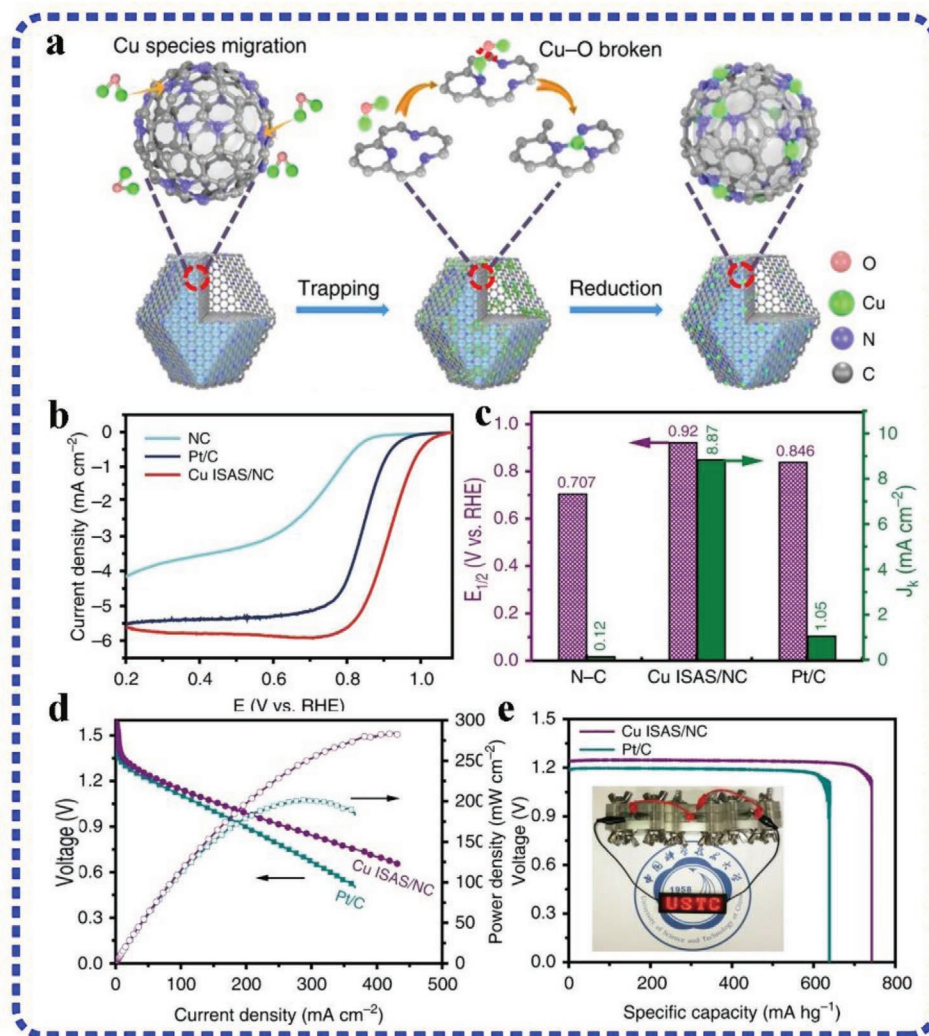


Figure 18. a) Schematic for the preparation of Cu-SAs/N-C. b) ORR activity, c) $E_{1/2}$ and J_k for Cu-SAs/N-C in 0.1 M KOH. d) polarization and power density plots of Cu-SAs/N-C and Pt/C Zn-air batteries. e) The specific capacity of Cu-SAs/N-C and Pt/C-based Zn-air batteries at 50 mA cm⁻². Reproduced with permission.^[58] Copyright 2019, Nature Publishing Group.

a high-temperature gas-transport strategy to direct construction isolated Cu-SACs (Cu_{1SA}/NC) from cost-effective and commercially available Cu₂O (Figure 18a).^[58] As displayed in Figure 18b,c, the Cu_{1SA}/NC catalyst provide the high ORR activity in 0.1 M KOH with positive half-wave potential of 0.92 V (vs RHE), large kinetic current density of 8.87 mA cm⁻², and small Tafel slope of 59 mV dec⁻¹. Employed as the cathode catalyst in Zn-air battery (Figure 18d-e), it was found that the maximum power density and specific capacity can be achieved up to 280 mW cm⁻² and ≈736 mAh g⁻¹ of Cu_{1SA}/NC-based Zn-air battery, better than that of Pt/C-based Zn-air battery. Based on the EXAFS and DFT analysis, the Cu-N₃-V structure was determined as the active site of the Cu_{1SA}/NC ORR catalyst. The synergistic effect of the defect (V) and the N coordination around Cu SAs contributes to the enhanced ORR activity of Cu_{1SA}/NC.

Zn-Based SACs: Zn has a fully filled d orbital, which makes it difficult to be oxidized in the presence of H₂O₂, thus Zn-based SACs are expected to be harmless to the electrode and

electrolyte membrane in PEMFC device.^[59] Unfortunately, the big challenge of Zn_{nSAs}-N-C catalysts is their poor performance in ORR compared with Fe_{nSA}-N-C catalysts. Due to the easy removal of Zn atoms during the high-temperature pyrolysis, fabrication of atomically dispersed Zn_{nSAs}-N-C catalyst while maintaining the high density of Zn atoms has proved difficult. After many research efforts, Wei and co-workers successfully fabricated the high loading of Zn SAs (9.33 wt%) dispersed in N-doped carbon by accurately controlling the gasification rate of Zn precursor.^[60] The ORR activity of optimized Zn_{nSA}-N-C catalyst in acidic medium reached a half-wave potential of 0.746 V (vs RHE), which was comparable to that of the Fe-N-C (0.743 V) catalyst. The H₂O₂ yield of Zn_{nSA}-N-C catalyst in both acidic and alkaline solutions was less than 5%, indicating a four-electron ORR pathway. It was demonstrated that the supported Zn SAs coordinated with N-doping sites and formed a planar Zn-N₄ structure, which are the major active centers in catalyzing the ORR and result in the enhanced ORR

activity. More interestingly, the Fenton reaction is substantially restrained and thus the Zn_{SA}-N-C catalyst exhibited superb electrochemical stability. DFT calculations further revealed that the Zn-N₄ centers are more electrochemically stable than the Fe-N₄ structure during the ORR process.

4.1.3. Bimetallic Dimer Catalysts

Instead of optimizing the active site density and engineering porosity structure, exploring new metal components and bimetallic active sites may be another way to achieve superior catalytic activity of SACs. Recently, fabrication of bimetallic atoms to make dual-metal dimer catalysts, such as Fe-Co^[61] and Co-Zn^[62] dimer, have been reported with excellent intrinsic electrocatalytic activity toward the ORR due to the synergistic effect arising from bimetallic atoms. In 2017, Li and co-workers reported the design of porphyrin-like Fe-Co dual-atom sites embedded in the hollow carbon matrix ((Fe,Co)/N-C).^[61b] By analyzing the electrochemical activity in O₂-saturated 0.1 M HClO₄, the (Fe,Co)/N-C dimer catalyst exhibited high ORR activity with $E_{1/2}$ of 0.863 V (vs RHE) and E_{onset} of 1.06 V (vs RHE). The kinetic current density at 0.9 V was 2.842 mA cm⁻², which surpassed most of the nonprecious metal catalysts (Figure 19a and Table 1). Same with the behavior of Pt/C, (Fe,Co)/N-C dimer catalyst reduced the oxygen to H₂O through a four-electron pathway, showing an H₂O₂ yield of 1.17% over the potential range from 0.2 to 0.8 V (vs RHE). Moreover, the (Fe,Co)/N-C as a cathodic catalyst was applied in a practical H₂/O₂ PEMFC. It was found that (Fe,Co)/N-C-PEMFC reached the maximum power density of ≈0.85 and 0.98 W cm⁻² at back pressures of 0.1 and 0.2 MPa, respectively, which outperformed most reported Pt-free catalysts (Table 1). DFT calculations showed that Fe-Co dual-atom sites can reduce the cleavage barrier in the activation of O-O bond, crucial in boosting high activity of the ORR. In their another work, a novel electrocatalyst with Fe-Co dual-atom sites embedded in N-doped carbon nanotubes (FeCo/CNTs) was constructed, which exhibited inimitable advantages toward the ORR.^[61a] The FeCo/CNTs dimer showed an admirable onset potential of 1.15 V (vs RHE) and half-wave potential of 0.954 V (vs RHE) in 0.1 M KOH, outperforming the performance indicated by commercial Pt/C (1.05 V and 0.842 V vs RHE). When employed at the air cathode in a Zn-air battery with 6.0 M KOH electrolyte, the FeCo/CNTs air cathode outputted high voltages of 1.31 and 1.23 V at discharge current densities of 20 and 50 mA cm⁻², respectively. The power density and specific energy density reached 260 mW cm⁻² and 870 Wh kg_{Zn}⁻¹, which were much better than that of the commercial Pt/C catalyst (18 mA cm⁻² and 105 mW cm⁻²).

Besides Fe and Co porphyrin, Zn porphyrin structure is found in carbonic anhydrase with a four-coordinated structure. The lower electronegativity (1.65) compared to Fe (1.83) and Co (1.88), lets Zn more easily to donate its outer electron to neighbor elements. When atom pairs form between Zn and the adjacent metal atom, a synergistic interaction enables the diatomic centers to approach enhanced catalytic activity. Zhao and co-workers reported the fabrication of Zn/Co bimetallic active sites supported on N-doped carbon.^[62] Such architecture offers enhanced binding ability with O₂, significantly elongates the O-O length,

and thus facilitates the cleavage of O-O bond during the ORR. Importantly, the Zn/Co-N-C catalyst exhibited outstanding ORR performance in both alkaline and acid conditions via a four-electron pathway with $E_{1/2}$ of 0.861 and 0.796 V (vs RHE), respectively (Figure 19b). The assembled Zn-air battery and fuel cell with Zn/Co-N-C as cathode catalyst showed excellent power density and stability, which demonstrate promising practical application of the bimetallic Zn/Co-N-C dimer catalyst.

Through summary the recent progress of SACs, it can be concluded that dispersed SAs located on porous carbon support derived from MOF strategy have shown fascinating activity for the ORR, due to their unique characteristics of maximum atom utilization, unique electronic structure, and unsaturated coordination environment. However, to be an alternative electrocatalyst with high intrinsic activity, an ideal SAC comprised of O₂-favorable reactive sites for cleaving the O=O double bond, optimized geometric structure for O₂ diffusion and water management is in high demand. It is necessary to understand the original ORR mechanism catalyzed by the single-atom active sites. In future, the dimer catalyst with bimetallic or monometallic dimer catalyst, and even triatomic catalyst need to be developed and investigated for the ORR. Another challenge is the practical application of SACs in batteries or fuel cells. The industrial process is much different from the lab-synthesis. If the lab protocol can be expanded and used in large scale synthesis of SACs, it will approach huge achievements and progress in the field of SAC.

4.2. MOF-Derived SACs for CO₂ Reduction Reaction

Electrochemical conversion of CO₂ into value-added products such as methanol, ethanol, methane, and formic acid is an effective approach to remit global warming and energy issues.^[46b,63] However, achieving the electroreduction of CO₂ usually requires overcoming some bottlenecks, such as the large overpotential necessary for CO₂ activation and electron transfer, and suppress multi products derived from competitive side reactions.^[64] As a result, finding active and selective catalysts is of paramount importance to make practical CO₂ electroreduction a reality. Benefiting from the high ratio of low-coordinated metal atoms and technically uniform structure, SACs have shown great potential as ideal catalysts in the electrochemical CO₂ reduction.^[7b,65] Particularly, SACs achieved from MOF strategy are reported to be capable in CO₂ reduction reaction (CO₂RR) with high activity and selectivity.^[64a,66] In this section, we will summarize the recent progress that has been made on the MOF-derived active or selective SACs, and their reaction mechanism in the CO₂RR.

4.2.1. Electrochemical Reduction of CO₂ to CO

The electroreduction of CO₂ to carbon monoxide (CO) is a two-electron pathway that consists of two elementary steps. CO₂ is first reductively adsorbed on the catalyst surface to form *COOH intermediate. Then the adsorbed *COOH is further reduced to *CO via electron-proton transfer and desorbed from electrode and releasing the CO. Based on the reaction pathway,

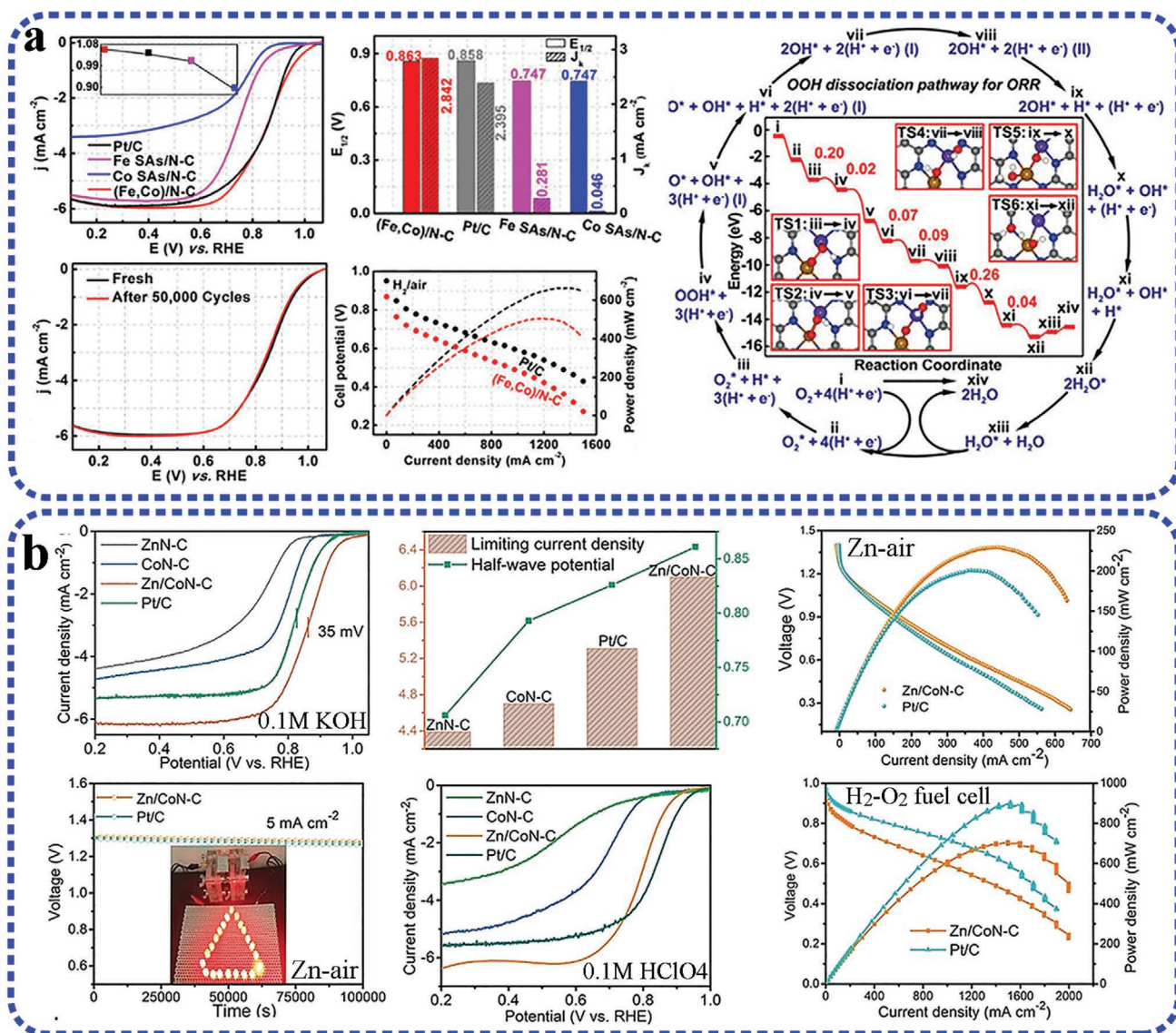


Figure 19. a) RDE polarization curves of ORR activity, electron transfer number, durability and the H₂/O₂ fuel cell performance of (Fe,Co)/N-C catalysts. Energy of intermediates and transition states in mechanism of ORR at (Fe,Co)/N-C from DFT. Reproduced with permission.^[61b] Copyright 2017, American Chemical Society. b) ORR polarization curves for different catalysts in O₂-saturated 0.1 M KOH, limiting current density and half-wave potential of Zn/Co-N-C catalysts. Polarization and power density curves of Zn-air battery using Zn/Co-N-C catalyst. ORR curves for different catalysts in 0.1 M HClO₄ and H₂/O₂ fuel cell polarization plots. Reproduced with permission.^[62] Copyright 2019, Wiley-VCH.

an ideal SAC should have appropriate adsorption energy for the key intermediates. Herein, recent advances in MOF-derived SACs for selective CO evolution from CO₂ RR are described.

Ni-Based SACs: Li and Wu developed an ion exchange MOF strategy to generate Ni SACs (Ni_{SAs}/N-C) for selectively catalyzing the CO₂RR.^[24] The comparison of CO₂ reduction activities of Ni_{SAs}/N-C and Ni_{NPs}/N-C was summarized in **Figure 20a**. The current density reached to 10.48 mA cm⁻² at -1.0 V (vs RHE) of Ni_{SAs}/N-C catalyst during the CO₂RR, which was roughly 3 times larger than that of Ni_{NPs}/N-C. At -0.9 V (vs RHE), Ni_{SAs}/N-C catalyst exhibited high Faradaic efficiency for CO production of 71.9%. Nyquist plots revealed that Ni_{SAs}/N-C had a lower interfacial charge-transfer resistance

than Ni NPs/N-C, thereby ensuring fast electron transfer from the electrode to CO₂ and easy formation of *COO⁻ radical anions. Since Ni_{SAs}/N-C showed rich low-coordinated active sites on the surface, the strong bonding energy of CO₂*⁻ to Ni SAs account for the excellent activity. However, Ni SAs also exhibited a competitive activity for the HER, which depress the high Faradaic efficiency for CO production.

An efficient CO₂RR catalyst should enhance CO₂RR activity and selectivity while suppress the competitive HER. Bao and Wang proposed a strategy to synthesize Ni-Nx active sites within porous carbon achieving Ni SAs loading of 5.44 wt% (Zn/Ni-N-C).^[67] In the CO₂-saturated 1.0 M KHCO₃, the Zn/Ni-N-C catalysts exhibited high CO Faradaic efficiency

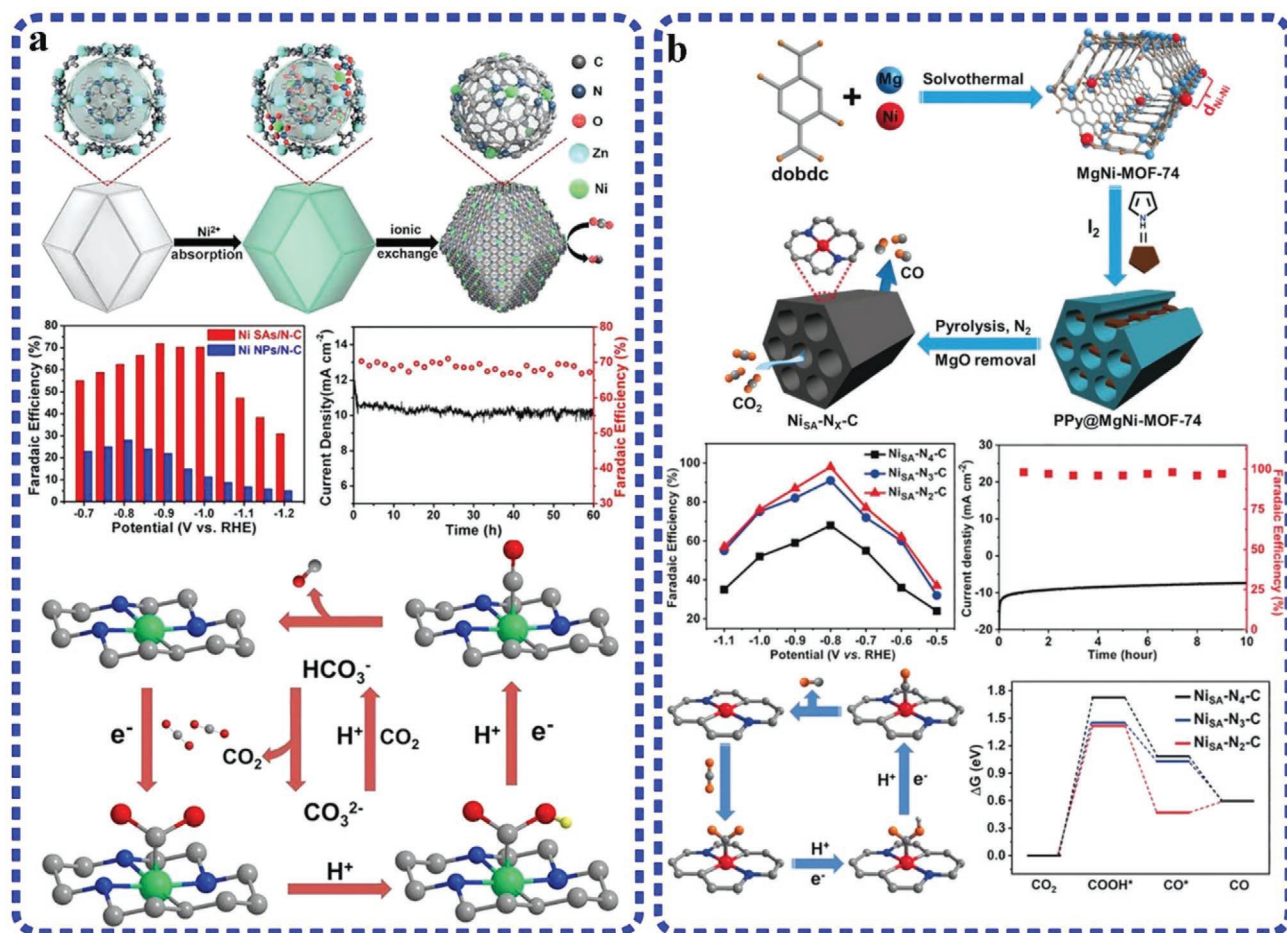


Figure 20. a) Scheme for the synthesis of NiSAs/N-C. LSV curves, Faradaic efficiency of CO, TOFs, and stability of Ni SAs/N-C and Ni NPs/N-C catalyst. Proposed reaction paths for CO₂ electroreduction by NiSAs/N-C. Reproduced with permission.^[24] Copyright 2017, American Chemical Society. b) Schematic illustration for the synthesis of Ni_{SA}-N_x-C. The electrocatalytic performance of CO₂RR for CO Faradaic efficiency and stability of Ni_{SA}-N_x-C at -0.8 V, proposed reaction path for CO₂RR with Ni_{SA}-N_x-C. Reproduced with permission.^[66b] Copyright 2020, Wiley-VCH.

of 92.0–98.0% (Table 2) over a wide potential range of -0.53 to -1.03 V (vs RHE). The effect of Ni and Zn loading in Zn/Ni-N-C catalyst was investigated. The electrochemical performance demonstrated that the CO current density increased with Ni loading, while higher Zn loading resulted in a low CO current density, suggesting Ni-N sites were the active centers for CO₂RR and the blocking effect of Zn species. DFT calculations were conducted to understand the catalytic selectivity between the CO₂RR and HER over Ni-N_x and Zn-N_x sites. The electroreduction of CO₂ into CO is considered with three elementary steps of the initial state (CO₂ molecule), adsorbed intermediate states (*COOH, *CO) and the terminal state (CO molecule). The conversion of CO₂ to adsorbed COOH* is the rate-determining step, which shows a close relationship to the CO₂RR activity. The low free energy of *COOH on NiN₂V₂ active centers suggests the high activity for the CO₂RR. In contrast, *H is quite preferred to adsorb on NiN₃V, which leads to predominantly competitive HER process. Therefore, it is pointed that the active sites of NiN₂V₂ with Ni-N coordination number of 2, which endow Zn/Ni-N-C catalyst with high activity and selectivity for the CO₂RR.

It is acknowledged that local coordination environment usually plays a significant role for the catalytic activity and selectivity of SACs. The accurate control of the coordination environment of SACs at an atomic level remains a great challenge. Jiang and co-workers developed a host-guest cooperative MOF strategy to construct the Ni SAs implanted N-doped carbon catalysts (Ni_{SA}-N_x-C) with controlled Ni-N coordination number from 4 to 2.^[66b] Significantly, the Ni_{SA}-N₂-C catalyst with the lowest N coordination number, possesses a high current density, maximum CO Faradaic efficiency (98%) and turnover frequency (1622 h⁻¹), which are far superior than all the measured SACs in CO₂RR following a trend of Ni_{SA}-N₂-C > Ni_{SA}-N₃-C > Ni_{SA}-N₄-C (Figure 20b). Theoretical calculations unveil that the reduced coordination of Ni_{SA} with N atoms in Ni_{SA}-N₂-C favors the formation of COOH* intermediate during the reaction path of CO₂ to CO and thus improves the superior activity in electrocatalytic CO₂RR.

Co-Based SACs: The molecular optimization of MOF by using Co-porphyrin as building units can be used to prepare Co-SACs for electrochemical reduction of CO₂ to CO. Koper and co-workers immobilized Co-porphyrin molecular catalyst onto

Table 2. Summarize of MOF-derived SACs for the CO₂ RR.

Catalyst	Metal SAs loading	Electrolyte	Maximum Faradaic efficiency [%]	CO ₂ RR products	CO ₂ RR current density [mA cm ⁻²]	TOF [h ⁻¹]	Durability	Active centers	Ref.
Ni _{SA} /N-C	1.53 wt%	CO ₂ -saturated 0.5 M KHCO ₃	71.9	CO	7.37 @ -1.0 V (vs RHE)	5273	Stable during 60 h CO ₂ RR	Ni-N	[24]
Ni _{SA} -Nx-C	0.9 wt%	CO ₂ -saturated 0.5 M KHCO ₃	98	CO	≈12.0 @ -0.8 V (vs RHE)	3467	Stable during 10 h CO ₂ RR	Ni _{SA} -N ₂ -C	[66b]
Zn/Ni _{SA} -N-C	5.44 wt%	CO ₂ -saturated 1.0 M KHCO ₃	98	CO	71.5 ± 2.9 @ -1.03 V (vs RHE)	10 087 ± 216	3.2% loss of FE for 2 h CO ₂ RR	NiN ₂ V ₂	[67]
Co _{SA} -NC	0.25 wt%	CO ₂ -saturated 0.5 M KHCO ₃	94	CO	32.7 @ -0.78 V (vs RHE)	33 000	Stable during 60 h CO ₂ RR	Co-N ₂	[21b]
Co-N ₅ /HNPCs	3.54 wt%	CO ₂ -saturated 0.5 M KHCO ₃	99.4	CO	4.5 @ -0.73 V (vs RHE)	480.2	Stable during 10 h CO ₂ RR	Co-N ₅	[68]
Fe-NG	1.25 wt%	CO ₂ -saturated 0.1 M KHCO ₃	80	CO	≈2.7 @ -0.8 V (vs RHE)	-	Stable during 10 h CO ₂ RR	Fe-N ₄	[65c]
Fe _{SA} -N-C	0.1 at%	CO ₂ -saturated 0.5 M KHCO ₃	93	CO	6.0 @ -0.7 V (vs RHE)	-	Stable during 20 h CO ₂ RR	Fe-N ₂₊₂ -C ₈	[70]
Fe _{SA} /CNF-900	4.58 wt%	CO ₂ -saturated 0.5 M KHCO ₃	86.9	CO	2.8 @ -0.47 V (vs RHE)	639.9	Stable during 12 h CO ₂ RR	Fe-N _x	[69c]
(Ni/Fe)-N-C	Ni:0.97 wt% Fe:0.34 wt%	CO ₂ -saturated 0.5 M KHCO ₃	98	CO	7.4 @ -0.7 V (vs RHE)	7682	1% loss after 30 h CO ₂ RR	Ni/Fe-N	[71]
Cu _{SA} /TCNFs	1.3 wt%	CO ₂ -saturated 0.5 M KHCO ₃	44 for CH ₃ OH 56 for CO	CH ₃ OH & CO	93 for CH ₃ OH @ -0.9 V (vs RHE)	-	Stable for 50h electrolysis	Cu-N ₄	[72b]

graphite electrode and monitored the volatile products distribution during CO₂RR in acidic electrolyte.^[63d] CO was identified as the major product together with other hydrocarbons. It was reported that the atomic Co-N₄ sites exhibit high Faradaic efficiency (90%) at an overpotential of 0.55 V. In another example, three atomically dispersed Co catalysts with different coordination numbers of Co-N₄, Co-N₃, and Co-N₂ were developed by Li and co-workers and their corresponding catalytic performance toward CO₂RR were studied.^[21b] The Co-SAC with Co-N₂ sites gained higher CO₂RR activity and selectivity than that of Co-N₄ sites. The current density of 18.1 mA cm⁻² and a CO Faradaic efficiency of 94% at a low overpotential of 0.52 V could be reached by the Co-N₂ catalyst. In their subsequent study, the Co-SAC with atomically dispersed Co-N₅ sites anchored on hollow N-doped porous carbon spheres (Co-N₅/HNPCs)^[68] exhibited CO Faradaic efficiency up to 99.2% and 99.4% at -0.73 and -0.79 V (vs RHE), which outperformed most reported SACs (Table 2). Moreover, the CO current density and Faradaic efficiency remained nearly unchanged after 10 h of electrocatalysis, indicating the remarkable stability. The Co-N₅ coordination configuration and DFT calculations both indicated that single-atom Co-N₅ sites are the dominating active centers simultaneously for CO₂ activation and reduction. According to comparison the CO₂RR performance of reported Co-SACs, it can be known that unsaturated coordination resulted in unoccupied 3d orbitals of Co atoms, which facilitate the adsorption of CO₂ and increase CO₂ reduction rate. In terms of the atomically dispersed Co-N_x sites in electrochemical CO₂RR to CO, the catalytic activities are ranked in the order of Co-N₅ > Co-N₂ >> Co-N₄, Co-N₃, Co-N₁.

Fe-Based SACs: Atomically dispersed Fe-N₄ sites in Fe-N₄-C catalysts derived from MOF were reported to exhibit high activity and selectivity in conversion of CO₂RR to CO.^[65c,69] Wu

and Li designed the nitrogen-coordinated and atomically dispersed Fe-N₄ and Co-N₄ catalysts as an ideal model system to study the active sites toward the CO₂RR (**Figure 21a**).^[70] Experimental results discovered that Fe-N₄ sites are more active than Co-N₄ sites toward the electrochemical conversion of CO₂ into CO. For the Fe-N₄-C, the highest CO Faradaic efficiency of 93% at an overpotential of 0.47 V can be achieved. Meanwhile, Fe-N₄-C is more effective in suppressing the HER compared with Co-N₄-C. Reaction thermodynamics and DFT calculations demonstrated that the configuration of Fe-N₂₊₂-C₈ sites are thermodynamically and kinetically active centers for the CO₂RR. In another example, the mesoporous carbon nano-frames implanted with atomically dispersed Fe-N_x active sites (FeSA/CNF) were prepared from Fe-MOF precursor by Zhu and co-workers.^[69c] It was found that the distinctive structure with dense Fe atoms and plentiful mesopores afford FeSA/CNF catalyst with extraordinary bifunctional electrocatalytic performance for ORR and CO₂RR. As illustrated in the Figure 21b, the FeSA/CNF-900 showed the highest values of the current density and with a maximum Faradaic efficiency up to 86.9% (at -0.47 V) for conversion of CO₂ to CO. Due to the high density of the Fe-N_x active sites, the FeSA/CNF-900 also presented the high turnover frequency of 639.9 h⁻¹ and excellent stability during the continuous CO₂ electrocatalysis for 12 h.

Bimetallic Dimer catalysts: Monometallic Ni-N, Co-N, and Fe-N sites are reported to exhibit high current density for CO production but suffer from sluggish kinetics of the first proton-coupled electron transfer (CO₂ + H⁺ + e⁻ → COOH*). Despite Fe-N and Co-N sites showing low onset potential for CO₂RR, the desorption of *CO lowers their reactivity due to the strong binding of CO to the single Fe- or Co-atom sites, which results in multiple intermediates and products, and decreases the product selectivity. To address this issue, building planar active

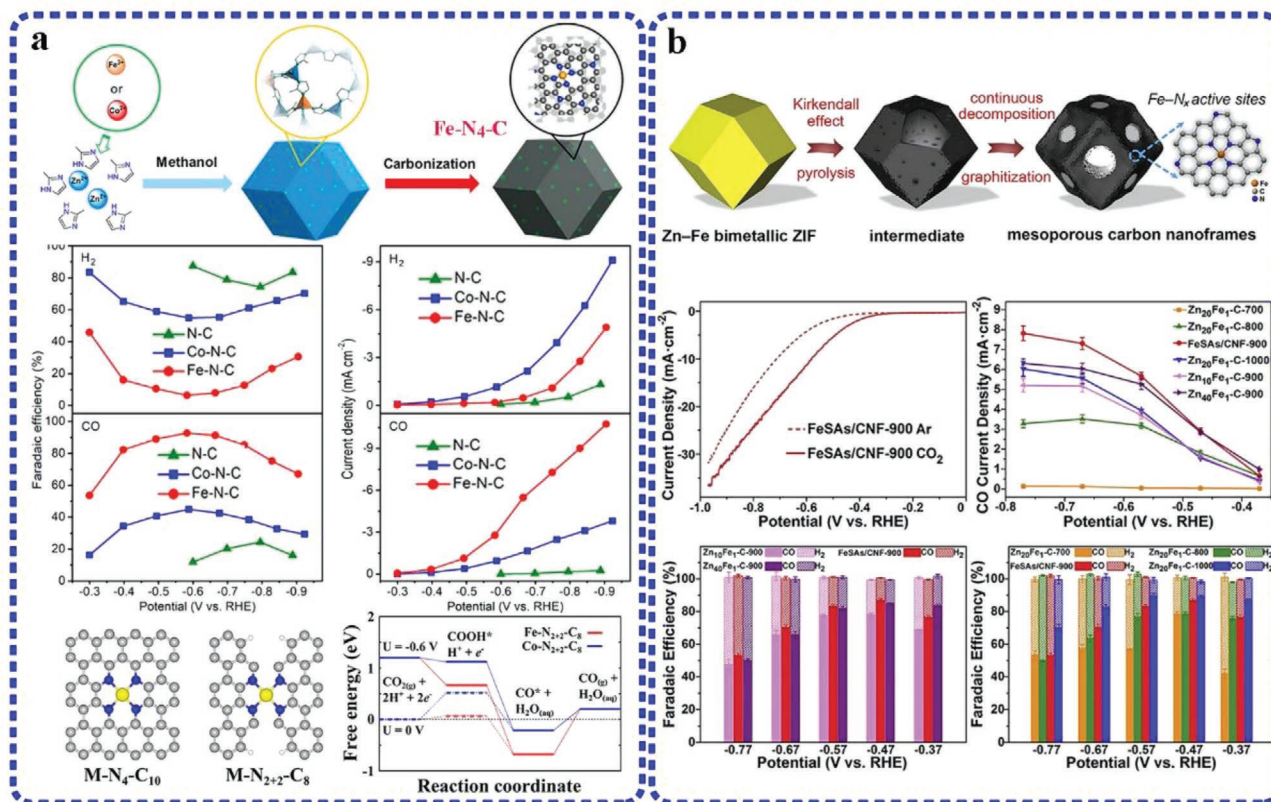


Figure 21. a) Schematic illustration for the synthesis of Fe-NC and Co-NC catalysts. CO and H₂ Faradaic efficiency, and current density of N-C, Co-N-C, and Fe-N-C in electrocatalytic CO₂RR. Atomic structure of M-N₄-C₁₀, M-N₂₊₂-C₈ active sites and the calculated free energy of CO₂ reduction to CO under electrode potential of (U) 0 and -0.6 V. Reproduced with permission.^[70] Copyright 2018, American Chemical Society. b) Schematic illustration of the formation of Fe_{5A5}-N_x and evaluation of CO₂RR catalytic performance for the catalysts. Reproduced with permission.^[69c] Copyright 2020, Elsevier Ltd.

centers with exposed atomic interface, and synergistic interaction are effective solutions. Zhao and co-workers demonstrated a bimetal-catalyst with isolated Ni-Fe dual atoms anchored in N-doped carbon (Ni/Fe-N-C).^[71] The electrocatalytic activity of Ni/Fe-N-C for the CO₂RR was studied using a three-electrode H-cell filled with CO₂-saturated 0.5 M KHCO₃ electrolyte. It was found that Ni/Fe-N-C showed a maximum CO Faradaic Efficiency of 98% and current density of 7.4 mA cm⁻² at -0.7 V (vs RHE), which is 1.5 and 4.6 times higher than that of Ni-N-C and Fe-N-C catalysts, respectively. Moreover, Ni/Fe-N-C demonstrated outstanding durability, maintaining 99% of initial Faradaic efficiency for CO production (≈8 mA cm⁻²) after 30 h of continuous electrolysis. The structurally sensitive XAFS and DFT calculations revealed that the bimetallic Ni/Fe-N dimer catalyst undergoes a structure change into CO-adsorbed moiety, which reduces the energy barrier during formation of the intermediate COOH* and desorption of *CO, thus accounting for the enhanced CO₂RR activity.

4.2.2. Electrochemical Conversion of CO₂ to Alcohol

The M-N_x-C-based SACs demonstrate impressive activity for CO₂RR in yielding the two-electron reduction products of CO. However, controlling the catalytic selectivity of CO₂RR

to generate high-value products such as hydrocarbons and alcohols still presents a great challenge.^[72] After significant efforts in the field of CO₂RR, the metallic Cu atom was found with the capability to convert CO₂ into alcohol products. For example, In 2019, He and co-workers proposed a facile strategy for the large-scale synthesis of Cu SAs dispersed in carbon nanofibers (CuSAs/TCNFs) as electrocatalyst for the CO₂RR (Figure 22a).^[72b] Benefiting from excellent mechanical properties, the CuSAs/TCNFs membrane can be used directly as a cathode for CO₂ RR, which generated nearly pure methanol and CO with 44% and 56% Faradaic efficiency in liquid- and gas-phase products at -0.9 V (vs RHE), respectively. Owing to the synergetic effect arising between the through-hole carbon and Cu SAs, CuSAs/TCNFs exhibited 93 mA cm⁻² partial current density for methanol and more than 50 h of stability in aqueous solution (Figure 22b,c). To explore the reaction mechanism of CO₂RR conversion to CH₃OH on Cu-based SACs, the authors completed DFT calculations from *CO conversion to methanol (Figure 22d-g). It was discovered that *CO intermediate can combine with a proton and form *COH, then *COH species were further reduced into *CHOH on Cu-N₄ structure with a moderate free energy barrier much lower than the steps in generating CH₄ production. Therefore, single-atom Cu-N₄ sites on CuSAs/TCNFs catalyst tend to generate CH₃OH instead of CH₄ through the pathway of

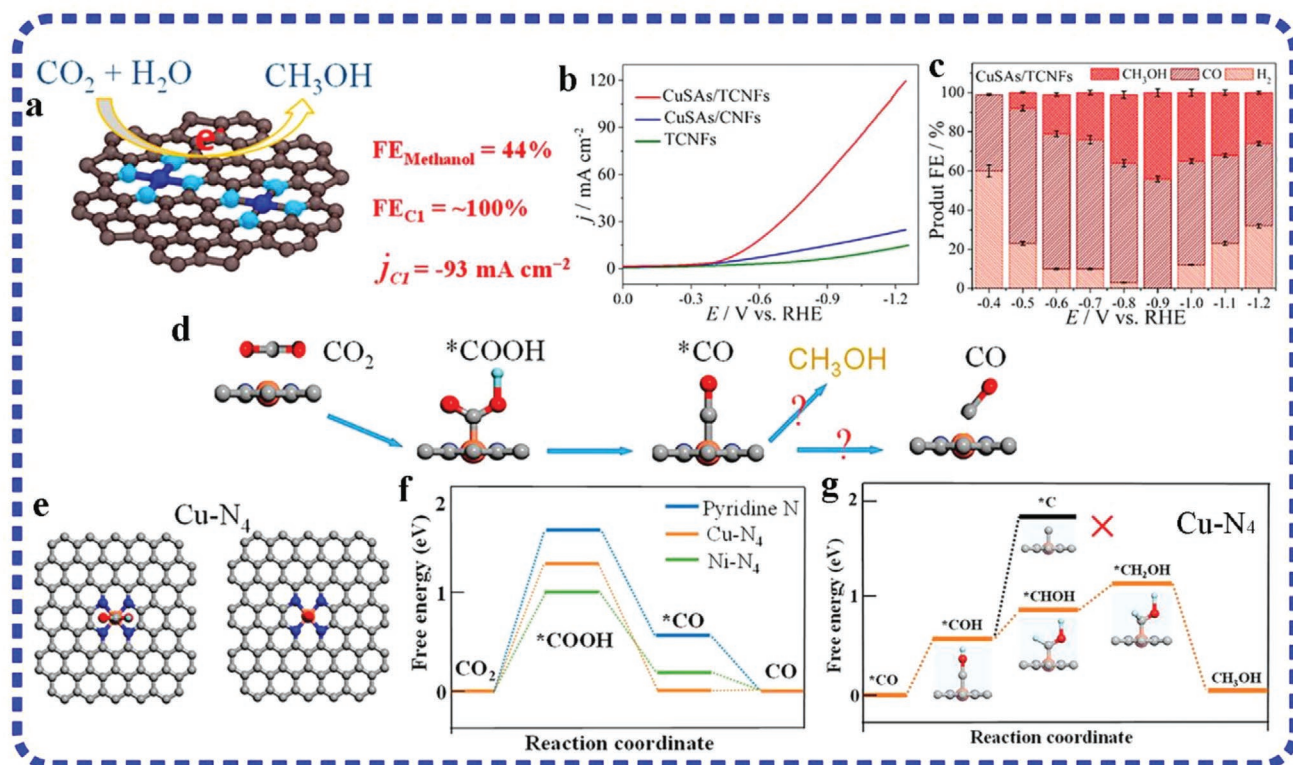
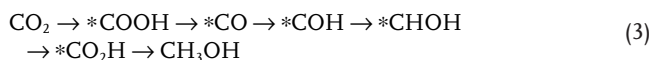


Figure 22. a) Schematic illustration of CO₂RR to CH₃OH on the catalyst of CuSAs/TCNFs. b) LSV curves recorded in CO₂-saturated 0.1 M KHCO₃ solution and c) Faradaic efficiencies of all products at CuSAs/TCNFs catalysts. d) Proposed reaction paths for CO₂ electroreduction. e) Optimized atomic structures of CuSAs/TCNFs. f) Free energy diagram of CO₂ to CO on pyridine N, Ni-N₄, and Cu-N₄ structure. g) Free energies for conversion of *CO to CH₃OH on Cu-N₄ structure. Reproduced with permission.^[72b] Copyright 2019, American Chemical Society.



The self-supporting CuSAs/TCNFs membrane is easy to synthesize on a large-scale and can be used directly as the cathode for catalyzing the CO₂RR, which shows great potential in practical application of CO₂RR.

According to recent progress, it can be known that a variety of SACs designed from MOF precursors show promising electrocatalytic performance in CO₂RR especially to C₁ products (CO and methanol) with high activity and selectivity. However, SACs for the CO₂RR is still in an early stage. The production of high-value C₂₊ products, high current density achievement, and practical device application still requires further investigation. To this end, tuning appropriate intermediate adsorption and conversion energy on bi-(or multi-) metallic atom catalysts may favor for generation of C₂₊ products (e.g., C₂H₄, C₂H₆, or C₂H₅OH). Alternatively, controlling the coordination environment and synergy interaction between metal atoms may facilitate C₂₊ products.

4.3. MOF-Derived SACs for N₂ Reduction Reaction

Nitrogen (N₂) reduction reaction via conversion of atmospheric N₂ into ammonia (NH₃) is one of the significant conversion

reactions in industry, because NH₃ not only plays important role in producing fertilizer but also serves as green energy carrier and alternative fuel.^[73] Nowadays, industrial ammonia is predominantly synthesized by the Haber–Bosch process using Fe-based catalysts at high pressure (150–200 atm) and high temperature (300–500 °C), which brings in huge energy consumption.^[74] Recently, electrochemical approaches using heterogeneous catalysts to achieve nitrogen reduction and fixation at room temperature have attracted increasing attention.^[75]

4.3.1. Principle and Reaction Mechanism of the NRR

The electrochemical N₂ reduction to NH₃ involves multiple proton–electron transfer steps and generates different intermediates. It is reported that the NRR occurs based on two fundamental mechanism of dissociative and associative pathways.^[73a,75b,c] For the dissociative mechanism (Figure 23b), adsorbed N₂ molecules firstly undergo cleavage of the inert N≡N triple bonds, then hydrogenation occurs and generates an intermediate of N–H which requires high energy input. Accordingly, the dissociative mechanism is less favorable for the NRR under ambient conditions. While for the associative pathway, the adsorbed N₂ molecule keeps two N atoms bonding with each other until final release of NH₃. Considering different sequence between N₂ adsorption and hydrogenation,

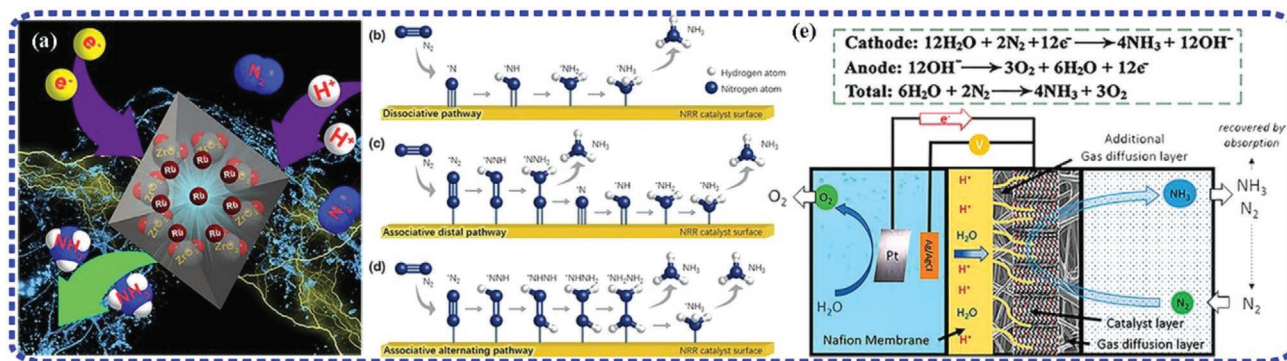


Figure 23. Schematic illustration of a) the N₂ reduction reaction (NRR) electrocatalysis and b–d) its possible mechanisms, including dissociative pathway, associative distal pathway, and associative alternating pathway, e) electrochemical of NRR in three-phase reaction. Reproduced with permission.^[75c] Copyright 2019, Elsevier Ltd.

the hydrogenation process in the associative mechanism can proceed via two ways, including the distal pathway (Figure 23c) and alternating pathway (Figure 23d). In the associative distal pathway, one N atom far away from the end-on adsorption site undergoes a hydrogenation process until releasing the remote NH₃ molecule. Subsequently, the remaining N atom repeats the same procedure to generate the second NH₃ molecule. In terms of associative alternating pathway, two N atoms are hydrogenated in turn accompany with proton-coupled electron transfer, and two NH₃ are released sequentially at the final step.

In the electrochemical cell for converting N₂ into NH₃, the most widely adopted reactor is the H-type cell, as shown in Figure 23e. The H₂O oxidation reaction occurs in the anode side, and the N₂ reduction into NH₃ happens in the cathode side. As the reaction process is suppressed by slow kinetics of N₂ adsorption and the sluggish splitting of strong N≡N bond, a large overpotential, low Faradaic efficiency and low NH₃ yield are the main challenges for the NRR.^[76] Developing highly active and stable electrocatalysts, which show advantages in achieving low overpotential, high NH₃ yield, and high Faradaic efficiency, is of great significance.^[77] Electrocatalysts with atomic-scale active sites have demonstrated outstanding activity in numbers of electrochemical reactions (e.g., ORR, CO₂RR, HER, and OER). The uniform low-coordination environment, much active sites, maximum metal atom utilization, and ultrafast charge transfer endowing SACs optimal binding strength with intermediates. Inspired from their unique features, SACs have been exploited in electrocatalysis of the NRR, with expectation of breaking up the highly stable N≡N covalent triple bond (941 kJ mol⁻¹).^[75c,78]

4.3.2. SACs for the NRR

The electrochemical system for NRR is complicated and contains numerous impact factors, such as electrocatalysts, electrolyte and electrochemical technique, potential, temperature, etc. Early DFT calculations conducted by Norskov and co-workers demonstrated that HER is a major competing reaction for NRR.^[76] At present, the electrochemical NRR at ambient conditions is hampered by the low Faradaic efficiency, high overpotential and low NH₃ yield.^[73a,75a,b] Therefore, developing advanced electrocatalysts to suppress the side reaction of HER

while boost the NRR activity and selectivity should be in primary consideration. Recently, Jung and co-workers conducted DFT calculations and revealed that Ti and V SAs anchored in defective graphene exhibit promising activity toward the NRR.^[78c] The ensemble effect of SACs with only top site adsorption is available for H adsorption compared to several adsorption sites (e.g., top, bridge and hollow adsorption) for the metal bulk and NPs surface, which can suppress the HER and enable SACs with high NRR activity and selectivity.^[75d,78a] In this section, we will highlight recent attempts toward MOF strategy in synthesis atomic-scale SACs for the NRR, with an emphasis on noble metal-based SACs and transition metal-based SACs derived from MOF.

Noble Metal SACs for the NRR: The capability of noble metal SACs for the electrochemical fixation of N₂ into NH₃ have been investigated.^[79] For the pioneering work, Li and Wu prepared Au atoms electrocatalyst for the NRR.^[79b] The Au₁/C₃N₄ SAC displayed great NRR catalytic activity with Faradaic efficiency of 11.1% at -0.10 V (vs RHE) and high NH₄⁺ yield rate of 1305 μg h⁻¹ mg_{Au}⁻¹, outperforming that of Au_{NPs}/C₃N₄ catalyst. The lower free energy barrier required in the rate determining step of conversion N₂ to *NHH for Au₁/C₃N₄ (ΔG = 1.33eV) than that of Au_{NPs}/C₃N₄ (ΔG = 2.01eV), well revealed the reaction pathway and explained the enhanced activity of Au₁/C₃N₄ SAC. According to the experimental and computational results, it was claimed that the electron depletion of Au atom could shift its d-orbital to the Fermi level, which optimizes its interaction with intermediates and thus leads to a better selectivity in electroreduction of N₂ to NH₃.

Besides Au SAs, Ru-based SACs attracted much attention and have been reported with distinguished performance in NRR. For example, Zeng and co-workers developed Ru SAs supported on N-doped carbon (Ru₁/N-C with Ru loading of 0.18 wt%) via pyrolysis of MOF precursor.^[79d] The electrochemical performance in Figure 24a showed that Ru₁/N-C exhibited high partial current density in yielding NH₃. Notably, 29.6% Faradaic efficiency and high current density of -0.13 mA cm⁻² are achieved for Ru₁/N-C at -0.2 V (vs RHE). When normalized to catalysts mass loading, the yielding rate of NH₃ over Ru₁/N-C reached 120.9 μg_{NH₃} h⁻¹ mg_{cat}⁻¹, much higher than that of Ru_{NPs}/N-C catalyst. DFT calculations indicated that low free energy barrier was required in N₂ dissociation and reduction on

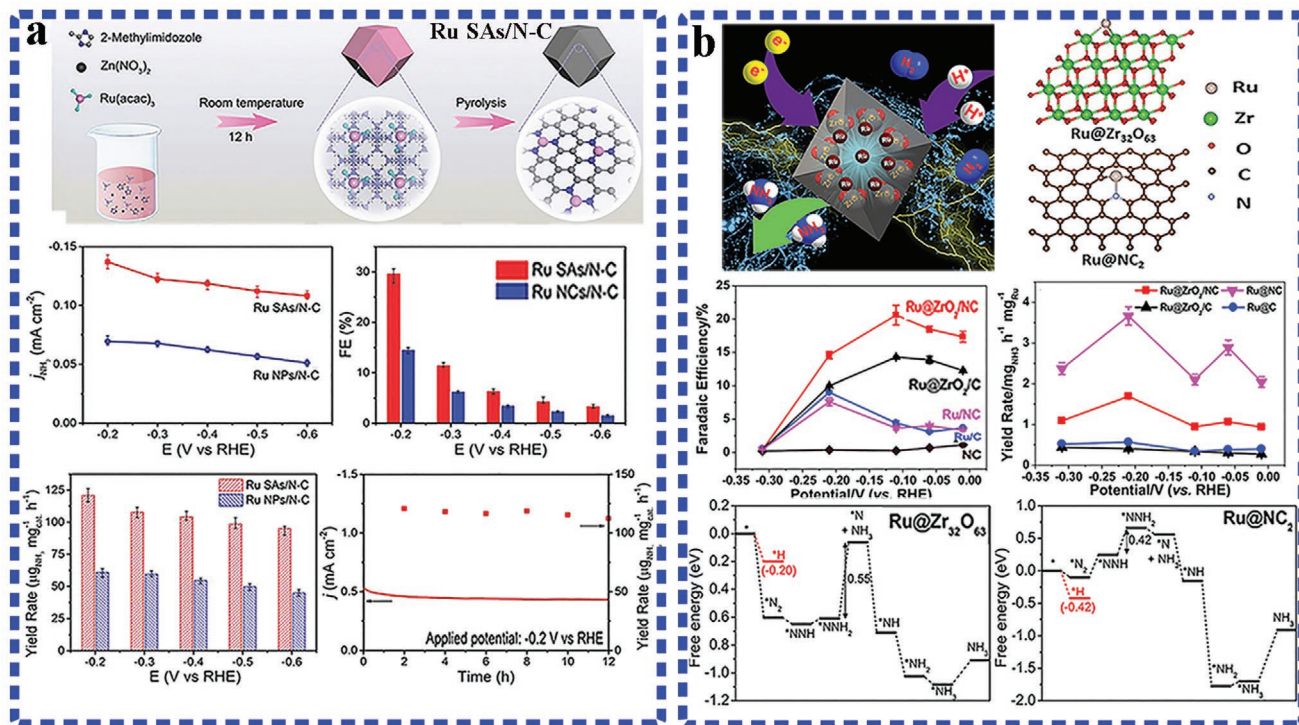


Figure 24. a) Scheme for the synthesis of Ru SAs/N-C. Current density, FE, and yield rate of NH₃ production on Ru SAs/N-C. 12 h durability test for Ru SAs/N-C toward NRR at -0.2V versus RHE. Reproduced with permission.^[79d] Copyright 2018, Wiley-VCH. b) Scheme illustration for the structure of Ru₁@ZrO₂/NC catalyst. The Faradaic efficiency and yield rate of NH₃ over Ru₁@ZrO₂/NC catalyst and counterparts. The calculation models of Ru₁@ZrO₂/NC and free-energy diagrams for NRR. Reproduced with permission.^[79c] Copyright 2019, Elsevier Ltd.

Ru₁-N₃ and Ru₁-N₄ single-atom sites, thereby resulting Ru₁/N-C with enhanced activity for the NRR. Sun and co-workers demonstrated the fabrication of Ru SAs coordinated with ZrO₂/N-doped carbon via pyrolysis of Ru-containing UiO-66 MOF (Zr₆O₄(OH)₄(BDC)₆).^[79c] As electrocatalyst in N₂ fixation, the Ru SAs from Ru₁@ZrO₂/NC significantly promoted N₂ reduction to NH₃, reaching high NH₃ formation rate of 3.665 mg_{NH₃} h⁻¹mg_{Ru}⁻¹ at -0.2 V (vs RHE), and high faradaic efficiency of 21% (at overpotential of 0.17 V), outperformed other reported SACs (Figure 24b and Table 3). Interestingly, it was found that the addition of ZrO₂ significantly suppressed side reaction of HER. The only NH₃ product suggested high selectivity of Ru₁@ZrO₂/NC catalyst for the NRR. Comparing to the performance of Ru₁@NC and Ru₁@ZrO₂/NC catalysts, the effect of ZrO₂ species in NRR performance was revealed. It was found that ZrO₂ remarkably improved the NH₃ Faradaic efficiency but did not significantly impact the NH₃ yield rate, which indicated the indispensable role of ZrO₂ in suppressing HER during the NRR. DFT calculations were performed on Ru₁@ZrO₂/NC SAC for understanding the reaction mechanism of NRR and HER. For Ru SAs in N-doped carbon, Ru@NC₂ active centers contribute to the reduction of N₂ and afford a high NH₃ yielding rate. The presence or absence of ZrO₂ in support critically impacts the Faradaic efficiency, which suggest the NRR/HER selectivity for Ru₁@ZrO₂/NC is closely related to ZrO₂ component. Therefore, Ru₁@ZrO₂/NC shows a bifunctional capability in which Ru₁@NC active sites responsible for improved NRR activity, and ZrO₂ contributes to suppress side reaction of HER.

Non-Noble Metal SACs for the NRR: M-N_x active sites consist of transition metal SACs coordinated with N atoms were reported to exhibit catalytic activity for the NRR.^[80] Xin and co-workers reported Mo SAs anchored in N-doped porous carbon (Mo₁/NPC) as an effective catalyst for NRR.^[80c] The SAC of Mo₁/NPC with 9.54 wt% Mo loading achieved high NH₃ yield rate of 34.0 ± 3.6 μg_{NH₃} h⁻¹ mg_{cat}⁻¹ and Faradaic efficiency of 14.6 ± 1.6% during the NRR. Moreover, as shown in Figure 25a, the Mo₁/NPC catalyst also displayed good NRR performance in acidic medium (0.1 M HCl). The high activity and durability without current density decay during 50 000 s NRR operation, confirmed the superior activity of transition metal Mo-N single-atom sites in boosting the NRR.

The Mo-based SACs demonstrated improved NRR performance in both acidic and alkaline media. Nevertheless, it is worth noting that neutral aqueous electrolyte can alleviate corrosion issue and benefit in reducing cost of electrochemical system. Liu and co-workers reported the electrocatalytic conversion of N₂ to NH₃ by using Fe-based SACs in the neutral media.^[80d] The Fe-SAC with high density of isolated Fe SAs dispersed in N-doped carbon frameworks (Fe_{SA}/NC) was derived from the bimetallic Fe/Zn-MOF. As electrocatalyst for NRR in 0.1 M phosphate buffer solution (PBS), the Fe_{SA}/NC catalyst exhibited a remarkable Faradaic efficiency for NH₃ product of 18.6 ± 0.8% and NH₃ yield rate of 62.9 ± 2.7 μg_{NH₃} h⁻¹ mg_{cat}⁻¹ at -0.4 V (vs RHE). DFT calculations performed on Fe_{SA}/NC catalyst for NRR are presented in Figure 25b-i-ii. It was found that N₂ molecules can adsorb on Fe atom sites via a favorable

Table 3. Summary of SACs for the NRR.

Catalyst	Metal SAs loading	Electrolyte	Maximum Faradaic efficiency [%]	NH ₃ yield rate	Durability	Active centers	Ref.
Au _{5A} -NDPCs	0.205 wt%	N ₂ -saturated 0.1 M HCl	12.3	2.32 μg h ⁻¹ cm ⁻²	No loss after 5000 s at -0.2 V (vs RHE)	Au ₁ -N/C	[79a]
Au ₁ /C ₃ N ₄	0.15 wt%	N ₂ -saturated 5 mmol L ⁻¹ H ₂ SO ₄	11.1	1305 μg h ⁻¹ mg _{Au} ⁻¹	No decay from -0.1 to -0.3 V (vs RHE)	Au ₁ -C ₃ N ₄	[79b]
Ru ₁ /N-C	0.18 wt%	N ₂ -saturated 0.05 M H ₂ SO ₄	29.6	120.9 μg _{NH₃} h ⁻¹ mg _{cat} ⁻¹	7% decay after 12 h at -0.2 V (vs RHE)	Ru ₁ -N ₃ , Ru ₁ -N ₄	[79d]
Ru ₁ @ZrO ₂ /NC	0.1 wt%	N ₂ -saturated 0.1 M HCl	21.0	3.665 mg _{NH₃} h ⁻¹ mg _{Ru} ⁻¹	Stable over 60 h at -0.21V (vs RHE)	Ru _{5A} -NC ₂	[79c]
Mo ₁ /NPC	9.54 wt%	N ₂ -saturated 0.1 M KOH	14.6 ± 1.6	34.0 ± 3.6 μg _{NH₃} h ⁻¹ mg _{cat} ⁻¹	Stable in 5000 s NRR operation	Mo _{5A} -N-C	[80c]
Mo ₁ /NPC	9.54 wt%	N ₂ -saturated 0.1 M HCl	6.8 ± 0.3	31.5 ± 1.2 μg _{NH₃} h ⁻¹ mg _{cat} ⁻¹	Stable in 5000 s NRR operation	Mo _{5A} -N-C	[80c]
Fe _{5A} /NC	4.2 wt%	N ₂ -saturated 0.1 M PBS	18.6 ± 0.8	62.9 ± 2.7 μg _{NH₃} h ⁻¹ mg _{cat} ⁻¹	Slight decay during 24 h NRR	Fe-N ₄ -C	[80d]
FePc	0.73 wt%	N ₂ -saturated 0.1 M Na ₂ SO ₄	10.5	137.95 μg h ⁻¹ mg _{FePc} ⁻¹	Stable in 30 h NRR operation	Fe-N ₄	[80g]
NPC-750	N:13.6 at%	N ₂ -saturated 0.05 M H ₂ SO ₄	–	1.40 mmol g ⁻¹ h ⁻¹	Stable during 10 cycles NRR at -0.9 V	Pyridinic and pyrrolic N	[92]
C-ZIF-1100-1 h	N:2.5 at%	N ₂ -saturated KOH	10.2	3.4 μmol cm ⁻² h ⁻¹	No decay in 18 h NRR operation	Pyridinic N	[93]

side-on configuration. The active electrons from Fe atoms were transferred to the adsorbed N₂, which extended the N≡N bond length to 1.134 Å longer than that of 1.098 Å for free N₂ molecule. Then, the atomically dispersed Fe-N₄ active sites activated N₂ molecules to produce N-N*. The enzymatic mechanism

demonstrates a lower free energy barrier of 1.69 eV (Figure 25b) which was the preferred pathway for the NRR over Fe_{5A}/NC catalyst. Electrocatalytic reduction of N₂ in neutral media is close to the biological N₂ fixation using natural nitrogenases, which shows profound significance for the conversion of N₂ into NH₃.

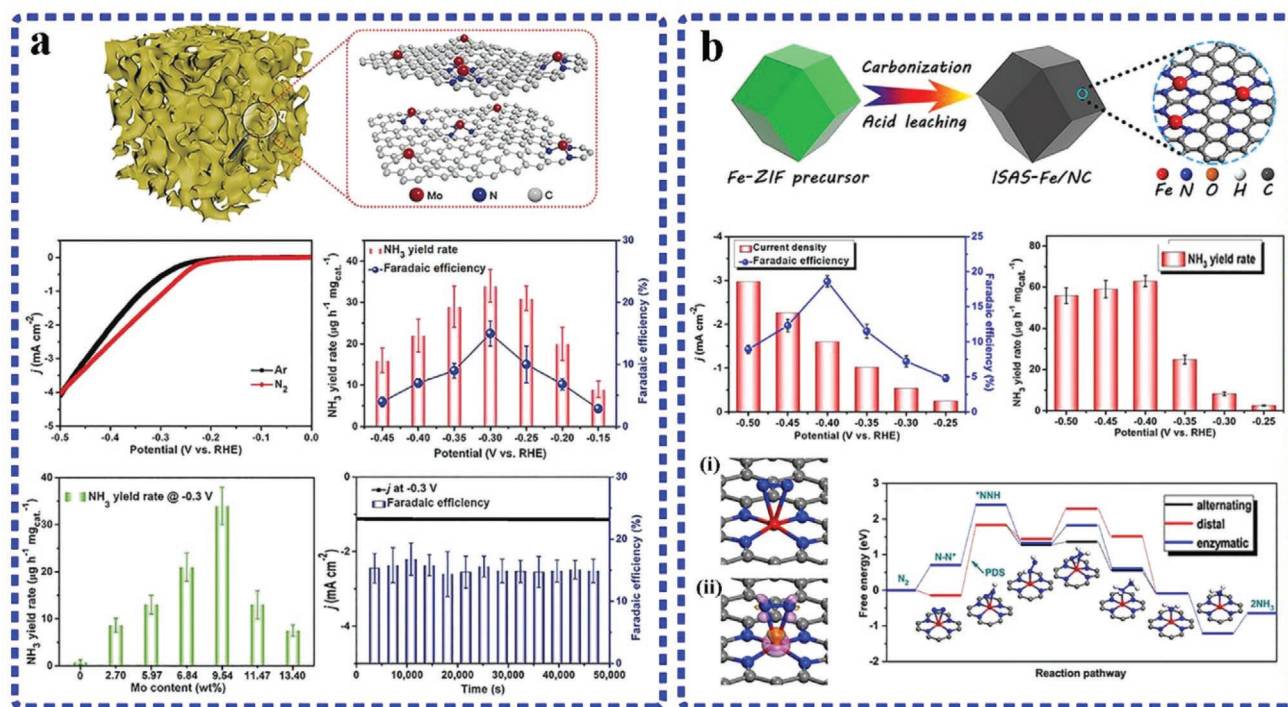


Figure 25. a) Scheme illustration of Mo₁/NPC and its atomic structure model. The LSV, NH₃ yield rate, and Faradaic efficiency stability for evaluating the NRR performance of Mo₁/NPC in 0.1 M KOH. Reproduced with permission.^[80c] Copyright 2019, Wiley-VCH. b) Scheme illustration for preparation of FeSA/NC. The current density and Faradaic efficiency measured in 0.1 M PBS solution for NRR electrochemical performance of FeSA/NC. i,ii) DFT calculations of optimized structure and the charge density difference of the N₂-adsorbed configuration on FeSA/NC. Free energy profiles for NRR on FeSA/NC with three possible pathways. Reproduced with permission.^[80d] Copyright 2019, Elsevier Ltd.

Nowadays, only limited numbers of SACs (noble metals of Ru/Au, non-noble metals of Mo/Fe) have been reported for electrochemical reduction of N₂ to synthesize NH₃. Most SACs still suffer from slow reaction kinetics, high overpotential, low Faradaic efficiency and selectivity. Therefore, it remains in highly demand to explore advanced SACs with excellent activity, selectivity and stability toward the N₂ fixation and reduction.

4.4. MOF-Derived SACs for Water Splitting

Electrocatalytic water splitting into hydrogen and oxygen evolution is considered as a renewable technology in production of hydrogen energy. The overall water splitting involves two half reactions: the cathodic HER and anodic OER. Both reactions require high-performing electrocatalysts to accelerate the dynamics and lower overpotentials.^[81] Currently, Pt and Ru-, Ir-based noble metals and oxides are the most efficient catalysts in HER and OER.^[6a,82] However, the high-cost and resource scarcity of noble metal catalysts hamper the rapid development of water splitting. To break through these barriers, investigation of cost-effective low- or non- noble metal catalysts, especially SACs with ultra-low noble metal loading and superior activity/stability are highly in demand. In this section, we will briefly summarize the exciting advances of SACs for HER and OER, with an emphasis on the progress of MOF-derived SACs and highlight the in-depth understanding of active centers in determining performance. Also, the challenges and critical issues in water splitting are discussed.

4.4.1. SACs for HER

The HER process involving H₂ production undergoes a multi-step reaction with two possible mechanisms. The HER pathway may proceed through either the Volmer–Heyrovsky mechanism (H⁺ + e⁻ → H*; H* + H⁺ + e⁻ → H₂ + *) or the Volmer–Tafel mechanism (H⁺ + e⁻ → H*; 2H* → H₂ + 2*^[82b]). The hydrogen adsorption free energy (ΔG_H) is a key parameter for evaluating HER activity. With nearly zero ΔG_H, Pt single-atom sites are considered as the best-performing catalyst for HER.^[6b,39b,83]

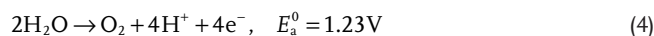
Hydrogen evolution through an electrochemical approach is the key part of clean energy conversion in water splitting and hydrogen fuel cells. Earth-abundant metal catalysts, especially transition metal–nitrogen–carbon (M–N/C, M = Co, Ni, Mo, W, etc.)^[47a,84] have been widely studied as appealing active sites in water splitting for hydrogen evolution. Among them, MOF-derived SACs made exciting progress as electrocatalysts in the HER. For example, Fan and co-workers fabricated a nickel–carbon SAC (Ni_{SAS}-C) which exhibited overpotential of -34 mV at the current density of 10 mA cm⁻², low Tafel slope of 41 mV dec⁻¹, and large exchange current density of 1.2 mA cm⁻² in 0.5 M H₂SO₄.^[84c] (as shown in **Figure 26a**). It was discovered that strong chemical and electrical coupling between Ni SAs and graphitic carbon, permit efficient electronic communication between active sites and the underlying substrate, thereby achieving Ni_{SAS}-C with excellent catalytic performance in HER.

In another case, Li and co-workers successfully achieved a W-based SAC for the HER with W SAs anchored on N-doped

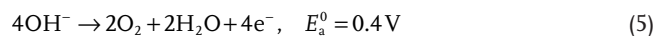
carbon matrix.^[85] The obtained W-SAC with possible local structure of W₁N₁C₃ moiety, approached low overpotential of 85 mV at current density of 10 mA cm⁻² and small Tafel slope of 53 mV dec⁻¹, indicating high electrochemical HER activity in alkaline conditions (**Figure 26b**). Additionally, it was found that the W-SAC showed long-term stability, with no appreciable activity degradation after 10 000 CV cycles. DFT calculations suggested that the most active sites of W₁N₁C₃ played an important role in optimizing the HER performance. The development of advanced Ni and W single-atom catalyst opens an avenue of Pt alternatives for the HER, which establish solid foundation in promoting practical water splitting and hydrogen evolution applications.

4.4.2. SACs for OER

The OER is a half reaction which takes place at the anode side during water splitting. It is accepted that O₂ generation during OER involved several proton/electron-coupled steps with different reaction mechanism under acidic and alkaline conditions. For example, at acidic conditions



and at alkaline conditions



The sluggish four-electron transfer kinetics of OER require high overpotential (more energy) to exceed the barrier in water oxidation, which call for innovative development of advanced SACs. For OER electrocatalysis in acid media, RuO₂ and IrO₂ are considered as the most active catalysts. However, metal corrosion and stability issue are big challenges. It was reported that coordinating Ru SAs with a Pt-rich matrix can enhance the OER activity while achieving corrosion resistant Ru SAs. Li and co-workers synthesized a series of PtCu core–shell structures decorated with atomically dispersed Ru₁.^[47b] Through rational control the PtCu_x alloy structure, the as-prepared Ru₁-Pt₃Cu delivered excellent OER activity with 220 mV overpotential at current density of 10 mA cm⁻² in 0.1 M HClO₄ electrolyte. Great stability of Ru₁-Pt₃Cu was presented with only 2.1% potential decay after 28 h of continuous electrocatalysis, well surpassing that of commercial RuO₂. Fundamental understanding in reaction mechanism was claimed that unique periodic nanoislands from Pt₃Cu provide abundant defect sites which can anchor Ru₁ SAs and ensure their excellent stability. Impressively, the almost unchanged oxidation states of Ru SAs during OER indicated their oxidation resistant nature. It was elaborated that the compressive strain of Pt skin shell effectively engineers the electronic structure of Ru SAs, which not only suppress Ru₁ overoxidation to achieve better stability in acid electrolyte but also boost the OER activity via optimizing the intermediates adsorption energy.

For OER electrocatalysis in alkaline media, the transition metal-based SACs have sparked great research interest because of their distinctive activity. Huang and co-workers

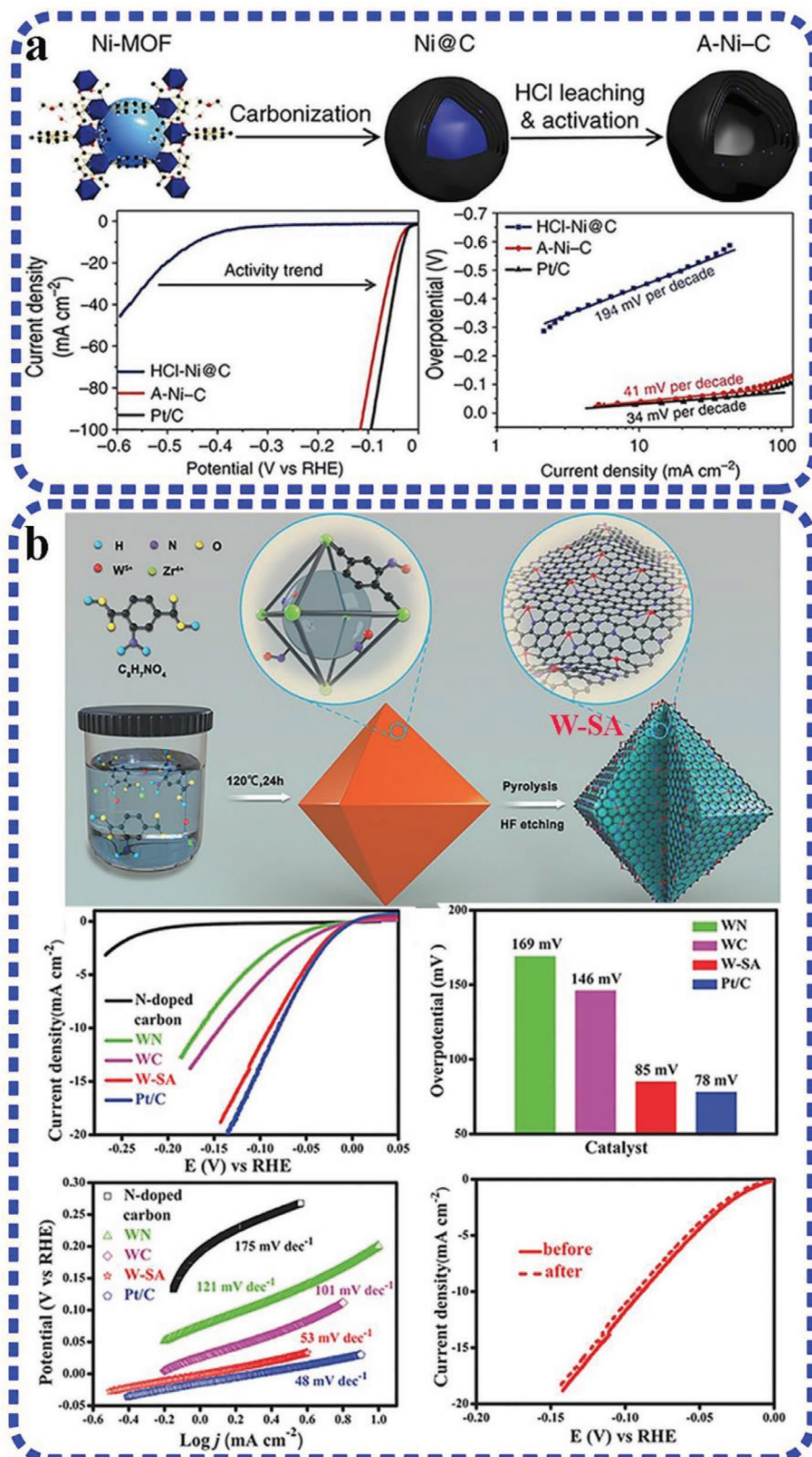


Figure 26. a) Schematic illustration for synthesis and activation of Ni_{5A}-C catalyst. HER electrocatalytic properties of the Ni_{5A}-C catalyst. Reproduced with permission.^[84] Copyright 2016, Nature Publishing Group. b) Schematic illustration of the synthesis of W-SAC. Electrocatalytic HER performance of the W-SAC in alkaline condition: the LSV curves, overpotentials, Tafel plots and long-time durability of W-SAC for HER. Reproduced with permission.^[85] Copyright 2018, Wiley-VCH.

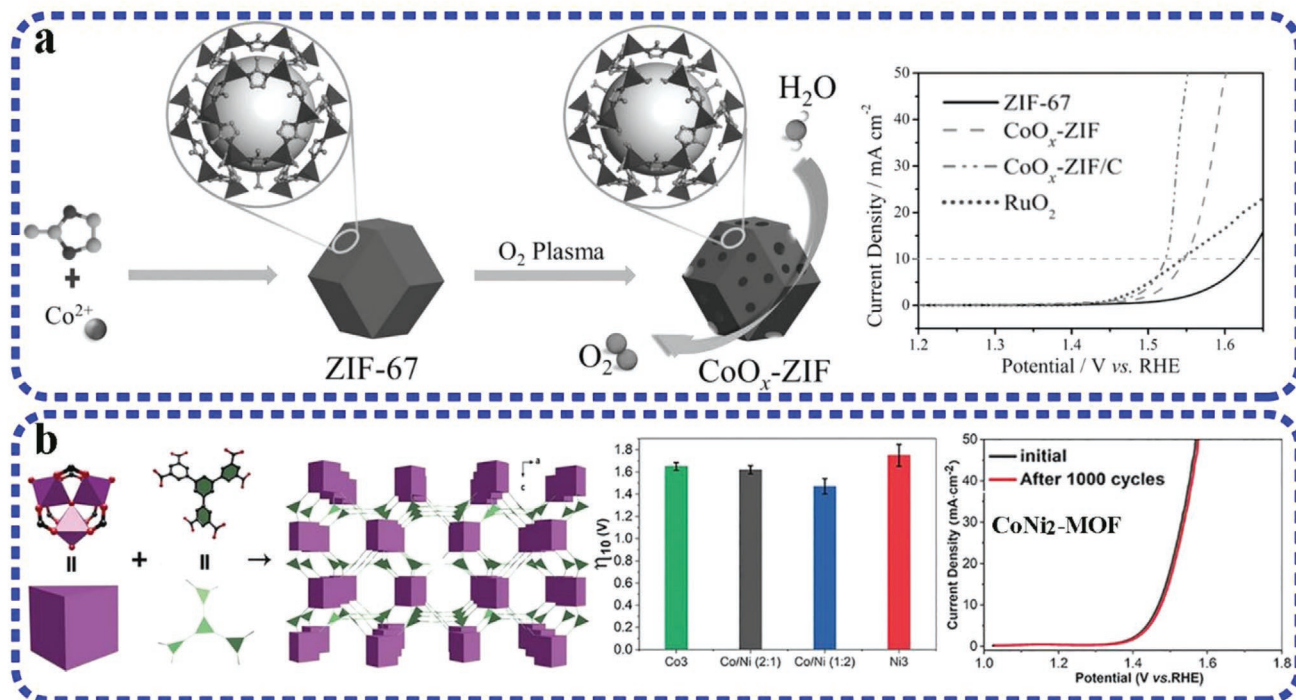


Figure 27. a) Schematic illustration of CoO_x-ZIF preparation, and LSV curves for the OER on CoO_x-ZIF catalysts. Reproduced with permission.^[89] Copyright 2017, Wiley-VCH. b) Structure illustration of M₃-MOF, the electrochemical potential and stability of as-prepared CoNi₂-MOF samples during the OER. Reproduced with permission.^[90] Copyright 2019, Wiley-VCH.

prepared a series of transition-metal SAs (Ni, Co and Fe etc.) with M-N₄C₄ sites embedded in N-doped graphene frameworks (M-NGF).^[43c] DFT calculations and electrochemical measurements demonstrated that the catalytic OER activity of M-N₄C₄ SACs follow the trend of Ni > Co > Fe. Wang and co-workers performed the O₂ plasma to on-site transform atomically distributed Co²⁺ of ZIF-67 into atomic-scale CoO_x active sites for the OER. During O₂ plasma treatment, the Co-N coordination bonds in ZIF-67 were broken and then Co reacted with O₂ thus producing CoO_x-ZIF with atomic-scale CoO_x species. The electrocatalytic OER activity of CoO_x-ZIF was studied in 1.0 M KOH. **Figure 27a** shows that CoO_x-ZIF required a potential of 1.548 V to deliver the OER current density of 10 mA cm⁻², lower than that of 1.63 V for ZIF-67. Mixed with porous carbon for conductivity compensation, the CoO_x-ZIF/C exhibited even better OER activity than RuO₂ due to the abundant active sites of CoO_x and excellent mass transport ensured by high porous feature. By poisoning the CoO_x sites with potassium thiocyanate, a negligible current can be detected for the OER, which proved that the electrocatalytic active site is the atomic-scale CoO_x from CoO_x-ZIF instead of carbon and nitrogen atoms from ZIF-67 ligand. Approximately 12 times higher specific activity of 0.0434 mA cm⁻² for CoO_x-ZIF than that of ZIF-67 (0.0034 mA cm⁻²) was indicated, demonstrating the excellent intrinsic activity of atomic-scale CoO_x sites.

Beside MOF-derived SACs, the bimetallic/trimetallic MOF with mixed atomic metal centers have been investigated as electrocatalyst toward the OER. For example, Zhou and co-workers designed the hierarchical bimetal-organic MOF structure

[NH₂(CH₃)₂][M₃(μ₃-OH)(H₂O)₃(BHB)] with alternative composition of the metal sites (M₃ = Co₃, Co₂Ni, CoNi₂, Ni₃). **Figure 27b** shows that the CoNi₂-MOF nanobelts displayed excellent OER performance with an ultralow overpotential of 240 mV to afford current density of 10 mA cm⁻², a small Tafel slope of 58 mV dec⁻¹ and a long-term stability (>50 h) in 0.1 M KOH. Notably, by alternating one Ni atom from Ni₃-MOF with Co, the bimetal CoNi₂-MOF displayed enhanced electrical conductivity and OER activity over monometallic MOF. According to DFT calculations, Co atom in CoNi₂-MOF structure was demonstrated as the active center for the OER. The role of Ni center was to cause d-band shift of Co to a higher energy level and thus improving the activity of Co center. To address low conductivity and mass transport issue which limit the utilization of bulk MOF. Design bimetal MOF crystals into 2D nanosheets or support ultrathin MOF arrays on conductive substrates have been regarded as effective solutions. For example, Tang and co-workers prepared NiCo-MOF ultrathin nanosheets (NiCo-UMOFNs) and explored their high electrocatalytic activity toward the OER.^[86] Zhao and co-workers in situ synthesis ultrathin NiFe-MOF nanosheet arrays on nickel foam and explored their atomic structure-performance relationships during OER.^[87] These examples highlight the prominent significance of SACs design from MOF precursor at atomic level, which offers great opportunities to fabricate active and stable SACs for the OER.

Electrochemical water splitting is widely considered as a critical step for renewable energy conversion involving the HER and OER. To increase the reaction kinetics and decrease the overpotential, many superior catalysts such as noble metal

SACs and transition metal SACs have been explored for electrochemical water splitting. Although much effort and great progress have been made, there is still a long way to go for the widespread application of SACs in water splitting. Design SACs with high density, excellent mass permeability, and superior electrochemical stability in both electrochemical cells and overall water splitting device should be considered in priority in the future research.^[88]

5. Summary and Perspective

MOF derived SACs with dispersed metal single atoms have shown fascinating activity in various electrochemical reactions owing to their unique characteristics of a low-coordinated environment, distinctive active centers, and maximum atom utilization efficiency. In this review, we summarize recent progress of novel SACs designed from typical MOF strategies, and the respective synthesis mechanism of each strategy are carefully discussed. Then the in situ and ex situ characterization techniques in understanding the isolated and spatial distribution, local electronic structure and coordination environment, and stable active centers for SACs are sequentially discussed. In summarizing the advanced progress of MOF-derived SACs in electrocatalysis, it can be concluded that SACs not only show excellent electrochemical performance in various reactions, but also offer extra functions in understanding different reaction mechanism and pathways. Despite great efforts that have been made in optimizing active sites and electronic structures, several key challenges for SACs still need to be overcome in order to achieve realistic high-performance and future practical application. The electrocatalytic activity, selectivity and stability must be addressed apart from the cost and availability considerations in the future design of novel electrocatalysts. The performance of SACs is strongly depending on their intrinsic properties and extrinsic factors associated with the active centers. Therefore, several technical challenges and future perspectives regarding high-performance MOF-derived single-atom catalysts should be considered.

- 1) *Single-atom sites with enhanced intrinsic activity:* To enhance the intrinsic activity, highly active metal centers should be a priority consideration. The active sites can be designed through improving their coordination environment, which could be achieved by tuning the electronic structure of SACs and thus optimizing the adsorption/desorption energy with intermediates during reaction conversions. One way in adjusting the coordination environment can be enabled by design the SAs with unsaturated coordination configuration. Emphasis should be paid on doping heteroatoms, fabricating synergistic dual-atom sites, and introducing defects into the synergistic support materials. By adjusting the specific energy of active sites, the binding energy between active sites and intermediates can be optimized and thus facilitate increased electrochemical activity.
- 2) *Accessible and dense single-atom active sites with high stability:* Increasing the loading amount of SAs active sites for more efficient catalytic performance without aggregation is of profound importance for SACs application. It is suggested that

the design of strong metal–support interactions can provide a viable route in stabilizing more SAs, which efficiently prevents the agglomeration of SAs. The population of exposed active centers for a given catalyst is the extrinsic factor which impact the catalytic activity. To maximize the exposed active centers, a catalyst morphology with hierarchical pore or hollow structure needs to be pursued. In practical applications, constructing the electrode with 3D porous architectures are highly desirable to facilitate electron transfer and mass transportation.

- 3) *Deep understanding the contribution of SACs in reaction mechanism:* A profound understanding of the active sites nature and deactivation mechanism is in high demand. Indeed, the active sites from SACs can be changed during the reaction conditions or impacted by environmental factors such as the temperature and pH of the electrolyte. Therefore, it is necessary to use in situ and operando techniques, particularly in situ HADDF-STEM and in situ XAS to monitor the SACs properties during reactions to gain a comprehensive understanding of the reaction mechanism. Ideally, a combination of in situ spectrum-electrochemical techniques with theoretical computational modeling can provide an insight into the contributions of SACs during the reaction process. This would reveal a more fundamental understanding of structure-property in SACs system and provide the fundamental guidance in designing high-performance next-generation SACs.
- 4) *Large scale SACs synthesis and practical application:* The fundamental electrode design of SACs in practical application is still inadequate. In view of the long-term development, we believe that single-atom catalysts are the ultimate performance in energy conversion applications such as fuel cells, Li-air battery, electrocatalysis of water splitting and CO₂/N₂ reduction devices. In addition to the materials challenges and solutions presented in this review, system-level concerns and solutions being pursued in the industry are also extremely important. Therefore, the industry experts are called to share their knowledge in the scientific literature to bridge the gap to convert lab efforts into the practical application goal of SACs.

In summary, the MOF-templated strategy provides a promising opportunity to generate a variety of SACs. Engineering the morphologies, structures and properties of MOF-derived SACs is helpful to improve their electrochemical performance. Continued research and development should focus on development of high-performing SACs conducive for practical application. Moreover, indicating the underlying mechanisms of conversion reactions over SACs is another significant point-cuts need to be pursued.

Acknowledgements

This research was supported by the National Natural Science Foundation of China (NSFC21905179), Natural Science and Engineering Research Council of Canada (NSERC), the Canada Research Chair Program (CRC), the Canada Foundation for Innovation (CFI), and Shenzhen University and the University of Western Ontario (UWO).

Conflict of Interest

The authors declare no conflict of interest.

Keywords

electrocatalysis, energy conversion reactions, metal–organic frameworks, single-atom catalysts

Received: May 7, 2020

Revised: July 16, 2020

Published online:

- [1] a) J. Kim, H.-E. Kim, H. Lee, *ChemSusChem* **2018**, *11*, 104; b) X.-F. Yang, A. Wang, B. Qiao, J. Li, J. Liu, T. Zhang, *Acc. Chem. Res.* **2013**, *46*, 1740; c) N. Tian, B.-A. Lu, X.-D. Yang, R. Huang, Y.-X. Jiang, Z.-Y. Zhou, S.-G. Sun, *Electrochem. Energy Rev.* **2018**, *1*, 54; d) R. Wang, H. Wang, F. Luo, S. Liao, *Electrochem. Energy Rev.* **2018**, *1*, 324; e) L. Zhang, K. Doyle-Davis, X. Sun, *Energy Environ. Sci.* **2019**, *12*, 492.
- [2] a) H. Zhang, G. Liu, L. Shi, J. Ye, *Adv. Energy Mater.* **2018**, *8*, 1701343; b) J. Liu, M. Jiao, L. Lu, H. M. Barkholtz, Y. Li, Y. Wang, L. Jiang, Z. Wu, D.-j. Liu, L. Zhuang, C. Ma, J. Zeng, B. Zhang, D. Su, P. Song, W. Xing, W. Xu, Y. Wang, Z. Jiang, G. Sun, *Nat. Commun.* **2017**, *8*, 15938; c) X. X. Wang, D. A. Cullen, Y.-T. Pan, S. Hwang, M. Wang, Z. Feng, J. Wang, M. H. Engelhard, H. Zhang, Y. He, Y. Shao, D. Su, K. L. More, J. S. Spendelov, G. Wu, *Adv. Mater.* **2018**, *30*, 1706758; d) S. Yang, J. Kim, Y. J. Tak, A. Soon, H. Lee, *Angew. Chem., Int. Ed.* **2016**, *128*, 2098; e) H. Zhang, S. Hwang, M. Wang, Z. Feng, S. Karakalos, L. Luo, Z. Qiao, X. Xie, C. Wang, D. Su, Y. Shao, G. Wu, *J. Am. Chem. Soc.* **2017**, *139*, 14143; f) Y.-Q. Su, Y. Wang, J.-X. Liu, I. A. W. Filot, K. Alexopoulos, L. Zhang, V. Muravev, B. Zijlstra, D. G. Vlachos, E. J. M. Hensen, *ACS Catal.* **2019**, *9*, 3289.
- [3] B. Qiao, A. Wang, X. Yang, L. F. Allard, Z. Jiang, Y. Cui, J. Liu, J. Li, T. Zhang, *Nat. Chem.* **2011**, *3*, 634.
- [4] S. Sun, G. Zhang, N. Gauquelin, N. Chen, J. Zhou, S. Yang, W. Chen, X. Meng, D. Geng, M. N. Banis, *Sci. Rep.* **2013**, *3*, 1775.
- [5] a) W. Zhang, W. Zheng, *Adv. Funct. Mater.* **2016**, *26*, 2988; b) J. Liu, *ACS Catal.* **2017**, *7*, 34; c) X. Li, R. Hongpan, J. Zhang, D. Wang, Y. Li, *Nano Res.* **2020**, *13*, 1842; d) C. Wan, X. Duan, Y. Huang, *Adv. Energy Mater.* **2020**, *10*, 1903815; e) S. Mitchell, E. Vorobyeva, J. Pérez-Ramírez, *Angew. Chem., Int. Ed.* **2018**, *57*, 15316; f) Y. Shi, C. Zhao, H. Wei, J. Guo, S. Liang, A. Wang, T. Zhang, J. Liu, T. Ma, *Adv. Mater.* **2014**, *26*, 8147; g) S. Mitchell, E. Vorobyeva, J. Pérez-Ramírez, *Angew. Chem., Int. Ed.* **2018**, *57*, 15316; h) Y. Peng, B. Lu, S. Chen, *Adv. Mater.* **2018**, *30*, 1801995; i) Z. Liang, W. Guo, R. Zhao, T. Qiu, H. Tabassum, R. Zou, *Nano Energy* **2019**, *64*, 103917.
- [6] a) J. Zhang, C. Liu, B. Zhang, *Small Methods* **2019**, *3*, 1800481; b) N. Cheng, S. Stambula, D. Wang, M. N. Banis, J. Liu, A. Riese, B. Xiao, R. Li, T.-K. Sham, L.-M. Liu, *Nat. Commun.* **2016**, *7*, 13638; c) L. Zhang, R. Si, H. Liu, N. Chen, Q. Wang, K. Adair, Z. Wang, J. Chen, Z. Song, J. Li, M. N. Banis, R. Li, T.-K. Sham, M. Gu, L.-M. Liu, G. A. Botton, X. Sun, *Nat. Commun.* **2019**, *10*, 4936; d) N. Cheng, L. Zhang, K. Doyle-Davis, X. Sun, *Electrochem. Energy Rev.* **2019**, *2*, 539.
- [7] a) H. Mistry, A. S. Varela, S. Kühn, P. Strasser, B. R. Cuenya, *Nat. Rev. Mater.* **2016**, *1*, 16009; b) X. Su, X.-F. Yang, Y. Huang, B. Liu, T. Zhang, *Acc. Chem. Res.* **2019**, *52*, 656; c) S. Yang, J. Kim, Y. J. Tak, A. Soon, H. Lee, *Angew. Chem., Int. Ed.* **2016**, *55*, 2058; d) D. Yang, B. C. Gates, *Nat. Mater.* **2017**, *16*, 703.
- [8] a) Z. Li, S. Ji, Y. Liu, X. Cao, S. Tian, Y. Chen, Z. Niu, Y. Li, *Chem. Rev.* **2020**, *120*, 623; b) L. Liu, A. Corma, *Chem. Rev.* **2018**, *118*, 4981; c) X. Cui, W. Li, P. Ryabchuk, K. Junge, M. Beller, *Nat. Catal.* **2018**, *1*, 385; d) Y. H. Tingting Chao, X. Hong, Y. Li, *ChemElectroChem* **2019**, *6*, 289; e) A. Wang, J. Li, T. Zhang, *Nat. Rev. Chem.* **2018**, *2*, 65; f) L. Gong, D. Zhang, C.-Y. Lin, Y. Zhu, Y. Shen, J. Zhang, X. Han, L. Zhang, Z. Xia, *Adv. Energy Mater.* **2019**, *9*, 1902625; g) Y. Wang, J. Mao, X. Meng, L. Yu, D. Deng, X. Bao, *Chem. Rev.* **2019**, *119*, 1806; h) G. Malta, S. Kondrat, S. Freakley, C. Davies, L. Lu, S. Dawson, A. Thetford, E. Gibson, D. Morgan, W. Jones, P. Wells, P. Johnston, R. Catlow, C. Kiely, G. Hutchings, *Science* **2017**, *355*, 1399.
- [9] H. Wei, X. Liu, A. Wang, L. Zhang, B. Qiao, X. Yang, Y. Huang, S. Miao, J. Liu, T. Zhang, *Nat. Commun.* **2014**, *5*, 5634.
- [10] L. DeRita, S. Dai, K. Lopez-Zepeda, N. Pham, G. W. Graham, X. Pan, P. Christopher, *J. Am. Chem. Soc.* **2017**, *139*, 14150.
- [11] a) H. Yan, H. Cheng, H. Yi, Y. Lin, T. Yao, C. Wang, J. Li, S. Wei, J. Lu, *J. Am. Chem. Soc.* **2015**, *137*, 10484; b) H. Yan, Y. Lin, H. Wu, W. Zhang, Z. Sun, H. Cheng, W. Liu, C. Wang, J. Li, X. Huang, *Nat. Commun.* **2017**, *8*, 1070; c) J. Li, Q. Guan, H. Wu, W. Liu, Y. Lin, Z. Sun, X. Ye, X. Zheng, H. Pan, J. Zhu, S. Chen, W. Zhang, S. Wei, J. Lu, *J. Am. Chem. Soc.* **2019**, *141*, 14515.
- [12] a) A. M. Abdel-Mageed, B. Rungtawevoranit, M. Parlinska-Wojtan, X. Pei, O. M. Yaghi, R. J. Behm, *J. Am. Chem. Soc.* **2019**, *141*, 5201; b) H. Zhang, J. Wei, J. Dong, G. Liu, L. Shi, P. An, G. Zhao, J. Kong, X. Wang, X. Meng, J. Zhang, J. Ye, *Angew. Chem., Int. Ed.* **2016**, *128*, 14522; c) X. Fang, Q. Shang, Y. Wang, L. Jiao, T. Yao, Y. Li, Q. Zhang, Y. Luo, H.-L. Jiang, *Adv. Mater.* **2018**, *30*, 1705112; d) Y. Zheng, S.-Z. Qiao, *Natl. Sci. Rev.* **2018**, *5*, 626; e) H.-L. J. Long Jiao, *Chem* **2019**, *5*, 786.
- [13] P. Liu, Y. Zhao, R. Qin, S. Mo, G. Chen, L. Gu, D. M. Chevrier, P. Zhang, Q. Guo, D. Zang, B. Wu, G. Fu, N. Zheng, *Science* **2016**, *352*, 797.
- [14] a) D. Zhao, Z. Zhuang, X. Cao, C. Zhang, Q. Peng, C. Chen, Y. Li, *Chem. Soc. Rev.* **2020**, *49*, 2215; b) M. Liu, L. Wang, K. Zhao, S. Shi, Q. Shao, L. Zhang, X. Sun, Y. Zhao, J. Zhang, *Energy Environ. Sci.* **2019**, *12*, 2890; c) L. Wang, W. Chen, D. Zhang, Y. Du, R. Amal, S. Qiao, J. Wu, Z. Yin, *Chem. Soc. Rev.* **2019**, *48*, 5310; d) S. Ji, Y. Chen, X. Wang, Z. Zhang, D. Wang, Y. Li, *Chem. Rev.* **2020**, <https://doi.org/10.1021/acs.chemrev.9b00818>.
- [15] a) H. Huang, K. Shen, F. Chen, Y. Li, *ACS Catal.* **2020**, *10*, 6579; b) A. Han, B. Wang, A. Kumar, Y. Qin, J. Jin, X. Wang, C. Yang, B. Dong, Y. Jia, J. Liu, X. Sun, *Small Methods* **2019**, *3*, 1800471.
- [16] B. Liu, H. Shioyama, T. Akita, Q. Xu, *J. Am. Chem. Soc.* **2008**, *130*, 5390.
- [17] a) Z. Liang, R. Zhao, T. Qiu, R. Zou, Q. Xu, *EnergyChem* **2019**, *1*, 100001; b) C.-C. Hou, H.-F. Wang, C. Li, Q. Xu, *Energy Environ. Sci.* **2020**, *13*, 1658; c) Y.-S. Wei, M. Zhang, R. Zou, Q. Xu, *Chem. Rev.* **2020**, <https://doi.org/10.1021/acs.chemrev.9b00757>.
- [18] a) C. Zhu, S. Fu, Q. Shi, D. Du, Y. Lin, *Angew. Chem., Int. Ed.* **2017**, *56*, 13944; b) H. Zhang, G. Liu, L. Shi, J. Ye, *Adv. Mater.* **2018**, *8*, 1701343.
- [19] a) H.-F. Wang, L. Chen, H. Pang, S. Kaskel, Q. Xu, *Chem. Soc. Rev.* **2020**, *49*, 1414; b) Q. Wang, D. Astruc, *Chem. Rev.* **2020**, *120*, 1438; c) X. F. Lu, B. Y. Xia, S.-Q. Zang, X. W. Lou, *Angew. Chem., Int. Ed.* **2020**, *59*, 4634.
- [20] X. X. Wang, D. A. Cullen, Y.-T. Pan, S. Hwang, M. Wang, Z. Feng, J. Wang, M. H. Engelhard, H. Zhang, Y. He, Y. Shao, D. Su, K. L. More, J. S. Spendelov, G. Wu, *Adv. Mater.* **2018**, *30*, 1706758.
- [21] a) P. Yin, T. Yao, Y. Wu, L. Zheng, Y. Lin, W. Liu, H. Ju, J. Zhu, X. Hong, Z. Deng, G. Zhou, S. Wei, Y. Li, *Angew. Chem., Int. Ed.* **2016**, *55*, 10800; b) X. Wang, Z. Chen, X. Zhao, T. Yao, W. Chen, R. You, C. Zhao, G. Wu, J. Wang, W. Huang, J. Yang, X. Hong, S. Wei, Y. Wu, Y. Li, *Angew. Chem., Int. Ed.* **2018**, *57*, 1944.

- [22] Y. He, S. Hwang, D. A. Cullen, M. A. Uddin, L. Langhorst, B. Li, S. Karakalos, A. J. Kropf, E. C. Wegener, J. Sokolowski, M. Chen, D. Myers, D. Su, K. L. More, G. Wang, S. Litster, G. Wu, *Energy Environ. Sci.* **2019**, *12*, 250.
- [23] R. C. Klet, T. C. Wang, L. E. Fernandez, D. G. Truhlar, J. T. Hupp, O. K. Farha, *Chem. Mater.* **2016**, *28*, 1213.
- [24] C. Zhao, X. Dai, T. Yao, W. Chen, X. Wang, J. Wang, J. Yang, S. Wei, Y. Wu, Y. Li, *J. Am. Chem. Soc.* **2017**, *139*, 8078.
- [25] Y. Chen, S. Ji, S. Zhao, W. Chen, J. Dong, W.-C. Cheong, R. Shen, X. Wen, L. Zheng, A. I. Rykov, S. Cai, H. Tang, Z. Zhuang, C. Chen, Q. Peng, D. Wang, Y. Li, *Nat. Commun.* **2018**, *9*, 5422.
- [26] X. Wang, W. Chen, L. Zhang, T. Yao, W. Liu, Y. Lin, H. Ju, J. Dong, L. Zheng, W. Yan, X. Zheng, Z. Li, X. Wang, J. Yang, D. He, Y. Wang, Z. Deng, Y. Wu, Y. Li, *J. Am. Chem. Soc.* **2017**, *139*, 9419.
- [27] T. He, S. Chen, B. Ni, Y. Gong, Z. Wu, L. Song, L. Gu, W. Hu, X. Wang, *Angew. Chem., Int. Ed.* **2018**, *57*, 3493.
- [28] a) L. Jiao, G. Wan, R. Zhang, H. Zhou, S.-H. Yu, H.-L. Jiang, *Angew. Chem., Int. Ed.* **2018**, *57*, 8525; b) L. Jiao, R. Zhang, G. Wan, W. Yang, X. Wan, H. Zhou, J. Shui, S.-H. Yu, H.-L. Jiang, *Nat. Commun.* **2020**, *11*, 2831.
- [29] a) Y. Chen, S. Ji, Y. Wang, J. Dong, W. Chen, Z. Li, R. Shen, L. Zheng, Z. Zhuang, D. Wang, Y. Li, *Angew. Chem., Int. Ed.* **2017**, *56*, 6937; b) S. Ji, Y. Chen, Q. Fu, Y. Chen, J. Dong, W. Chen, Z. Li, Y. Wang, L. Gu, W. He, C. Chen, Q. Peng, Y. Huang, X. Duan, D. Wang, C. Draxl, Y. Li, *J. Am. Chem. Soc.* **2017**, *139*, 9795; c) J. Wang, G. Han, L. Wang, L. Du, G. Chen, Y. Gao, Y. Ma, C. Du, X. Cheng, P. Zuo, G. Yin, *Small* **2018**, *14*, 1704282; d) J. Han, X. Meng, L. Lu, J. Bian, Z. Li, C. Sun, *Adv. Funct. Mater.* **2019**, *29*, 1808872.
- [30] J. Jones, H. Xiong, A. T. DeLaRiva, E. J. Peterson, H. Pham, S. R. Challa, G. Qi, S. Oh, M. H. Wiebenga, X. I. Pereira Hernández, Y. Wang, A. K. Datye, *Science* **2016**, *353*, 150.
- [31] S. Wei, A. Li, J.-C. Liu, Z. Li, W. Chen, Y. Gong, Q. Zhang, W.-C. Cheong, Y. Wang, L. Zheng, H. Xiao, C. Chen, D. Wang, Q. Peng, L. Gu, X. Han, J. Li, Y. Li, *Nat. Nanotechnol.* **2018**, *13*, 856.
- [32] J. Yang, Z. Qiu, C. Zhao, W. Wei, W. Chen, Z. Li, Y. Qu, J. Dong, J. Luo, Z. Li, Y. Wu, *Angew. Chem., Int. Ed.* **2018**, *57*, 14095.
- [33] a) Y. Qu, Z. Li, W. Chen, Y. Lin, T. Yuan, Z. Yang, C. Zhao, J. Wang, C. Zhao, X. Wang, F. Zhou, Z. Zhuang, Y. Wu, Y. Li, *Nat. Catal.* **2018**, *1*, 781; b) Y. Qu, B. Chen, Z. Li, X. Duan, L. Wang, Y. Lin, T. Yuan, F. Zhou, Y. Hu, Z. Yang, C. Zhao, J. Wang, C. Zhao, Y. Hu, G. Wu, Q. Zhang, Q. Xu, B. Liu, P. Gao, R. You, W. Huang, L. Zheng, L. Gu, Y. Wu, Y. Li, *J. Am. Chem. Soc.* **2019**, *141*, 4505.
- [34] a) J. R. Ran, J. T. Qu, H. P. Zhang, T. Wen, H. L. Wang, S. M. Chen, L. Song, X. L. Zhang, L. Q. Jing, R. K. Zheng, S. Z. Qiao, *Adv. Energy Mater.* **2019**, *9*, 1803402; b) Q. Mu, W. Zhu, X. Li, C. Zhang, Y. Su, Y. Lian, P. Qi, Z. Deng, D. Zhang, S. Wang, X. Zhu, Y. Peng, *Appl. Catal., B* **2020**, *262*, 118144; c) Q. Zuo, T. T. Liu, C. S. Chen, Y. Ji, X. Q. Gong, Y. Y. Mai, Y. F. Zhou, *Angew. Chem., Int. Ed.* **2019**, *58*, 10198; d) T. He, B. Ni, S. M. Zhang, Y. Gong, H. Q. Wang, L. Gu, J. Zhuang, W. P. Hu, X. Wang, *Small* **2018**, *14*, 6; e) J. Wang, N. Li, Y. Xu, H. Pang, *Chem. - Eur. J.* **2020**, *26*, 6402; f) H. Yang, X. Wang, *Adv. Mater.* **2019**, *31*, 1800743; g) X. Li, D.-D. Ma, C. Cao, R. Zou, Q. Xu, X.-T. Wu, Q.-L. Zhu, *Small* **2019**, *15*, 1902218.
- [35] a) Y. Zhu, J. Sokolowski, X. Song, Y. He, Y. Mei, G. Wu, *Adv. Energy Mater.* **2020**, *10*, 1902844; b) Y. He, S. Liu, C. Priest, Q. Shi, G. Wu, *Chem. Soc. Rev.* **2020**, *49*, 3484.
- [36] G. Yilmaz, S. B. Peh, D. Zhao, G. W. Ho, *Adv. Sci.* **2019**, *6*, 1901129.
- [37] a) Y. Yao, Z. Huang, P. Xie, L. Wu, L. Ma, T. Li, Z. Pang, M. Jiao, Z. Liang, J. Gao, Y. He, D. J. Kline, M. R. Zachariah, C. Wang, J. Lu, T. Wu, T. Li, C. Wang, R. Shahbazian-Yassar, L. Hu, *Nat. Nanotechnol.* **2019**, *14*, 851; b) X. Li, X. Yang, J. Zhang, Y. Huang, B. Liu, *ACS Catal.* **2019**, *9*, 2521; c) L. Liu, D. N. Zakharov, R. Arenal, P. Concepcion, E. A. Stach, A. Corma, *Nat. Commun.* **2018**, *9*, 574.
- [38] a) R. Lang, W. Xi, J.-C. Liu, Y.-T. Cui, T. Li, A. F. Lee, F. Chen, Y. Chen, L. Li, L. Li, J. Lin, S. Miao, X. Liu, A.-Q. Wang, X. Wang, J. Luo, B. Qiao, J. Li, T. Zhang, *Nat. Commun.* **2019**, *10*, 234; b) T.-Y. Chang, Y. Tanaka, R. Ishikawa, K. Toyoura, K. Matsunaga, Y. Ikuhara, N. Shibata, *Nano Lett.* **2014**, *14*, 134.
- [39] a) D. Deng, X. Chen, L. Yu, X. Wu, Q. Liu, Y. Liu, H. Yang, H. Tian, Y. Hu, P. Du, R. Si, J. Wang, X. Cui, H. Li, J. Xiao, T. Xu, J. Deng, F. Yang, P. N. Duchesne, P. Zhang, J. Zhou, L. Sun, J. Li, X. Pan, X. Bao, *Sci. Adv.* **2015**, *1*, e1500462; b) J. Deng, H. Li, J. Xiao, Y. Tu, D. Deng, H. Yang, H. Tian, J. Li, P. Ren, X. Bao, *Energy Environ. Sci.* **2015**, *8*, 1594; c) H. Li, S. Wang, H. Sawada, G. G. D. Han, T. Samuels, C. S. Allen, A. I. Kirkland, J. C. Grossman, J. H. Warner, *ACS Nano* **2017**, *11*, 3392.
- [40] a) T. Sun, L. Xu, D. Wang, Y. J. N. R. Li, *Nano Res.* **2019**, *12*, 2067; b) Z. Liang, C. Qu, D. Xia, R. Zou, Q. Xu, *Angew. Chem., Int. Ed.* **2018**, *57*, 9604.
- [41] S. Stambula, N. Gauquelin, M. Bugnet, S. Gorantla, S. Turner, S. Sun, J. Liu, G. Zhang, X. Sun, G. A. Botton, *J. Phys. Chem. C* **2014**, *118*, 3890.
- [42] L. Weiha, L. Minsi, H. Yongfeng, L. Jun, L. Andrew, L. Ruying, W. Tianpin, S. Tsun-Kong, S. Xueliang, *Small Methods* **2018**, *2*, 1700341.
- [43] a) Q. Jia, N. Ramaswamy, H. Hafiz, U. Tylus, K. Strickland, G. Wu, B. Barbiellini, A. Bansil, E. F. Holby, P. Zelenay, S. Mukerjee, *ACS Nano* **2015**, *9*, 12496; b) A. Zitolo, V. Goellner, V. Armel, M.-T. Sougrati, T. Mineva, L. Stievenato, E. Fonda, F. Jaouen, *Nat. Mater.* **2015**, *14*, 937; c) H. Fei, J. Dong, Y. Feng, C. S. Allen, C. Wan, B. Voloskiy, M. Li, Z. Zhao, Y. Wang, H. Sun, P. An, W. Chen, Z. Guo, C. Lee, D. Chen, I. Shakir, M. Liu, T. Hu, Y. Li, A. I. Kirkland, X. Duan, Y. Huang, *Nat. Catal.* **2018**, *1*, 63.
- [44] A. I. Frenkel, *Chem. Soc. Rev.* **2012**, *41*, 8163.
- [45] a) M. Xiao, J. Zhu, L. Ma, Z. Jin, J. Ge, X. Deng, Y. Hou, Q. He, J. Li, Q. Jia, S. Mukerjee, R. Yang, Z. Jiang, D. Su, C. Liu, W. Xing, *ACS Catal.* **2018**, *8*, 2824; b) A. Zitolo, N. Ranjbar-Sahraie, T. Mineva, J. Li, Q. Jia, S. Stamatini, G. F. Harrington, S. M. Lyth, P. Krtil, S. Mukerjee, E. Fonda, F. Jaouen, *Nat. Commun.* **2017**, *8*, 957.
- [46] a) H. B. Yang, S.-F. Hung, S. Liu, K. Yuan, S. Miao, L. Zhang, X. Huang, H.-Y. Wang, W. Cai, R. Chen, J. Gao, X. Yang, W. Chen, Y. Huang, H. M. Chen, C. M. Li, T. Zhang, B. Liu, *Nat. Energy* **2018**, *3*, 140; b) K. Jiang, S. Siahrostami, T. Zheng, Y. Hu, S. Hwang, E. Stavitski, Y. Peng, J. Dynes, M. Gangisetty, D. Su, K. Attenkofer, H. Wang, *Energy Environ. Sci.* **2018**, *11*, 893; c) Z. Zhang, J. Xiao, X.-J. Chen, S. Yu, L. Yu, R. Si, Y. Wang, S. Wang, X. Meng, Y. Wang, Z.-Q. Tian, D. Deng, *Angew. Chem., Int. Ed.* **2018**, *57*, 16339.
- [47] a) L. Cao, Q. Luo, W. Liu, Y. Lin, X. Liu, Y. Cao, W. Zhang, Y. Wu, J. Yang, T. Yao, S. Wei, *Nat. Catal.* **2019**, *2*, 134; b) Y. Yao, S. Hu, W. Chen, Z.-Q. Huang, W. Wei, T. Yao, R. Liu, K. Zang, X. Wang, G. Wu, W. Yuan, T. Yuan, B. Zhu, W. Liu, Z. Li, D. He, Z. Xue, Y. Wang, X. Zheng, J. Dong, C.-R. Chang, Y. Chen, X. Hong, J. Luo, S. Wei, W.-X. Li, P. Strasser, Y. Wu, Y. Li, *Nat. Catal.* **2019**, *2*, 304; c) T. Sun, S. Zhao, W. Chen, D. Zhai, J. Dong, Y. Wang, S. Zhang, A. Han, L. Gu, R. Yu, X. Wen, H. Ren, L. Xu, C. Chen, Q. Peng, D. Wang, Y. Li, *Proc. Natl. Acad. Sci. USA* **2018**, *115*, 12692.
- [48] a) J. P. Simonovis, A. Hunt, R. M. Palomino, S. D. Senanayake, I. Waluyo, *J. Phys. Chem. C* **2018**, *122*, 4488; b) L. Nguyen, S. Zhang, L. Wang, Y. Li, H. Yoshida, A. Patlolla, S. Takeda, A. I. Frenkel, F. Tao, *ACS Catal.* **2016**, *6*, 840; c) A. Bruix, Y. Lykhach, I. Matolínová, A. Neitzel, T. Skála, N. Tsud, M. Vorokhta, V. Stetsovych, K. Ševčíková, J. Mysliveček, R. Fiala, M. Václavů, K. C. Prince, S. Bruyère, V. Potin, F. Illas, V. Matolín, J. Libuda, K. M. Neyman, *Angew. Chem., Int. Ed.* **2014**, *53*, 10525.
- [49] a) K. Ding, A. Gulec, A. M. Johnson, N. M. Schweitzer, G. D. Stucky, L. D. Marks, P. C. Stair, *Science* **2015**, *350*, 189; b) J. C. Matsubu, V. N. Yang, P. Christopher, *J. Am. Chem. Soc.* **2015**, *137*, 3076; c) D. Yang, P. Xu, N. D. Browning, B. C. Gates, *J. Phys. Chem. Lett.* **2016**, *7*, 2537.

- [50] J. Li, H. Zhang, W. Samarakoon, W. Shan, D. Cullen, S. Karakalos, M. Chen, D. Gu, K. More, G. Wang, Z. Feng, Z. Wang, G. Wu, *Angew. Chem., Int. Ed.* **2019**, *58*, 18971.
- [51] X. Zeng, J. Shui, X. Liu, Q. Liu, Y. Li, J. Shang, L. Zheng, R. Yu, *Adv. Energy Mater.* **2018**, *8*, 1701345.
- [52] a) J. Liu, M. Jiao, B. Mei, Y. Tong, Y. Li, M. Ruan, P. Song, G. Sun, L. Jiang, Y. Wang, Z. Jiang, L. Gu, Z. Zhou, W. Xu, *Angew. Chem., Int. Ed.* **2019**, *58*, 1163; b) S. Yang, Y. J. Tak, J. Kim, A. Soon, H. Lee, *ACS Catal.* **2017**, *7*, 1301; c) C. Zhang, J. Sha, H. Fei, M. Liu, S. Yazdi, J. Zhang, Q. Zhong, X. Zou, N. Zhao, H. Yu, Z. Jiang, E. Ringe, B. I. Yakobson, J. Dong, D. Chen, J. M. Tour, *ACS Nano* **2017**, *11*, 6930.
- [53] C. H. Choi, M. Kim, H. C. Kwon, S. J. Cho, S. Yun, H.-T. Kim, K. J. J. Mayrhofer, H. Kim, M. Choi, *Nat. Commun.* **2016**, *7*, 10922.
- [54] a) H. Zhang, H. T. Chung, D. A. Cullen, S. Wagner, U. I. Kramm, K. L. More, P. Zelenay, G. Wu, *Energy Environ. Sci.* **2019**, *12*, 2548; b) J.-D. Yi, R. Xu, Q. Wu, T. Zhang, K.-T. Zang, J. Luo, Y.-L. Liang, Y.-B. Huang, R. Cao, *ACS Energy Lett.* **2018**, *3*, 883; c) X. Wan, X. Liu, Y. Li, R. Yu, L. Zheng, W. Yan, H. Wang, M. Xu, J. Shui, *Nat. Catal.* **2019**, *2*, 259; d) Q. Lai, L. R. Zheng, Y. Y. Liang, J. He, J. Zhao, J. Chen, *ACS Catal.* **2017**, *7*, 1655; e) R. Jiang, L. Li, T. Sheng, G. Hu, Y. Chen, L. Wang, *J. Am. Chem. Soc.* **2018**, *140*, 11594; f) Y. Chen, Z. Li, Y. Zhu, D. Sun, X. Liu, L. Xu, Y. Tang, *Adv. Mater.* **2019**, *31*, 1806312; g) P. Chen, T. Zhou, L. Xing, K. Xu, Y. Tong, H. Xie, L. Zhang, W. Yan, W. Chu, C. Wu, Y. Xie, *Angew. Chem., Int. Ed.* **2017**, *56*, 610; h) L. Yang, D. Cheng, H. Xu, X. Zeng, X. Wan, J. Shui, Z. Xiang, D. Cao, *Proc. Natl. Acad. Sci. USA* **2018**, *115*, 6626; i) Q. Li, W. Chen, H. Xiao, Y. Gong, Z. Li, L. Zheng, X. Zheng, W. Yan, W.-C. Cheong, R. Shen, N. Fu, L. Gu, Z. Zhuang, C. Chen, D. Wang, Q. Peng, J. Li, Y. Li, *Adv. Mater.* **2018**, *30*, 1800588.
- [55] Y. Chen, S. Ji, S. Zhao, W. Chen, J. Dong, W.-C. Cheong, R. Shen, X. Wen, L. Zheng, A. I. Rykov, S. Cai, H. Tang, Z. Zhuang, C. Chen, Q. Peng, D. Wang, Y. Li, *Nat. Commun.* **2018**, *9*, 5422.
- [56] C.-C. Hou, L. Zou, L. Sun, K. Zhang, Z. Liu, Y. Li, C. Li, R. Zou, J. Yu, Q. Xu, *Angew. Chem., Int. Ed.* **2020**, *59*, 7384.
- [57] J. Li, M. Chen, D. A. Cullen, S. Hwang, M. Wang, B. Li, K. Liu, S. Karakalos, M. Lucero, H. Zhang, C. Lei, H. Xu, G. E. Sterbinsky, Z. Feng, D. Su, K. L. More, G. Wang, Z. Wang, G. Wu, *Nat. Catal.* **2018**, *1*, 935.
- [58] Z. Yang, B. Chen, W. Chen, Y. Qu, F. Zhou, C. Zhao, Q. Xu, Q. Zhang, X. Duan, Y. Wu, *Nat. Commun.* **2019**, *10*, 3734.
- [59] P. Song, M. Luo, X. Liu, W. Xing, W. Xu, Z. Jiang, L. Gu, *Adv. Funct. Mater.* **2017**, *27*, 1700802.
- [60] J. Li, S. Chen, N. Yang, M. Deng, S. Ibraheem, J. Deng, J. Li, L. Li, Z. Wei, *Angew. Chem., Int. Ed.* **2019**, *58*, 7035.
- [61] a) J. Wang, W. Liu, G. Luo, Z. Li, C. Zhao, H. Zhang, M. Zhu, Q. Xu, X. Wang, C. Zhao, Y. Qu, Z. Yang, T. Yao, Y. Li, Y. Lin, Y. Wu, Y. Li, *Energy Environ. Sci.* **2018**, *11*, 3375; b) J. Wang, Z. Huang, W. Liu, C. Chang, H. Tang, Z. Li, W. Chen, C. Jia, T. Yao, S. Wei, Y. Wu, Y. Li, *J. Am. Chem. Soc.* **2017**, *139*, 17281; c) R. Zhao, Z. Liang, S. Gao, C. Yang, B. Zhu, J. Zhao, C. Qu, R. Zou, Q. Xu, *Angew. Chem., Int. Ed.* **2019**, *58*, 1975; d) D. Zhang, W. Chen, Z. Li, Y. Chen, L. Zheng, Y. Gong, Q. Li, R. Shen, Y. Han, W. Cheong, L. Gu, Y. Li, *Chem. Commun.* **2018**, *54*, 4274.
- [62] Z. Lu, B. Wang, Y. Hu, W. Liu, Y. Zhao, R. Yang, Z. Li, J. Luo, B. Chi, Z. Jiang, M. Li, S. Mu, S. Liao, J. Zhang, X. Sun, *Angew. Chem., Int. Ed.* **2019**, *131*, 2648.
- [63] a) Y. Y. Birdja, E. Pérez-Gallent, M. C. Figueiredo, A. J. Göttle, F. Calle-Vallejo, M. T. M. Koper, *Nat. Energy* **2019**, *4*, 732; b) T. Zheng, K. Jiang, H. Wang, *Adv. Mater.* **2018**, *30*, 1802066; c) K. Jiang, R. B. Sandberg, A. J. Akey, X. Liu, D. C. Bell, J. K. Nørskov, K. Chan, H. Wang, *Nat. Catal.* **2018**, *1*, 111; d) J. Shen, R. Kortlever, R. Kas, Y. Y. Birdja, O. Diaz-Morales, Y. Kwon, I. Ledezma-Yanez, K. J. P. Schouten, G. Mul, M. T. M. Koper, *Nat. Commun.* **2015**, *6*, 8177; e) Y. Zhou, F. Che, M. Liu, C. Zou, Z. Liang, P. De Luna, H. Yuan, J. Li, Z. Wang, H. Xie, H. Li, P. Chen, E. Bladt, R. Quintero-Bermudez, T.-K. Sham, S. Bals, J. Hofkens, D. Sinton, G. Chen, E. H. Sargent, *Nat. Chem.* **2018**, *10*, 974; f) Q. Yang, C.-C. Yang, C.-H. Lin, H.-L. Jiang, *Angew. Chem., Int. Ed.* **2019**, *58*, 3511.
- [64] a) H. Zhang, J. Li, Q. Tan, L. Lu, Z. Wang, G. Wu, *Chem. - Eur. J.* **2018**, *24*, 18137; b) Q. Lu, F. Jiao, *Nano Energy* **2016**, *29*, 439; c) M. G. Kibria, J. P. Edwards, C. M. Gabardo, C.-T. Dinh, A. Seifitokaldani, D. Sinton, E. H. Sargent, *Adv. Mater.* **2019**, *31*, 1807166; d) S. Zhang, Q. Fan, R. Xia, T. J. Meyer, *Acc. Chem. Res.* **2020**, *53*, 255.
- [65] a) D. Zhao, Z. Chen, W. Yang, S. Liu, X. Zhang, Y. Yu, W.-C. Cheong, L. Zheng, F. Ren, G. Ying, X. Cao, D. Wang, Q. Peng, G. Wang, C. Chen, *J. Am. Chem. Soc.* **2019**, *141*, 4086; b) C. Zhao, Y. Wang, Z. Li, W. Chen, Q. Xu, D. He, D. Xi, Q. Zhang, T. Yuan, Y. Qu, J. Yang, F. Zhou, Z. Yang, X. Wang, J. Wang, J. Luo, Y. Li, H. Duan, Y. Wu, Y. Li, *Joule* **2019**, *3*, 584; c) C. Zhang, S. Yang, J. Wu, M. Liu, S. Yazdi, M. Ren, J. Sha, J. Zhong, K. Nie, A. S. Jalilov, Z. Li, H. Li, B. I. Yakobson, Q. Wu, E. Ringe, H. Xu, P. M. Ajayan, J. M. Tour, *Adv. Energy Mater.* **2018**, *8*, 1703487; d) J. G. Chen, *Joule* **2018**, *2*, 587.
- [66] a) M. Jia, Q. Fan, S. Liu, J. Qiu, Z. Sun, *Curr. Opin. Green Sustainable Chem.* **2019**, *16*, 1; b) Y.-N. Gong, L. Jiao, Y. Qian, C.-Y. Pan, L. Zheng, X. Cai, B. Liu, S.-H. Yu, H.-L. Jiang, *Angew. Chem., Int. Ed.* **2020**, *59*, 2705.
- [67] C. Yan, H. Li, Y. Ye, H. Wu, F. Cai, R. Si, J. Xiao, S. Miao, S. Xie, F. Yang, Y. Li, G. Wang, X. Bao, *Energy Environ. Sci.* **2018**, *11*, 1204.
- [68] Y. Pan, R. Lin, Y. Chen, S. Liu, W. Zhu, X. Cao, W. Chen, K. Wu, W.-C. Cheong, Y. Wang, L. Zheng, J. Luo, Y. Lin, Y. Liu, C. Liu, J. Li, Q. Lu, X. Chen, D. Wang, Q. Peng, C. Chen, Y. Li, *J. Am. Chem. Soc.* **2018**, *140*, 4218.
- [69] a) T. N. Huan, N. Ranjbar, G. Rousse, M. Sougrati, A. Zitolo, V. Mougel, F. Jaouen, M. Fontecave, *ACS Catal.* **2017**, *7*, 1520; b) H. Zhang, J. Li, S. Xi, Y. Du, X. Hai, J. Wang, H. Xu, G. Wu, J. Zhang, J. Lu, J. Wang, *Angew. Chem., Int. Ed.* **2019**, *58*, 14871; c) X. Chen, D.-D. Ma, B. Chen, K. Zhang, R. Zou, X.-T. Wu, Q.-L. Zhu, *Appl. Catal., B* **2020**, *267*, 118720.
- [70] F. Pan, H. Zhang, K. Liu, D. Cullen, K. More, M. Wang, Z. Feng, G. Wang, G. Wu, Y. Li, *ACS Catal.* **2018**, *8*, 3116.
- [71] W. Ren, X. Tan, W. Yang, C. Jia, S. Xu, K. Wang, S. C. Smith, C. Zhao, *Angew. Chem., Int. Ed.* **2019**, *131*, 7046.
- [72] a) Y. Wang, Z. Chen, P. Han, Y. Du, Z. Gu, X. Xu, G. Zheng, *ACS Catal.* **2018**, *8*, 7113; b) H. Yang, Y. Wu, G. Li, Q. Lin, Q. Hu, Q. Zhang, J. Liu, C. He, *J. Am. Chem. Soc.* **2019**, *141*, 12717; c) R. Long, Y. Li, Y. Liu, S. Chen, X. Zheng, C. Gao, C. He, N. Chen, Z. Qi, L. Song, J. Jiang, J. Zhu, Y. Xiong, *J. Am. Chem. Soc.* **2017**, *139*, 4486; d) M.-J. Cheng, E. L. Clark, H. H. Pham, A. T. Bell, M. Head-Gordon, *ACS Catal.* **2016**, *6*, 7769; e) X. Shao, X. Yang, J. Xu, S. Liu, S. Miao, X. Liu, X. Su, H. Duan, Y. Huang, T. Zhang, *Chem* **2019**, *5*, 693; f) S. Li, Y. Xu, Y. Chen, W. Li, L. Lin, M. Li, Y. Deng, X. Wang, B. Ge, C. Yang, S. Yao, J. Xie, Y. Li, X. Liu, D. Ma, *Angew. Chem., Int. Ed.* **2017**, *56*, 10761; g) J. Jiao, R. Lin, S. Liu, W.-C. Cheong, C. Zhang, Z. Chen, Y. Pan, J. Tang, K. Wu, S.-F. Hung, H. M. Chen, L. Zheng, Q. Lu, X. Yang, B. Xu, H. Xiao, J. Li, D. Wang, Q. Peng, C. Chen, Y. Li, *Nat. Chem.* **2019**, *11*, 222.
- [73] a) C. J. M. van der Ham, M. T. M. Koper, D. G. H. Hetterscheid, *Chem. Soc. Rev.* **2014**, *43*, 5183; b) K. Ithisuphalap, H. Zhang, L. Guo, Q. Yang, H. Yang, G. Wu, *Small Methods* **2019**, *3*, 1800352; c) P. C. Shelley D. Minter, S. Lincic, *ACS Energy Lett.* **2019**, *4*, 163.
- [74] M. M. Rodriguez, E. Bill, W. W. Brennessel, P. L. Holland, *Science* **2011**, *334*, 780.
- [75] a) G.-F. Chen, S. Ren, L. Zhang, H. Cheng, Y. Luo, K. Zhu, L.-X. Ding, H. Wang, *Small Methods* **2019**, *3*, 1800337; b) X. Cui, C. Tang, Q. Zhang, *Adv. Energy Mater.* **2018**, *8*, 1800369; c) Y. Wan, J. Xu, R. Lv, *Mater. Today* **2019**, *27*, 69; d) M. Li, H. Huang, J. Low, C. Gao, R. Long, Y. Xiong, *Small Methods* **2019**, *3*, 1800388; e) D. Yan, H. Li, C. Chen, Y. Zou, S. Wang, *Small Methods* **2019**, *3*, 1800331; f) Z.-H. Xue, S.-N. Zhang, Y.-X. Lin, H. Su, G.-Y. Zhai, J.-T. Han,

- Q.-Y. Yu, X.-H. Li, M. Antonietti, J.-S. Chen, *J. Am. Chem. Soc.* **2019**, *141*, 14976; g) M. Nazemi, S. R. Panikkanvalappil, M. A. El-Sayed, *Nano Energy* **2018**, *49*, 316; h) Y. Luo, G.-F. Chen, L. Ding, X. Chen, L.-X. Ding, H. Wang, *Joule* **2019**, *3*, 279; i) L. Huang, J. Wu, P. Han, A. M. Al-Enizi, T. M. Almutairi, L. Zhang, G. Zheng, *Small Methods* **2019**, *3*, 1800386.
- [76] J. H. Montoya, C. Tsai, A. Vojvodic, J. K. Nørskov, *ChemSusChem* **2015**, *8*, 2180.
- [77] M.-M. Shi, D. Bao, B.-R. Wulan, Y.-H. Li, Y.-F. Zhang, J.-M. Yan, Q. Jiang, *Adv. Mater.* **2017**, *29*, 1606550.
- [78] a) Y. Qiu, X. Peng, F. Lü, Y. Mi, L. Zhuo, J. Ren, X. Liu, J. Luo, *Chem. - Asian J.* **2019**, *14*, 2911; b) X. Yan, D. Liu, H. Cao, F. Hou, J. Liang, S. X. Dou, *Small Methods* **2019**, *3*, 1800501; c) C. Choi, S. Back, N.-Y. Kim, J. Lim, Y.-H. Kim, Y. Jung, *ACS Catal.* **2018**, *8*, 7517; d) J. Li, S. Chen, F. Quan, G. Zhan, F. Jia, Z. Ai, L. Zhang, *Chem Mater.* **2020**, *6*, 885; e) R. Zhang, L. Jiao, W. Yang, G. Wan, H.-L. Jiang, *J. Mater. Chem. A* **2019**, *7*, 26371.
- [79] a) Q. Qin, T. Heil, M. Antonietti, M. Oschatz, *Small Methods* **2018**, *2*, 1800202; b) X. Wang, W. Wang, M. Qiao, G. Wu, W. Chen, T. Yuan, Q. Xu, M. Chen, Y. Zhang, X. Wang, J. Wang, J. Ge, X. Hong, Y. Li, Y. Wu, Y. Li, *Sci. Bull.* **2018**, *63*, 1246; c) C. C. Hengcong Tao, L.-X. Ding, Y. Jung, S. Liu, Z. Sun, *Chem* **2019**, *5*, 204; d) Z. Geng, Y. Liu, X. Kong, P. Li, K. Li, Z. Liu, J. Du, M. Shu, R. Si, J. Zeng, *Adv. Mater.* **2018**, *30*, 1803498.
- [80] a) C. Ling, X. Bai, Y. Ouyang, A. Du, J. Wang, *J. Phys. Chem. C* **2018**, *122*, 16842; b) J. Zhao, J. Zhao, Q. Cai, *Phys. Chem. Chem. Phys.* **2018**, *20*, 9248; c) L. Han, X. Liu, J. Chen, R. Lin, H. Liu, F. Lü, S. Bak, Z. Liang, S. Zhao, E. Stavitski, J. Luo, R. R. Adzic, H. L. Xin, *Angew. Chem., Int. Ed.* **2019**, *58*, 2321; d) F. Lü, S. Zhao, R. Guo, J. He, X. Peng, H. Bao, J. Fu, L. Han, G. Qi, J. Luo, X. Tang, X. Liu, *Nano Energy* **2019**, *61*, 420; e) J. Zhao, Z. Chen, *J. Am. Chem. Soc.* **2017**, *139*, 12480; f) A. C. Xu Zhang, Z. Zhang, Z. Zhou, *J. Mater. Chem. A* **2018**, *6*, 18599; g) C. He, Z.-Y. Wu, L. Zhao, M. Ming, Y. Zhang, Y. Yi, J.-S. Hu, *ACS Catal.* **2019**, *9*, 7311.
- [81] C. Wei, R. R. Rao, J. Y. Peng, B. T. Huang, I. E. L. Stephens, M. Risch, Z. C. J. Xu, Y. Shao-Horn, *Adv. Mater.* **2019**, *31*, 24.
- [82] a) C. Zhu, Q. Shi, S. Feng, D. Du, Y. Lin, *ACS Energy Lett.* **2018**, *3*, 1713; b) Y. Zheng, Y. Jiao, A. Vasileff, S. Z. Qiao, *Angew. Chem., Int. Ed.* **2018**, *57*, 7568; c) K. C. Kwon, J. M. Suh, R. S. Varma, M. Shokouhimehr, H. W. Jang, *Small Methods* **2019**, *3*, 1800492; d) H. Zhang, P. An, W. Zhou, B. Y. Guan, P. Zhang, J. Dong, X. W. Lou, *Sci. Adv.* **2018**, *4*, ea06657; e) J. Lin, A. Wang, B. Qiao, X. Liu, X. Yang, X. Wang, J. Liang, J. Li, J. Liu, T. Zhang, *J. Am. Chem. Soc.* **2013**, *135*, 15314; f) C.-H. Chen, D. Wu, Z. Li, R. Zhang, C.-G. Kuai, X.-R. Zhao, C.-K. Dong, S.-Z. Qiao, H. Liu, X.-W. Du, *Adv. Energy Mater.* **2019**, *9*, 1803913.
- [83] a) J. Zhang, Y. Zhao, X. Guo, C. Chen, C.-L. Dong, R.-S. Liu, C.-P. Han, Y. Li, Y. Gogotsi, G. Wang, *Nat. Catal.* **2018**, *1*, 985; b) S. Ye, F. Luo, Q. Zhang, P. Zhang, T. Xu, D. He, L. Guo, Y. Zhang, C. He, X. Ouyang, Q. Wang, M. Gu, J. Liu, X. Sun, *Energy Environ. Sci.* **2019**, *12*, 1000; c) L. Zhang, Y. Jia, G. Gao, X. Yan, N. Chen, J. Chen, M. T. Soo, B. Wood, D. Yang, A. Du, X. Yao, *Chem* **2018**, *4*, 285.
- [84] a) Y. Xue, B. Huang, Y. Yi, Y. Guo, Z. Zuo, Y. Li, Z. Jia, H. Liu, Y. Li, *Nat. Commun.* **2018**, *9*, 1460; b) H.-J. Qiu, Y. Ito, W. Cong, Y. Tan, P. Liu, A. Hirata, T. Fujita, Z. Tang, M. Chen, *Angew. Chem., Int. Ed.* **2015**, *54*, 14031; c) L. Fan, P. F. Liu, X. Yan, L. Gu, Z. Z. Yang, H. G. Yang, S. Qiu, X. Yao, *Nat. Commun.* **2016**, *7*, 10667; d) W. Chen, J. Pei, C. T. He, J. Wan, H. Ren, Y. Zhu, Y. Wang, J. Dong, S. Tian, W. C. J. A. C. I. E. Cheong, *Angew. Chem., Int. Ed.* **2017**, *56*, 16086; e) H. Fei, J. Dong, M. J. Arellano-Jiménez, G. Ye, N. Dong Kim, E. L. G. Samuel, Z. Peng, Z. Zhu, F. Qin, J. Bao, M. J. Yacaman, P. M. Ajayan, D. Chen, J. M. Tour, *Nat. Commun.* **2015**, *6*, 8668.
- [85] W. Chen, J. Pei, C.-T. He, J. Wan, H. Ren, Y. Wang, J. Dong, K. Wu, W.-C. Cheong, J. Mao, X. Zheng, W. Yan, Z. Zhuang, C. Chen, Q. Peng, D. Wang, Y. Li, *Adv. Mater.* **2018**, *30*, 1800396.
- [86] S. Zhao, Y. Wang, J. Dong, C.-T. He, H. Yin, P. An, K. Zhao, X. Zhang, C. Gao, L. Zhang, J. Lv, J. Wang, J. Zhang, A. M. Khattak, N. A. Khan, Z. Wei, J. Zhang, S. Liu, H. Zhao, Z. Tang, *Nat. Energy* **2016**, *1*, 16184.
- [87] J. Duan, S. Chen, C. Zhao, *Nat. Commun.* **2017**, *8*, 15341.
- [88] T. Qiu, Z. Liang, W. Guo, S. Gao, C. Qu, H. Tabassum, H. Zhang, B. Zhu, R. Zou, Y. Shao-Horn, *Nano Energy* **2019**, *58*, 1.
- [89] S. Dou, C.-L. Dong, Z. Hu, Y.-C. Huang, J.-I. Chen, L. Tao, D. Yan, D. Chen, S. Shen, S. Chou, S. Wang, *Adv. Funct. Mater.* **2017**, *27*, 1702546.
- [90] W. Zhou, D.-D. Huang, Y.-P. Wu, J. Zhao, T. Wu, J. Zhang, D.-S. Li, C. Sun, P. Feng, X. Bu, *Angew. Chem., Int. Ed.* **2019**, *58*, 4227.
- [91] M. Xiao, H. Zhang, Y. Chen, J. Zhu, L. Gao, Z. Jin, J. Ge, Z. Jiang, S. Chen, C. Liu, W. Xing, *Nano Energy* **2018**, *46*, 396.
- [92] Y. Liu, Y. Su, X. Quan, X. Fan, S. Chen, H. Yu, H. Zhao, Y. Zhang, J. Zhao, *ACS Catal.* **2018**, *8*, 1186.
- [93] S. Mukherjee, D. A. Cullen, S. Karakalos, K. Liu, H. Zhang, S. Zhao, H. Xu, K. L. More, G. Wang, G. Wu, *Nano Energy* **2018**, *48*, 217.



Zhongxin Song is an associate professor at the Shenzhen University, China. Dr. Song received her Ph.D. in Mechanical & Materials Engineering in 2018 from the University of Western Ontario, Canada. Her current research interests focus on design and synthesis of noble metal and non-noble metal-based nanomaterials for electrocatalysis and fuel cells application.



Jing-Li Luo is professor at the Shenzhen University, China, professor Emeritus at University of Alberta, and fellow of the Canadian Academy of Engineering. She obtained her Ph.D. degree in Materials Science and Engineering from McMaster University, Canada in 1992. She served as Canadian Research Chair in Alternative Fuel Cells from 2004 to 2015. Her research has been focused on fuel cells, energy storage research, clean energy technology, and corrosion control.



Xueliang Sun is a Canada Research Chair in Development of Nanomaterials for Clean Energy, fellow of the Royal Society of Canada and Canadian Academy of Engineering, and full professor at the University of Western Ontario, Canada. Dr. Sun received his Ph.D. in materials chemistry in 1999 from the University of Manchester, UK, which he followed up by working as a postdoctoral fellow at the University of British Columbia, Canada and as a research associate at L'Institut National de la Recherche Scientifique (INRS), Canada. His current research interests are focused on advanced materials for electrochemical energy storage and conversion, including solid-state batteries, interface, and solid-state electrolytes and electrocatalysts.